Midlevel Ventilation's Constraint on Tropical Cyclone Intensity

by

Brian Hong-An Tang

B.S. Atmospheric Science, University of California Los Angeles, 2004
B.S. Applied Mathematics, University of California Los Angeles, 2004

Submitted to the Department of Earth, Atmospheric and Planetary Sciences
in partial fulfillment of the requirements for the degree of

Doctor of Philosophy in Atmospheric Science

at the

MASSACHUSETTS INSTITUTE OF TECHNOLOGY

September 2010

Author . . . .
Department of Earth, Atmospheric and Planetary Sciences
June 14, 2010

Certified by . . . .
Kerry A. Emanuel
Breene M. Kerr Professor of Atmospheric Science
Director, Program in Atmospheres, Oceans and Climate
Thesis Supervisor

Accepted by . . . .
Maria Zuber
Earle Griswold Professor of Geophysics and Planetary Science
Head, Department of Earth, Atmospheric and Planetary Sciences

Midlevel Ventilation's Constraint on Tropical Cyclone Intensity

by

Brian Hong-An Tang

Submitted to the Department of Earth, Atmospheric and Planetary Sciences
on June 14, 2010, in partial fulfillment of the
requirements for the degree of
Doctor of Philosophy in Atmospheric Science

Abstract

Midlevel ventilation, or the flux of low-entropy air into the inner core of a tropical cyclone (TC), is a hypothesized mechanism by which environmental vertical wind shear can constrain a TC's intensity. An idealized framework is developed to assess how ventilation affects TC intensity via two pathways: downdrafts outside the eyewall and eddy fluxes directly into the eyewall. Three key aspects are found: ventilation has a detrimental effect on TC intensity by decreasing the maximum steady state intensity, imposing a minimum intensity below which a TC will unconditionally decay, and providing an upper ventilation bound beyond which no steady TC can exist.

Based on the idealized framework, a ventilation index is derived that is equal to the environmental vertical wind shear times the midlevel entropy deficit divided by the potential intensity. The ventilation index has a strong influence on the present-day climatology of tropical cyclogenesis and the distribution of TC intensification. Additionally, changes in the ventilation index are also examined in general circulation models (GCMs) between the late 20th century and the late 22nd century. Individual GCMs indicate potential regional shifts in preferred locations of tropical cyclogenesis and changes in TC intensity statistics due to shifts in the seasonal ventilation index, but a statistically significant projection cannot be given. The GCMs do show a robust increase in the midlevel entropy deficit and potential intensity nearly everywhere in the tropics.

Lastly, an axisymmetric model with parameterized ventilation is used to examine the sensitivity of TC intensity to the strength and location of the ventilation and to examine the findings of the idealized framework. Increasing the strength of the ventilation and placing the ventilation at lower to middle levels results in a greater decrease in the quasi-steady intensity, whereas upper-level ventilation has little effect on the intensity. For strong ventilation, an oscillatory intensity regime materializes and is tied to transient convective bursts and strong downdrafts into the boundary layer. The sensitivity of TC intensity to ventilation can be viewed in the context of a modified thermal wind relation or the fractional Carnot efficiency of the inner-core.

Thesis Supervisor: Kerry A. Emanuel
Title: Breene M. Kerr Professor of Atmospheric Science
Director, Program in Atmospheres, Oceans and Climate

Acknowledgments

It is hard to believe it has been six years in the Green Building already. I know I will look back upon my graduate years and realize how special they were. This would not have been possible without the great support and friendship of many individuals.

First, I would like to thank my advisor, Kerry Emanuel. I knew upon coming to MIT that I would learn a great deal from him given his expertise in the field, and my expectations were greatly exceeded. He has given me guidance in both my generals research and dissertation that have been invaluable to my progress, but at the same time has let me find my own way, which will benefit me greatly after I leave MIT. Not only has he advised me well in matters of science, but his ability to communicate with such eloquence has truly inspired me to do the same. Additionally, Kerry has given me opportunities few graduates have to teach, attend conferences/workshops, and participate in a field campaign.

My thesis committee has been invaluable to me. Alan Plumb is an excellent teacher, and I've benefited greatly from his class in atmospheric dynamics. I will never forget the time Alan and I were preparing a two layer convection experiment for the undergraduate fluids lab. We accidentally made the bottom layer so salty and dense that when we set out to figure out what temperature would be needed to cause the system to start convecting, we calculated it would have to be above boiling much to the laughter of the class. I would also like to thank John Molinari for giving me plenty of encouragement and also giving observational fodder that these nebulous equations on the following pages might actually apply to reality! Lastly, my research was greatly aided by Mike Montgomery. I would like to especially thank Mike and Michael Riemer for looking out for me during my trip to Guam, for hosting my trip out to Monterey in 2009, and for providing me data from their 3D hurricane simulations. I was able to fine tune and think much more critically about my research than any time before my visit out there.

I love to teach and enjoyed TAing both graduate and undergraduate courses in the department. This would not have been possible without the support of Lodovica

Illari and John Marshall. The undergraduate lab course (12.310) sets a new paradigm for teaching atmospheric science and oceanography to students, and it was a pleasure to be part of this innovative and unique experience. I do apologize again for the water spills, cords wrapping around rotating tables, and speeding up the rotation rate of the Hadley Cell demo, but at least I avoided setting the place on fire.

My colleagues and the administrative staff in the program have also been part of why my graduate years have been so memorable. Starting from when I first arrived MIT, I would like to thank Robert Korty and Bill Boos for their advice during my first couple of years. I knew I could always rely on Jon Moskaitis, Cegeon Chan, and Garrett Marino to start up a conversation about the weather, as we are all professed weather junkies. We suffered through many humbling days in the National Collegiate Weather Forecast Competition and WxChallenge, but victory was sweet when it came. Thanks to Kelly Klima and Tim Whitcomb for being great friends, as we toughed it out through classes together. I lost count how many times Dan Gombos and I ate at the student center and Quiznos over the years talking about anything from poker to ensembles. Angela Zalucha has been my ski buddy and brunch buddy, particularly because she is always at the front of the line. Lastly, Mary Elliff always put the students first, and she made a huge difference.

Finally, I would like to thank my family for being there for me through the years. I've always had the unconditional love of my family, and my success is largely due to this. My parents have asked nothing of me except to do the best I can at whatever I decide to do. For this, I dedicate this large stack of paper (a.k.a. thesis) to them.

This work is supported by NSF grant ATM-0850639.

P.S. Go crEAPS!

Contents

List of Figures

List of Tables

Chapter 1

Introduction

1.1 Motivation

Tropical cyclones (TCs) are one of nature's most destructive phenomena, having caused both heavy human and economic toll. For example, Hurricane Katrina (2005) caused an estimated 81-82 billion dollars in losses (Pielke Jr. et al., 2008). The Bagladesh Cyclone (1970) brought a storm surge that killed 300,000 people in the Ganges Delta. As more property is built up along the world's vulnerable coastlines, the potential for damage is guaranteed to increase in the future. Thus, it is important that the physics of TCs are understood in order to improve the ability to foresee short- and long-term impacts.

1.1.1 Intensity Prediction

The human toll can be mitigated by accurate predictions of TC track and intensity. The former has seen significant gains, with the track error at 72 hours in the north Atlantic decreasing from 400 n mi in the 1970s to a little over 100 n mi in 2009 (Franklin, 2010). This has been brought forth by a combination of improvements in numerical weather prediction models, better initialization of TCs in models (Kurihara et al., 1993), and an understanding of the basic physics of TC motion (Chan, 2005).

On the contrary, intensity forecasts remain quite problematic. Fig. 1-1 shows the seasonal intensity errors compiled by the National Hurricane Center for the north Atlantic basin from 1990-2009 (Franklin, 2010). The intensity is defined by the maximum one minute sustained near-surface wind speed. At all lead times, intensity forecasts have shown no statistically significant improvement over the twenty-year period. Despite the introduction of high resolution hurricane models, such as the Hurricane Weather Research and Forecast model, accurate intensity forecasts pose a challenge due to the large number of external mechanisms that control TC intensity. Examples of such controls include ocean mixing, environmental vertical wind shear, background thermodynamic state, and upper level trough interactions (Hanley et al., 2001; Emanuel et al., 2004). Additionally, asymmetric convective features (Van Sang et al., 2008) and eyewall replacement cycles (Willoughby et al., 1982) have little predictability but potentially large effects on TC intensity. Current understanding of these mechanisms is limited, hindering the ability to develop and improve guidance for intensity prediction, especially at longer forecast lead times.

This study focuses on one important external control on TC intensity: environmental vertical wind shear. Environmental vertical wind shear has been shown to have a negative impact on TC intensification. Figure 1-2 shows a box plot of the distribution of 12-hour intensity change of north Atlantic TCs between 1981-2000 binned by the vertical wind shear. To obtain an estimate of the maximum *symmetric* wind speed, 70% of the tropical cyclone's translation speed is subtracted from its reported maximum wind speed in the best track database. The 70% factor is chosen because it best matches observations (K. Emanuel, pers. communication). Moreover, the vertical wind shear is defined as the magnitude of the vector difference between the winds at 850 mb and 200 mb. The shear is estimated at the TC's center from ERA-40 reanalysis after a filter[1] is applied to remove the TC's circulation. In Fig. 1-2, there is a clear tendency for the 25th, median, and 75th percentiles of the 12-hour intensity change distribution to decrease with increasing vertical wind shear. In particular, rapidly strengthening storms tend to be embedded in environments with low vertical wind shear. The correlation between the vertical wind shear and the 12-hour inten-

---

[1] The filter used to remove TCs from the raw data is described in Appendix A.

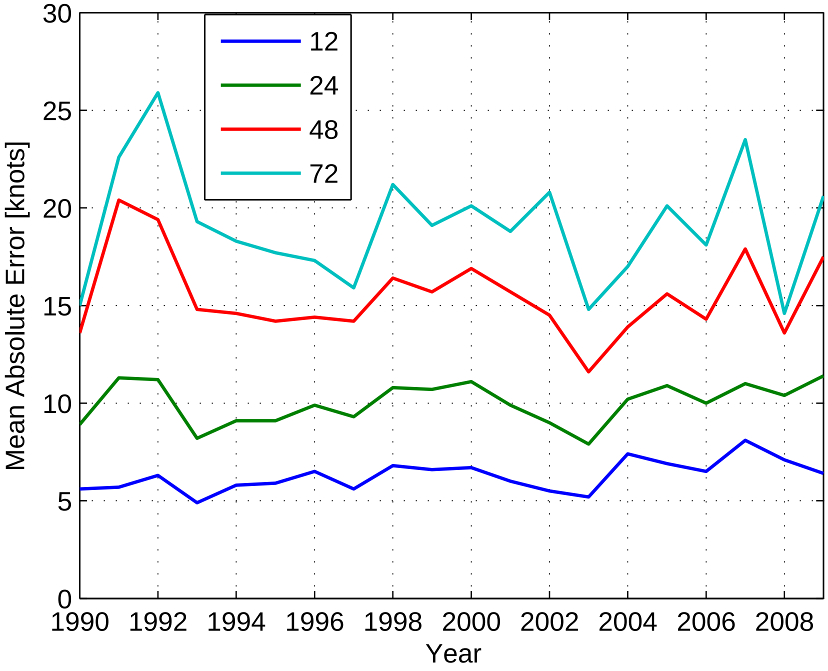

Figure 1-1: Yearly mean absolute intensity errors from the National Hurricane Center official forecasts for the north Atlantic from 1990-2009. The errors are given for forecast lead times of 12 hours, 24 hours, 48 hours, and 72 hours. The data is provided by the National Hurricane Center at http://www.nhc.noaa.gov/verification/.

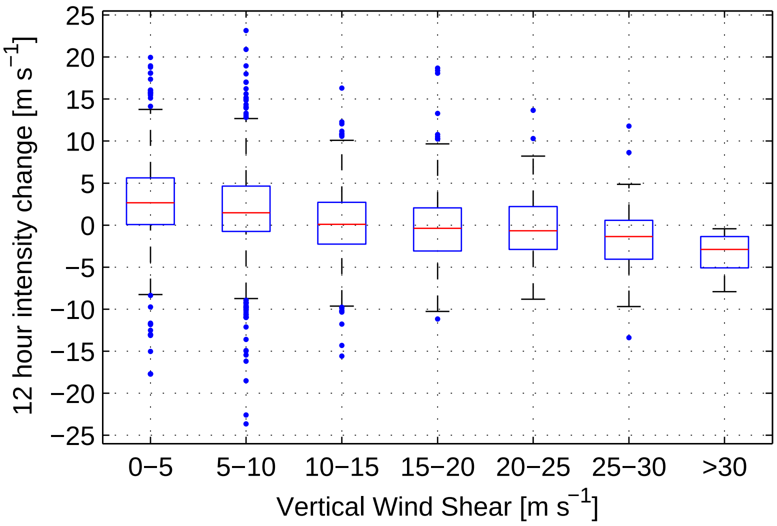

Figure 1-2: A box plot of the 12-hour intensity change of north Atlantic tropical cyclones between 1981-2000 binned by the environmental vertical wind shear. The median 12-hour intensity change in each shear bin is given by the red line, and the 25th (75th) percentile is given by the bottom (top) edge of the box. The bars extend to 1.5 times the interquartile range, and outliers are given by the blue points. Only tropical cyclone observations over water south of 30°N are used.

sity change is -0.26. Although this correlation is weak, it is statistically significant and makes environmental vertical wind shear one of the most important predictors in dynamical-statistical TC intensity models, such as the Statistical Hurricane Intensity Prediction Scheme (DeMaria and Kaplan, 1994b) and the Logistic Growth Equation Model (DeMaria, 2009), and simple dynamical models, such as the axisymmetric Coupled Hurricane Intensity Prediction Scheme (CHIPS) (Emanuel et al., 2004).

The CHIPS model accounts for vertical wind shear through an empirical parameterization, in which the moisture at midlevels in the TC is decreased in proportion to the square of the vertical wind shear. The reasoning behind such a parameterization is based on the ventilation hypothesis (Simpson and Riehl, 1958), which is elaborated upon in depth in the following chapters. While this parameterization increases the skill of the model, there is no robust reason as to why the particular form of the parameterization is valid in terms of how ventilation may actually operate. Moreover, a curious consequence of the parameterization is that it increases the sensitivity of the model (Moskaitis, 2009). Fig. 1-3a depicts the 48 hour simulated intensity field as a function of mixed layer depth and vertical wind shear magnitude for a TC with an initial intensity of 80 knots. Storms at low wind shear intensify rapidly to greater than 140 knots, while storms embedded in greater than 10 m s^{-1} of vertical wind shear weaken below the initial intensity. Fig. 1-3b shows the magnitude of the intensity field gradient, which is a measure of sensitivity of the intensity to both the vertical wind shear magnitude and mixed layer depth. The sensitivity is dominated by vertical wind shear since the largest gradients are in the direction of the ordinate, with the greatest sensitivity around a vertical wind shear of 5 m s^{-1}. Unfortunately, this coincides to the climatological mode of the distribution of vertical wind shear in the tropics. The sensitivity reduces the predictability of TC intensity in the CHIPS model. If this sensitivity does indeed exist in reality, what is causing it?

Given that the shear parameterization is empirical and effectively folds all model error into it, it is possible that the sensitivity to vertical wind shear is unrealistic. This underscores the importance of achieving a better understanding of the physical pathways by which vertical wind shear affects intensity, which ideally will lead to refinements or new approaches to the CHIPS shear parameterization and other statistical-dynamical intensity guidance.

1.1.2 Defining Shear

Perhaps the most fundamental question that must be addressed is how one defines vertical wind shear for TC intensity studies. Obviously, there is a textbook definition of shear, but why use only the winds at 200 mb and 850 mb? In fact, there is no dynamical reason given in the literature as to why these two levels are used. Apparently, the 850-200 mb convention arises from the fact that cloud track winds are relatively dense and reliable at these two levels (Mark DeMaria, pers. communication). While the conventional metric is satisfactory for linear profiles of environmental flow, hodographs from Reasor et al. (2000) and Rogers et al. (2003) show that the environmental wind profile contains nonlinear structure with height, and Elsberry and Jeffries (1996) speculate that differently shaped profiles may arise depending on the source of the vertical shear. Consequentially, is the structure of the environmental

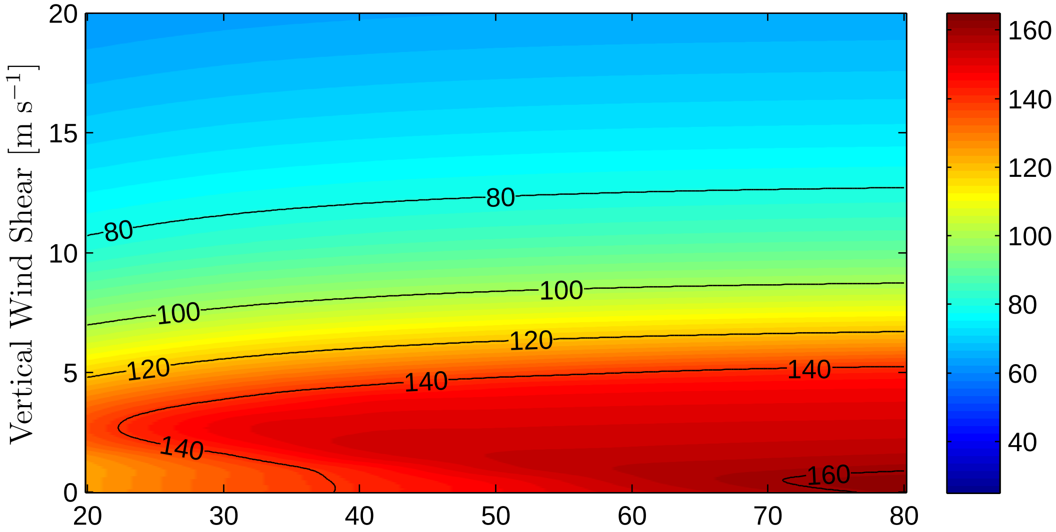
(a) Intensity [knots]

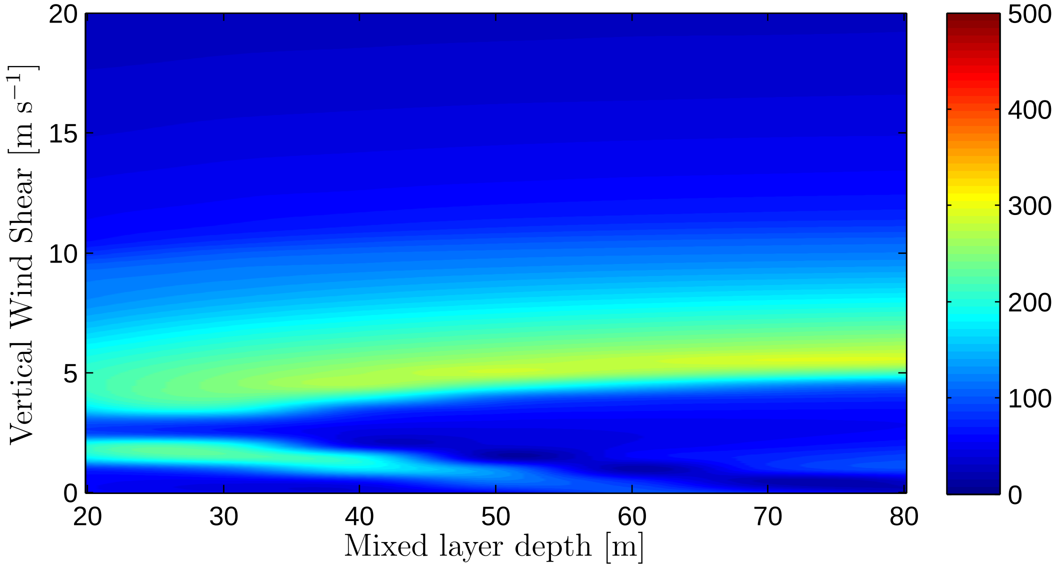
(b) Intensity gradient magnitude

Figure 1-3: (a) The 48 hour intensity field from the CHIPS model as a function of mixed layer depth and vertical wind shear for an initial intensity of 80 knots. (b) The intensity gradient magnitude field, which is a measure of the sensitivity of the model to the externally prescribed parameters. This figure is used with permission from Jonathan Moskaitis.

wind profile with height important for a tropical cyclone's evolution?

In light of the possible high sensitivity of intensity to the value of the vertical wind shear, it is imperative that the shear is accurately estimated. Achieving this, however, is not straightforward due to the fact that the environmental flow must be separated from the baroclinic structure of the TC, which itself contains very large amounts of vertical shear. Several popular methods include averaging the winds over a large annulus or disc around the TC and interpolating the synoptic flow to the TC's center (Gallina and Velden, 2002). The different methodologies can lead to differences of a few m s^{-1} in the vertical wind shear estimate. What is the relevant quantity to consider: the average vertical wind shear over the entire system or the shear in the vicinity of the center?

The lack of solid reasoning behind the usage of the conventional vertical wind shear metric that pervades the literature must be addressed. What one really seeks is a dynamically and/or thermodynamically relevant metric based on the primary physical pathway by which wind shear affects TC intensity. This may involve the interaction of a number of parameters, and an example of one possible interaction is explored in the third chapter.

1.2 Background

1.2.1 Observations of Sheared Tropical Cyclones

A number of studies have looked at the evolution of individual TCs in the presence of vertical wind shear using aircraft, radar, lightning, and satellite data. Low-wavenumber asymmetries in the convective pattern consistently appear, with deep convection favored on the downshear side of the storm coincident with the vertical velocity and lightning strike density maxima (Reasor et al., 2000; Corbosiero and Molinari, 2002). Conversely, the convective minimum and strongest subsidence are located in the upshear direction. A detailed study of the life cycle of convective elements in the eyewall of Hurricane Jimena embedded in 20 m s^{-1} of vertical shear was performed by Black et al. (2002). Initiation of updrafts occurred in the downshear semicircle below 6 km. The updrafts, sloping radially outward with height, then reached their maximum magnitude after rotating cyclonically approximately 90°. Thereafter, condensate loading and evaporative cooling drove strong downdrafts of greater than 8 $\mathrm{m\ s^{-1}}$ through a deep layer in the upshear semicircle. The net result of the vertical shear is to make individual convective elements generally shorter lived and shallower than what might otherwise be observed in a healthy TC.

Asymmetries in convection and vertical velocity are intimately connected to asymmetries in the horizontal flow and relative vorticity. Most of the variance in relative vorticity in Hurricane Olivia was confined to a 5-10 km radial band and dominated by the contributions from wavenumber one asymmetries above 3 km and wavenumber two asymmetries below 3 km (Reasor et al., 2000). There are a number of plausible sources for these convectively-coupled asymmetries: barotropic instability, asymmetric diabatic heating, tilting of radial and azimuthal vorticity filaments by updraft-downdraft couplets, and the projection of a tilted potential vorticity (PV) column on individual levels. The tilt can be quite pronounced in strongly sheared storms, with the horizontal distance between low and upper level centers exceeding 10 km (Corbosiero and Molinari, 2002). Additionally, the tilt of the outer vortex may be even larger (Jones, 2004). Although asymmetries are clearly prominent in TCs, their behavior in sheared TCs along with their role in altering intensity have not been thoroughly investigated.

The symmetric structure of the TC, which is analogous to an idealized Carnot heat engine (Emanuel, 1986), is also altered by the presence of vertical wind shear. Composited temperature data from the Advanced Microwave Sounding Unit indicates that as shear increases, the height of the symmetric warm anomaly decreases in the core of the TC. In accordance with thermal wind, the TC's circulation becomes shallower (Knutson and Tuleya, 2004). From the Carnot heat engine point of view, a shallower circulation implies a reduced thermodynamic efficiency and a lower potential intensity. It appears the tropical cyclone weakens from the top down, but the composited analysis doesn't indicate how this occurs, i.e. one cannot conclude that the mechanism behind the weakening also originates at upper levels and descends with time.

To gain more insight beyond changes to the symmetric thermodynamic structure, recent studies have looked at equivalent potential temperature (θ_e) or moist entropy asymmetries in highly sheared TCs. For instance, dropsondes and flight data were used construct the θ_e field in Tropical Storm Chantal (Heymsfield et al., 2006). At low levels, very high θ_e air (> 360 K) was confined to the downshear semicircle of the low-level center feeding a deep convective burst, while the upshear side had θ_e values less than 355 K. Further aloft, a subsidence inversion, imparted by the shear-induced secondary circulation, existed between 700-800 mb and inhibited any deep convection over the low-level center. The lowest values of θ_e were also found on the upshear side at about 500 mb, with minimum values around 335 K.

In another case study, Hurricane Claudette (2003) weakened drastically from a hurricane to a weak tropical storm, as vertical wind shear rose to greater than 10 $\mathrm{m\,s^{-1}}$. Shelton and Molinari (2009) studied the evolution of the storm from reconnaissance data. As the storm started to weaken, there was radial flow of greater than 15 $\mathrm{m\,s^{-1}}$ at 700 mb from NW and SE. Coinciding with the strong midlevel inflow was a layer of dry air with low-θ_e values. It is hypothesized that the storm weakened in response to the entrainment of the low-θ_e air into the eyewall, which subsequently led to the production of evaporatively cooled downdrafts. The downdraft cold pool produced divergence at low levels and stabilized the boundary layer.

Powell (1990) studied the boundary layer θ_e structure across outer rainbands and found cold pools spreading out on the inner side of a rainband in Hurricane Earl (1986) over an area of at least 250 $\mathrm{km^2}$. As this air then spirals inward, the presence of additional downdrafts in the stratiform rain region adjacent to the convective rainband and entrainment at the top of the mixed layer in a region of mesoscale subsidence may prevent θ_e from increasing despite surface fluxes. Moreover, if the rainband is positioned close to the center of the cyclone, then the time available for recovery of the downdraft air is abbreviated.

Downdrafts sap the TC's source of energy by mitigating the increase in θ_e due to surface fluxes leading to surface pressure rises in the center of the storm. Assuming hydrostatic balance, Malkus and Riehl (1960) derived a relationship between changes in surface pressure and changes in surface θ_e at the base of the eyewall:

$$p' \approx -2.6\theta_e'. \tag{1.1}$$

Emanuel (1986) derived a similar relationship between changes in central surface pressure and changes in the saturation equivalent potential temperature, θ_{ec}^*, at the center of the storm above the boundary layer by considering gradient wind balance and slantwise neutrality:

$$p_{cs}' \approx -3.3\theta_{ec}^{*\prime}. \tag{1.2}$$

As a consequence of thermal wind balance, Emanuel (1997) showed that the square of the maximum tangential wind speed is directly proportional to the radial gradient of θ_e or moist entropy:

$$v_m^2 \approx -r_m \left(T_b - T_o\right) \frac{\partial s_b}{\partial r}, \tag{1.3}$$

where v_m is the maximum tangential wind, r_m is radius of maximum wind, T_b is the temperature at the top of the boundary layer, T_o is the outflow temperature, and s_b is the moist entropy at the top of the boundary layer. Weakening the radial gradient of entropy in the eyewall by adding an entropy sink in the inner-core region will weaken the TC's primary circulation. This can be accomplished, for instance, by the incomplete recovery of downdraft air originating from spiral rainbands or downdrafts in the eyewall itself. However, a numerical study by Wang (2002b) found that downdraft air originating from spiral rainbands to have a negligible effect in a *mature, unsheared* TC. In fact, downdrafts occurring outside the eyewall may enhance the radial gradient of entropy and, hence, the maximum tangential wind speed as long as enhanced surface fluxes lead to a full recovery of the downdraft air during its inward transit (Yang et al., 2007). However, how different is the recovery timescale in vertically sheared TCs? If inner rainbands with unsaturated downdrafts are excited closer to the eyewall and/or over a much larger region, do they have a correspondingly larger effect, as there is less opportunity for recovery?

1.2.2 Numerical Modeling Studies of Sheared Tropical Cyclones

Since continuous, high-resolution monitoring of TCs is not currently possible, most research on this topic uses sophisticated numerical models to understand how TC structure is altered in the presence of vertical wind shear. Although numerical models corroborate the observations presented in the previous section, it is much harder to deduce whether and how these changes in structure lead to changes in intensity.

One such change in structure is the tilt of the vortex, which may play a role in exciting asymmetries. Since observations of the tilt are scarce, numerical simulations can elucidate the nature of the tilt evolution. Jones (1995) studied this phenomenon using a dry, primitive equation model on an f-plane with an easterly shear of 4 $\mathrm{m\ s^{-1}}$. The column of high PV precesses, and after a sufficient amount of time, the PV anomalies in the lower and upper levels decouple, although the details of this behavior are sensitive to the initial profile of relative vorticity (Reasor et al., 2004) and the penetration depth (Smith et al., 2000). In a moist setting, the tilt is significantly reduced due to a negative feedback associated with the diabatic heating, but can still exceed 10 km for shears greater than 10 $\mathrm{m\ s^{-1}}$. Additionally, the tilt does not evolve with a constant slope to mirror the specified linear shear profile, but rather, the layer of strongest tilt is initially found at upper levels and descends with time (Frank and Ritchie, 2001; Wong and Chan, 2004).

The tilt along with background vertical wind shear requires there to be isentropic gradients which induce wavenumber one vertical velocity asymmetries in a *dry* framework (Jones, 1995, 2000a,b). If moisture is introduced and diabatic effects dominate, the strongest vertical velocities and convection are shifted to the downshear-left quadrant (in the N Hemisphere) in agreement with observations (Frank and Ritchie, 1999). Instead of the adiabatic mechanisms, asymmetric divergence due to the relative flow is now primarily responsible for the wavenumber one vertical velocity asymmetries (Bender, 1997). As necessitated by conservation of PV, asymmetric relative flow into (out of) the core of the TC must be associated with asymmetric convergence (divergence) and ascent (descent) at low levels. The same reasoning can also be applied at upper levels to explain the shear-induced secondary circulation.

Thermodynamic changes to the structure of sheared TCs have also been documented in numerical simulations. With regards to the symmetric structure, the warm core of a moist TC in 10 $\mathrm{m\,s^{-1}}$ of easterly shear erodes at upper levels after the shear onset, but the lower half of the troposphere within 50 km of the center warms by 2-4 K (Wong and Chan, 2004). DeMaria (1996) explained the warming in the lower troposphere above the low-level circulation using a two-layer, dry model with offset Gaussian PV anomalies in each layer. A positive temperature perturbation of 3 K for an initial displacement of 60 km arises above the low-level center, increasing the vertical stability and hypothetically retarding convection (cf. Heymsfield et al. (2006)). On the other hand, a negative perturbation arises in the direction of the tilt, decreasing the stability and augmenting convection.

While the thermodynamic changes partially explain the wavenumber one pattern in convection, it is not immediately apparent that asymmetries must necessarily weaken the mean circulation of the TC. In fact, there is evidence to the contrary from both observational and modeling studies. Despite a large wavenumber one asymmetry in convection, Tropical Storm Gabrielle was observed to intensify by 20 mb over the course of 3 hours due to the downshear reformation of the center by diabatic vorticity generation (Molinari et al., 2006). Two studies by Moller and Montgomery (1999, 2000), using a barotropic and baroclinic model, indicate that symmetrizing PV anomalies, which can be generated by asymmetrically distributed convection, act to accelerate the tangential winds.

Frank and Ritchie (2001) investigated the PV and θ_e evolution of a TC embedded in a vertical wind shear of $5\ \mathrm{m\,s^{-1}}$ and postulated that the weakening of the TC occurs from the top down. A Fourier decomposition of the PV reveals that after the onset of the shear, the power in the axisymmetric component decreases while the power in the wavenumber one component increases. High-θ_e air is advected outward from the core of the TC most vigorously at upper levels at first, but then this outward advection descends with time. However, the azimuthally averaged horizontal eddy flux of θ_e is positive through a *deep* layer in the eyewall right before weakening commences. Consequently, the central surface pressure must rise as the warm core is weakened aloft. Wong and Chan (2004) also conjecture that ventilation in the upper levels causes their simulated TC to weaken, but instead suggest a threshold behavior. Weakening only occurs when the environmental vertical shear is strong enough to produce net subsidence in the upshear portion of the eyewall, leading to the entrainment of ambient low-θ_e air at upper levels as inflow dominates. However, the θ_e at upper levels is typically high, so the source of this low-θ_e air is unclear. Additionally, given the simulations of Bender (1997), it isn't clear that large values of vertical shear greater than 10 $\mathrm{m\,s^{-1}}$ are capable of offsetting the TC's thermally direct circulation. It also remains to be clarified whether the "eddies" responsible for the aforementioned mechanisms are simply the projection of the relative flow onto wavenumber one or mesoscale eddies, such as vortex Rossby waves.

In contrast, Wu and Braun (2004) concluded that eddies are unable to significantly alter the temperature perturbations in the inner core of a TC embedded in 4 $\mathrm{m\,s^{-1}}$ of vertical wind shear. Rather, the lowering of the warm core and weakening of the TC by 8 mb or 4 $\mathrm{m\,s^{-1}}$ is attributed to eddy momentum fluxes that act to decelerate the radial and tangential flow at lower and upper levels. However, the differences between the control simulation and shear simulation lie within the general predictability envelope of 3D simulations (Van Sang et al., 2008), so it is unclear if the differences are truly due to the vertical wind shear forcing or simply random. Furthermore, the vertical wind shear was not varied in the study to assess whether the results are sensitive to the magnitude of the shear.

Instead of ventilation at upper levels, ventilation at midlevels, near the climatological minimum of θ_e, can affect the inner-core and act as "a constraint on the hurricane heat engine (Simpson and Riehl, 1958)." Cram et al. (2007) investigated Lagrangian back trajectories of parcels at a height of 5 km in the eyewall of a numerical simulation of Hurricane Bonnie (1998), which was embedded in 12 $\mathrm{m\,s^{-1}}$ of vertical shear at the time. They found that about 20% of the eyewall mass originated from middle to upper levels. Since parcels at these levels have a lower θ_e than that of the eyewall, the midlevel ventilation acts to decrease the θ_e in the eyewall by approximately 1 K.

Ventilation's effects on the TC inflow layer have also been examined in an idealized numerical framework. Riemer et al. (2010) studied simulations of TCs embedded in varying amounts of vertical shear and hypothesized that a shear-induced, standing wavenumber one vorticity asymmetry forms in response to tilting of the outer vortex between a radius of 150-200 km. Where the vorticity asymmetry is positive, upward motion is enhanced due to frictional convergence and convection is enhanced. The convection forms a helical updraft pattern, which allows rain to fall into unsaturated air below it resulting in the formation of downdrafts. Consequently, these downdrafts flux a significant quantity of low-θ_e air down into the boundary layer. Thereafter, the low-θ_e air can then be swept in toward the eyewall of the storm where it acts as an "anti-fuel" mechanism weakening the TC. Only after these downdrafts cease and the vortex realigns do the simulated TCs begin to restrengthen.

One critical issue that needs to be addressed is how the low-θ_e air is actually getting into the inner core. While the relative flow might do the job for weak vortices, the relative flow would need to be unrealistically strong to be able to push the dividing streamline close enough to the inner core in hurricane-strength vortices (Michael Riemer, pers. communication). This is especially hard at midlevels since the steering level of TCs is located in this layer, implying weak relative flow. Alternatively, there may be some transient phenomena allowing the low-entropy air to be turbulently advected inward. A good candidate is vortex Rossby waves.

1.2.3 Vortex Rossby Waves

Perturbations in the TC flow - induced by convective asymmetries, tilt of the vortex, or some other mechanism - have been determined numerically and observationally to be vortex Rossby waves propagating along the TC's sharp gradient(s) of potential vorticity. The linearized theory for vortex Rossby waves was first derived by Montgomery and Kallenbach (1997), and the wave-mean flow interaction was generalized by McWilliams et al. (2003). Moller and Montgomery (2000) derived a dispersion relationship for vortex Rossby waves using asymmetric-balance theory:

$$\omega = n\bar{\Omega} + \frac{n}{R}\frac{\bar{\xi}}{\bar{q}}\frac{\bar{q}'}{k^2 + n^2/R^2 + (\bar{\eta}\bar{\xi}m^2)/N^2}, \tag{1.4}$$

where ω is the frequency, n is the azimuthal wavenumber, k is the radial wavenumber, m is the vertical wavenumber, N is the Brunt-Vaisala frequency, R is a reference radius, Ω is the angular velocity, q is the potential vorticity, η is the absolute vorticity, and ξ is the inertia parameter. Any variable with an overbar refers to the basic-state vortex, and any variable with a prime denotes its radial gradient. Strong evidence of the existence of vortex Rossby waves was provided by Corbosiero et al. (2006) in which wavenumber two banded features sporadically broke off from the shear-induced wavenumber one distributed eyewall convection in Hurricane Elena and had phase and group velocities consistent with those derived from (1.4).

Wang (2002a,b) conducted a detailed investigations of the structure and energy budgets of vortex Rossby waves in a primitive equation model. The main findings were:

- Most of the power lies in wavenumbers one and two, but wavenumber two activity is much more variable.
- The horizontal flow and geopotential height anomalies are quasi-balanced[2] with maximum PV anomaly amplitudes at low levels near the radius of maximum wind.
- The azimuthal wind anomalies are at times 10-20% the mean azimuthal mean wind speed.
- Vertical velocity anomalies are greater than 50% the mean eyewall vertical velocities and dominate outside the eyewall, implying convection can be greatly modulated by vortex Rossby waves.

---

[2] Quasi-balanced refers to a class of hydrostatic motions in the atmosphere where horizontal pressure gradients are closely balanced by centrifugal accelerations.

- Eddy kinetic energy is maximized near the eyewall and shows three distinct maxima located at the outflow layer, at 500 mb, and at low levels below 800 mb.

- Vertical velocity and relative vorticity perturbations are in approximate quadrature and are strongly convectively coupled.

- A trailing spiral structure is prominent in the radius-azimuth plane, which implies that the group velocity is directed outward, and the wave is transferring its energy to the mean-flow. An outward tilt occurs in the radius-height plane.

- Nonlinear interactions of wavenumber one waves excites wavenumber two waves, especially near the radius of maximum wind.

- There appears to be a stagnation radius and stagnation height, and both decrease as wavenumber increases. This implies that vortex Rossby waves are limited to the inner region of the tropical cyclone at lower to middle levels.

On the last point, the stagnation radius and stagnation height can be derived from the appropriate group velocities using (1.4) and letting $t \to \infty$. The resulting expression for the stagnation radius is

$$r_s = R + \frac{\bar{\xi}\bar{q}'}{R\bar{q}\bar{\Omega}'}\frac{1}{\kappa_{t0}^2}, \tag{1.5}$$

and the stagnation height is

$$z_s = Z - \frac{m\bar{\eta}\bar{\xi}^2\bar{q}'}{RN^2\bar{q}|\bar{\Omega}'|}\frac{1}{\kappa_{k0}^3}\left[\frac{\pi}{2} + \frac{\bar{\Omega}'}{|\bar{\Omega}'|}\arctan\left(\frac{k_o}{\kappa_{k0}}\right) + \frac{\bar{\Omega}'}{|\bar{\Omega}'|}\frac{\kappa_{k0}k_o}{\kappa_{t0}^2}\right], \tag{1.6}$$

where $\kappa^2 = k^2 + n^2/R^2 + (\bar{\eta}\bar{\xi}m^2)/N^2$, $\kappa_{t0} = \kappa(t = 0)$, $\kappa_{k0} = \kappa(k = 0)$, and Z is a reference height.

The interplay of vortex Rossby waves with the mean flow has been primarily studied through eddy momentum and PV fluxes. In a barotropic vortex, axisymmetrization of vortex Rossby waves leads to an increase in the tangential winds near and inside the radius of maximum wind and a decrease radially outward (Montgomery and Kallenbach, 1997; Moller and Montgomery, 1999). For a baroclinic vortex, the picture is slightly altered with an increase in tangential wind around the radius of maximum wind at the bottom of the domain bracketed by decreases in the tangential wind at small and large radii (Moller and Montgomery, 2000; Wang, 2002b). In a more complex, nonhydrstoatic 3D model of a quasi-steady TC, Eliassen-Palm flux diagnostics performed by Chen et al. (2003) indicate that eddy momentum fluxes accelerate the tangential winds on either side of the eyewall at low to midlevels. Wang (2002a,b) attributed this pattern to the asymmetric horizontal redistribution of angular momentum from the eyewall into the eye and vertical flux divergence of angular momentum at the eyewall.

For larger amplitude perturbations in both the barotropic and baroclinic simulations at upper levels, the radial gradient of PV changes sign at one or more radii, satisfying the necessary condition for barotropic instability. This allows vortex Rossby waves to grow at the expense of the energy of the mean flow, at least temporarily. In contrast at lower levels in the baroclinic simulations, perturbations are axisymmetrized for the entire range of amplitudes examined. When instead the perturbations are pulsed every hour for a narrow double-cluster PV anomaly to simulate convective bursts, as is often observed in a sheared TC, the TC intensifies about 16 $\mathrm{m\,s^{-1}}$ over a day. Broader perturbations are even more effective at increasing the maximum winds. Thus in terms of eddy-mean flow interaction, it is not at all obvious how asymmetries induced by environmental vertical wind shear cause TCs to weaken.

Wang (2002a,b) looked at the energy budget of vortex Rossby waves. The main sink of eddy kinetic energy is barotropic conversion in the lower half of the troposphere. An upscale transfer of energy occurs as the vortex Rossby waves are axisymmetrized. On the other hand, the main source of eddy kinetic energy is eddy potential energy, driven by asymmetric diabatic heating. Another source of eddy kinetic energy is baroclinic conversion, which is a function of the vertical shear of the mean radial and tangential flows. Consequently, the conversion of kinetic energy from the mean flow to the eddies is maximized in the eyewall, where the vertical shear of the vortex is largest. Increasing the vertical shear of the vortex by tilting it would enhance the production of eddy kinetic energy and, thus, decrease the mean kinetic energy.

Kwon and Frank (2008) specifically studied the energy life cycle of asymmetries in a 3D simulation of a moderately sheared TC. They found that there is significant baroclinic growth of eddies at upper levels and hypothesize that the eddies act to weaken the available potential energy of the mean vortex, leading to decay of the upper-level warm core. Periods of enhanced eddy kinetic energy are correlated with decreases in the temperature at upper-levels. Thus, they postulate that upper-level ventilation causes a hydrostatic increase in central minimum pressure and a decrease in the tangential wind, which is the same mechanism as that proposed by Frank and Ritchie (2001).

Several studies have looked at the connection between the tilt of a TC and vortex Rossby waves, primarily concentrating on the resistance of dry vortices to decoupling. The tilt excites a near-discrete vortex Rossby wave "quasi-mode" and is resonantly damped at the critical radius[3] only if the radial gradient of PV is negative at the critical radius. On the other hand, if the radial gradient of PV is instead positive at the critical radius, then the quasi-mode (tilt) will grow (Schecter et al., 2002). For small amplitude tilts, one can also view the quasi-mode heuristically as a harmonic oscillator with shear as the time-invariant forcing (see Fig. 6 in Reasor et al. (2004)). A downshear-left tilt equilibrium exists if the precession frequency is larger than the quasi-mode damping rate. Conversely, decoupling of the vortex occurs when the precession frequency is too small to counter the differential advection by the environmental relative flow. If instead the Rossby number and the ratio between the radius of maximum winds and internal deformation radius are both sufficiently large, the tilt will project onto sheared vortex Rossby waves instead of the quasi-mode allowing the tilt to decay, as the vortex Rossby waves are axisymmetrized (Reasor et al., 2004). Although the explicit effects of moisture are excluded in these models, it is speculated that diabatic effects will increase the resiliency of the vortex to tilting by increasing the precession frequency and the quasi-mode damping rate.

---

[3] The radius at which the angular phase velocity of the quasi-mode equals the angular velocity of the basic-state vortex

Given that a quasi-mode or sheared vortex Rossby waves are directly associated with vertical wind shear, how do they affect the intensity of the TC? There appears to be disagreement on whether eddy momentum fluxes act to intensify (e.g. Moller and Montgomery (2000)) or weaken (e.g. Wu and Braun (2004)) the mean circulation, and the results depend on many degrees of freedom such as the behavior (discrete vs. sheared), location, and amplitude of the eddies along with the mean vortex structure itself. Eddy momentum fluxes are likely not the primary reason as to how vertical wind shear constrains the intensity of TCs.

Thus, the attention turns toward the thermodynamic pathway, as TC intensity is quite sensitive to the distribution of moist entropy in the inner core. Asymmetries in the inner core are efficient at mixing entropy and other conserved tracers over horizontal distances of 60-80 km (Hendricks and Schubert, 2009), so it is possible that vortex Rossby waves are acting as the intermediary by which ventilation can occur. This study seeks to use theoretical, observational, and idealized modeling frameworks to study the parameterized role of vortex Rossby waves in ventilating the TC and the resulting thermodynamic pathway by which the intensity is affected.

1.3 Hypothesis and Objectives

How does ventilation affect TC intensity? Two possible pathways are sketched in Fig. 1-4. The first possible pathway is to inject low-entropy air at midlevels, given by the hatched region, directly into the eyewall. The low-entropy air can be directly entrained into the secondary circulation and then be communicated downward as downdrafts. This results in a decrease in the entropy over a deep layer in the eyewall. Additionally, a feedback can then occur in which surface fluxes are reduced due to a decrease in surface winds, allowing ventilation to depress the entropy even further.

The second pathway by which ventilation can affect TC intensity are downdrafts originating in near-inner core convection forced by the vertical wind shear. These downdrafts flush the boundary layer with low-entropy air, which is then advected radially inward into the inner core of the TC. Surface fluxes act to mitigate the

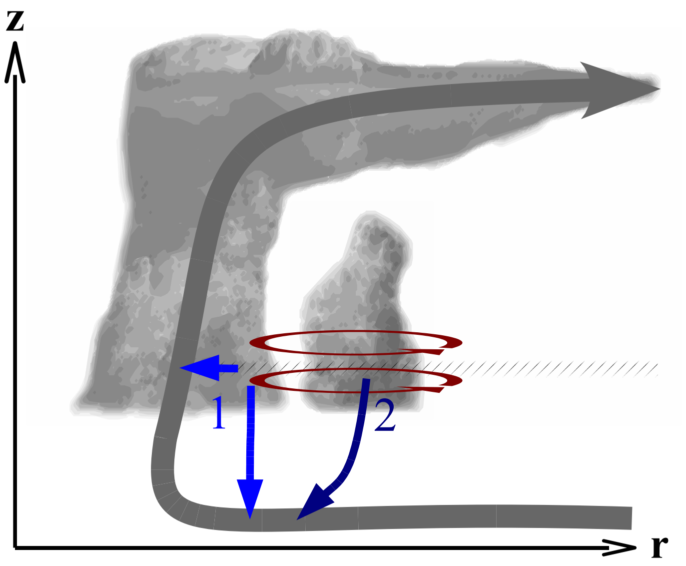

Figure 1-4: A radius-height schematic of the hypothesized pathways by which ventilation constrains a TC's intensity: (1) direct ventilation of the eyewall at midlevels and (2) downdraft modification of the boundary layer by near-inner core convection. The hatched region denotes low-entropy air at midlevels, circular red arrows denote vortex Rossby waves, and blue arrows denote ways the low-entropy air can enter the secondary circulation, which is given by the gray arrow.

effect of the downdrafts, but if the recovery is incomplete upon reaching the radius of maximum wind, the TC will still weaken. Like the previous pathway, a feedback may play a role in further weakening a TC once surface fluxes are diminished, leading to a greater amount of low-entropy air reaching the radius of maximum wind.

The primary objectives of each of the chapters in this thesis are listed below:

- Chapter 2: To formulate a steady-state theoretical framework for evaluating the hypothesized effects of ventilation on the maximum intensity of TCs.

- Chapter 3: To assess whether ventilation has a detectable fingerprint on global TC statistics and to evaluate how ventilation may affect TCs in the future.

- Chapter 4: To develop and use an axisymmetric model to study the sensitivity of TCs to ventilation strength and location.

Conclusions and future work follow in Chapter 5.

Chapter 2

A Theoretical Framework for Ventilation Modified Intensity

2.1 Introduction

Improving forecasts of tropical cyclone (TC) intensity has proven to be a vexing challenge. Part of the challenge continues to be defining pathways by which the ambient environment controls TC intensity. One particular environmental forcing, vertical wind shear, is generally observed to be a negative factor for TC intensification and is a primary reason why the vast majority of TCs fall well short of their potential intensity (DeMaria and Kaplan, 1994a; Emanuel, 2000; Zeng et al., 2007, 2008).

Although a causal link between vertical wind shear and TC intensity clearly exists, it is unclear how this physically comes about. Various theories have been put forth, including ventilation of the upper level warm core (Frank and Ritchie, 2001; Wong and Chan, 2004), increasing tropospheric stability (DeMaria, 1996), and eddy momentum fluxes (Wu and Braun, 2004). The goal of this study is not to evaluate each hypothesis that has been put forth, but to develop and analyze a simple framework for studying

---

[1] Permission to use figures, tables, and brief excerpts from this chapter in scientific and educational works is hereby granted provided that the source is acknowledged: Tang, B. and K. Emanuel, 2010: Midlevel ventilation's constraint on tropical cyclone intensity. *J. Atmos. Sci.*, **67**, 1817-1830.

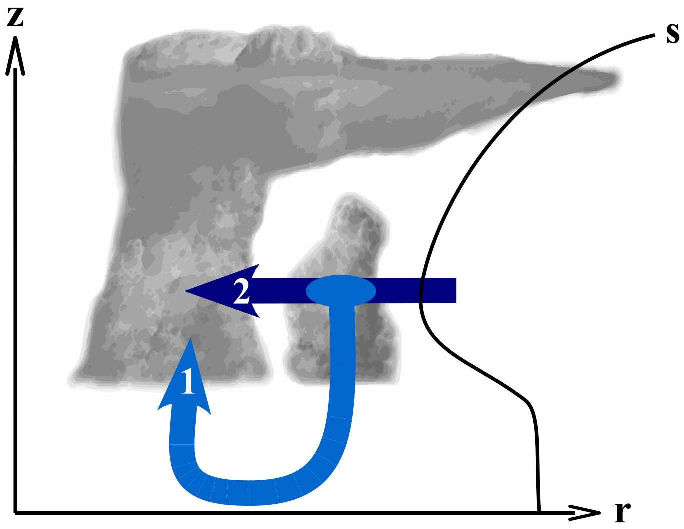

Figure 2-1: Ventilation pathways by which low-entropy air can infiltrate the eyewall. (1) Low-level pathway: downdraft air from convection originating outside eyewall is advected inwards in the subcloud layer. (2) Midlevel pathway: eyewall directly ventilated by eddy fluxes. A sample entropy profile of the environmental tropical troposphere with a well mixed subcloud layer is given on the right.

one hypothesis in particular: midlevel ventilation of a TC's inner core (Simpson and Riehl, 1958).

The ventilation hypothesis consists of both dynamical and thermodynamical components, and only the latter will be examined in this study. The dynamical component deals with the kinematics of how the TC vortex interacts with the environmental vertical wind shear, namely the tilt of the potential vorticity column due to differential advection by the background flow (Jones, 1995; Smith et al., 2000) and the subsequent excitation of low-wavenumber asymmetries such as vortex Rossby waves (Schecter et al., 2002; Reasor et al., 2004). The thermodynamic component concentrates on how eddy fluxes of low entropy from the ambient environment by these shear-induced asymmetries subsequently interact with the tropical cyclone's energetics, thereby acting as a "constraint on the hurricane heat engine" (Simpson and Riehl, 1958).

Sea surface enthalpy fluxes allow the hurricane heat engine to maintain itself against frictional dissipation, and any process that acts as a source of low-entropy air would counter the air-sea fluxes that drive the mechanical energy generation. There are two possible ways for low entropy to infiltrate the inner core, as shown in Fig. 2-1. The first is flushing the boundary layer with low-entropy air by convective downdrafts in the near inner core region (Powell, 1990; Riemer et al., 2010). From there, the low-entropy air is advected toward the eyewall by the radial inflow. We will refer to this as the "low-level pathway." The second is direct ventilation of the eyewall, where low-entropy environmental air is forced into the eyewall at midlevels by eddies (Cram et al., 2007). We will refer to this as the "midlevel pathway." It should be recognized that in both pathways, the origin of the low-entropy air is above the boundary layer through the midlevels of the troposphere. Although ventilation likely operates to some degree in all TCs, given that flow asymmetries and downdrafts are commonly observed in TCs, the magnitude and scope of these negative factors in the presence of vertical wind shear may be key to how TCs respond to hostile environments. Indeed, such a response is a necessary part of the Coupled Hurricane Intensity Prediction Scheme to produce skillful intensity forecasts (Emanuel et al., 2004).

There is compelling observational evidence of ventilation occurring in reconnaissance data and that the ventilation is correlated with observed intensity changes. Reconnaissance through strongly sheared Hurricane Claudette (2003) sampled greater than 15 $\mathrm{m\,s^{-1}}$ inflow of low-entropy air at 700 hPa on the NW side of the storm's inner core (Shelton and Molinari, 2009). Coinciding with the ventilation was a weakening of Claudette's intensity by about 10 $\mathrm{m\,s^{-1}}$. Additional reconnaissance data has also recorded strong downdrafts spawned from precipitation falling into dry air in the inner core of sheared Hurricanes Jimena (1991) and Olivia (1994) and may have also contributed to the weakening of both storms (Black et al., 2002). More generally, ancillary evidence of these downdrafts can commonly be seen as low-level arc clouds emanating away from sheared TCs on the upshear side (J. Dunion, personal communication).

In light of the observational and modeling evidence of ventilation, a theoretical framework is needed to assess the degree that these ventilation pathways are able to constrain a TC's intensity. A useful starting point is the body of steady-state, axisymmetric intensity theory (Malkus and Riehl, 1960; Emanuel, 1986; Holland, 1997; Bister and Emanuel, 1998). In doing so, one gains the benefit of a tractable framework afforded by a set of rigid assumptions, including axisymmetry, steadiness, and slantwise neutrality. Though sheared TCs are often asymmetric and unsteady in appearance, key insights in to how ventilation diminishes the symmetric component of TC's winds are still garnered through this idealized approach.

To begin with, a heuristic illustration of the ventilation process as a modification to the Carnot heat engine analogue of a tropical cyclone is given in section 2.2. Section 2.3 then details modifications to the potential intensity theory to account for ventilation. Section 2.4 examines the general behavior of a ventilated tropical cyclone. In section 2.5, the sensitivity to various parameters is assessed, followed by concluding remarks in section 2.6.

2.2 Carnot engine modification

Before deriving the theoretical framework, it is useful to think about ventilation's effect on TC intensity in a heuristic manner by considering the Carnot heat engine analogue of a TC (Emanuel, 1997, 2003). As shown in Fig. 2-2a, the secondary circulation can be divided in to the four steps of the Carnot cycle, which takes the form of a rectangle on a temperature-entropy diagram in Fig. 2-2b. The steps are (A) isothermal expansion in the inflow leg at the surface temperature, T_s; (B) adiabatic expansion up the eyewall at a large value of saturation moist entropy, s_e; (C) isothermal compression at the outflow temperature, T_o, as air radiates and subsides; and (D) following an absolute vortex line (a surface of constant absolute angular momentum) at an ambient value of saturation moist entropy, s_a. In lieu of following an actual air parcel in the last step, the Carnot cycle is closed by assuming there is little thermodynamic contribution along the absolute vortex line (Emanuel, 1991). The area contained within the rectangle A-B-C-D in Fig. 2-2b is the work the cycle performs.

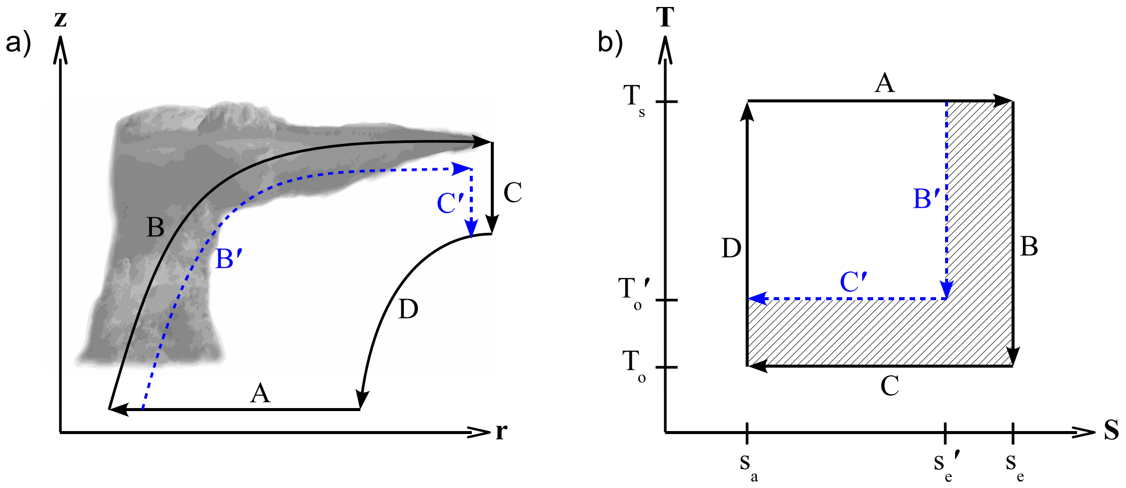

Figure 2-2: (a) The secondary circulation of an idealized TC, along with (b) the legs of the secondary circulation represented on a entropy-temperature diagram. A TC without ventilation travels along A-B-C-D, while a ventilated TC travels along A-B′-C′-D. The hatched region in (b) denotes the work lost due to ventilation.

Now consider the effect of ventilation on this Carnot heat engine analogue. Ventilating the eyewall via the midlevel pathway results in a local decrease in the entropy at midlevels along leg B. Given sufficient time, this perturbation is then spread by convective motions through a deep, slantwise layer, which is a consequence of the maintenence of subcloud layer quasi-equilibrium (Raymond, 1995). As a result, the entropy decreases from s_e to s_e' along leg B′. Additionally, the loss in system buoyancy (Smith et al., 2005) will correspond to a decrease in the outflow level or an increase in the outflow temperature from T_o to T_o' on leg C′. Now, consider ventilation via the low-level pathway whereby the TC boundary layer entropy is depressed by downdrafts in some region outside the eyewall. It is presumed that surface fluxes are unable to act to fully restore the entropy to its unperturbed value in the eyewall. Subsequently, the secondary circulation proceeds along the lower value of entropy, s_e', in the eyewall and the outflow occurs at a higher temperature, T_o', similar to the midlevel pathway.

In both cases, the effect is detrimental to the TC heat engine. This can be plainly seen in Fig. 2-2b on the $T-s$ diagram as the secondary circulation of a ventilated TC follows a modified path along A-B′-C′-D resulting in a smaller rectangle compared to the nonventilated TC. The difference in areas of the rectangles, given by the hatched area, represents the work lost due to ventilation; work that would otherwise be used to power the winds of a TC against frictional dissipation[2]. Ventilation, thus, works in two ways: it decreases the maximum difference between the ambient value of entropy and the eyewall entropy and it decreases the thermodynamic efficiency of the TC Carnot heat engine. Both of these are negative factors on TC intensity, and how much so will be examined in the next few sections.

2.3 Theoretical Framework

The derivation is based on conservation principles and closely parallels that of Bister and Emanuel (1998), hereafter BE98, with some major differences that will be highlighted. Throughout the derivation, axisymmetry and steadiness are assumed. Moreover, slantwise neutrality requires that the saturation isentropes be congruent to angular momentum surfaces.

The first law of thermodynamics for saturated conditions,

$$T\delta s^* = c_p \delta T + L_v \delta q^* - \alpha \delta p, \tag{2.1}$$

can be combined with the momentum equations to yield

$$T\delta s^* + \frac{M}{r^2}\delta M - \frac{\alpha}{r}\zeta\delta\psi = \delta(E + \frac{fM}{2}), \tag{2.2}$$

where c_p is the specific heat at constant pressure, L_v is the latent heat of vaporization, f is the Coriolis parameter, s is the specific moist entropy, T is the temperature, q is the water vapor mixing ratio, α is the specific volume, p is the pressure, $M = rv + 0.5fr^2$ is the absolute angular momentum, ζ is the azimuthal vorticity, ψ is the mass streamfunction, $E = c_pT + L_vq + gz + 0.5\left|\mathbf{u}\right|^2$ is the total energy, $\mathbf{u}$ is the wind velocity, g is the gravitational acceleration, r is the radius, z is the height, and any quantity with a star denotes the saturation value. Moreover, a pseudoadiabatic

---

[2] Some of the work is used to spin up the upper-level anticyclone as well, but to simplify matters, this effect will be ignored.

assumption is used, which implies the contribution of liquid water and ice to the entropy is ignored. Details on how to arrive at (2.2) are given in BE98.

The contribution of unbalanced flow is given by the third term in (2.2) containing $\delta\psi$. The storm deviates from gradient wind balance where this term is significant compared to the other terms, primarily in the eyewall. For instance, superintensity results when this term is positive, and the centrifugal force exceeds the pressure gradient force (Bryan and Rotunno, 2009a). In numerical simulations, it is possible to get superintense storms for certain combinations of numerical parameters, such as sufficiently small horizontal mixing length (Bryan and Rotunno, 2009b). Alternatively, Persing and Montgomery (2003) hypothesized that superintensity was caused by enhanced low-level entropy in the eye being drawn into the eyewall.

For the purposes of this study, the $\delta\psi$ term is ignored such that the precise problem to be explored is how ventilation reduces the TC's maximum achievable gradient wind. Albeit, one must keep in mind that unbalanced effects will modulate the full solution to some degree. However, since the goal is to describe the basic behavior of the intensity of ventilation-modified TC, unbalanced effects are likely not absolutely critical for the general picture. One could retain the $\delta\psi$ term and carry forward, but this produces an undesirable term that is a function of the internal state of the TC and is no longer closed (Bryan and Rotunno, 2009a).

The remaining terms are integrated around a closed circuit bounded by two isotherms, one in the outflow layer at $\overline{T_o}$ and one at the top of the boundary layer at T_h, and two saturation isentropes or isopleths of angular momentum encompassing the eyewall and adjacent region as illustrated in Fig. 2-3. The first and second terms on the left hand side in (2.2) only have contributions from the integration along isotherms while the term on the right hand side vanishes:

$$(T_h - \overline{T_o})\delta s^* + \int_{r_1}^{r_3} \frac{M}{r^2}\frac{\partial M}{\partial r} dr - \frac{1}{2r_o^2}\delta M^2 = 0. \tag{2.3}$$

The final term on the left hand side of (2.3) arises from the fact that it is evaluated at the outer radius of the storm, r_o. To evaluate (2.3), expressions for δs^* and δM

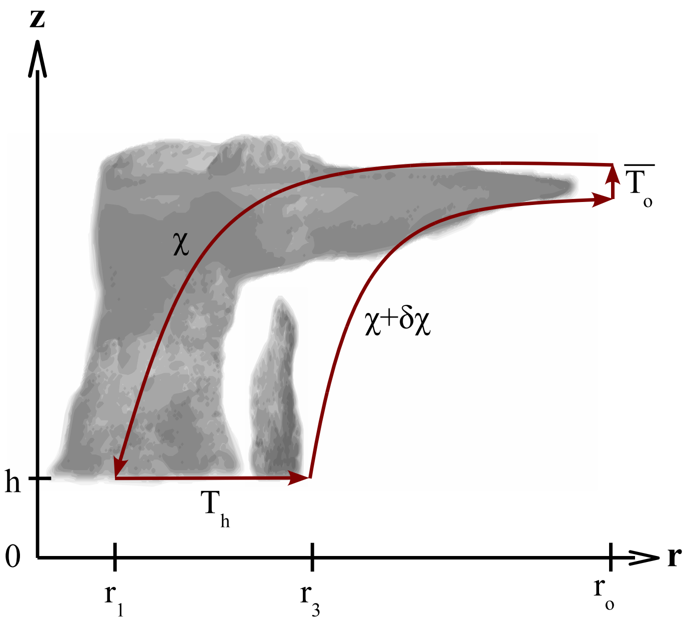

Figure 2-3: Closed circuit around which (2.2) is evaluated. Circuit consists of two isotherms, T_h and $\overline{T_o}$, and two contours of constant χ, where $\chi \in \{s^*, M, \psi\}$.

must be derived.

2.3.1 Subcloud layer entropy

Neutrality requires $\delta s^* = \delta s_b$, where s_b is the subcloud layer entropy. Hence, the entropy budget of the subcloud layer directly below the lowermost part of the integration circuit is required. In contrast to BE98, the subcloud layer is divided up in to two regions, as sketched in Fig. 2-4a: an "inner" region from r_1 to r_2 centered around the radius of maximum wind and an "outer" region from r_2 to r_3. Sources of entropy in both regions include turbulent fluxes, F_s, dissipative heating, H, and fluxes by the mean secondary circulation. In the outer region, convective entropy fluxes, $F_s(z = h) = \overline{w's'}$, through the top of the subcloud layer are included. Convective downdrafts, in particular, are driven by evaporation of rain into subsaturated air supplied by eddy entropy fluxes in the free troposphere, $\overline{\mathbf{u}'s'}$, as will be explained in the next subsection. Division of the domain in this manner represents a generaliza-

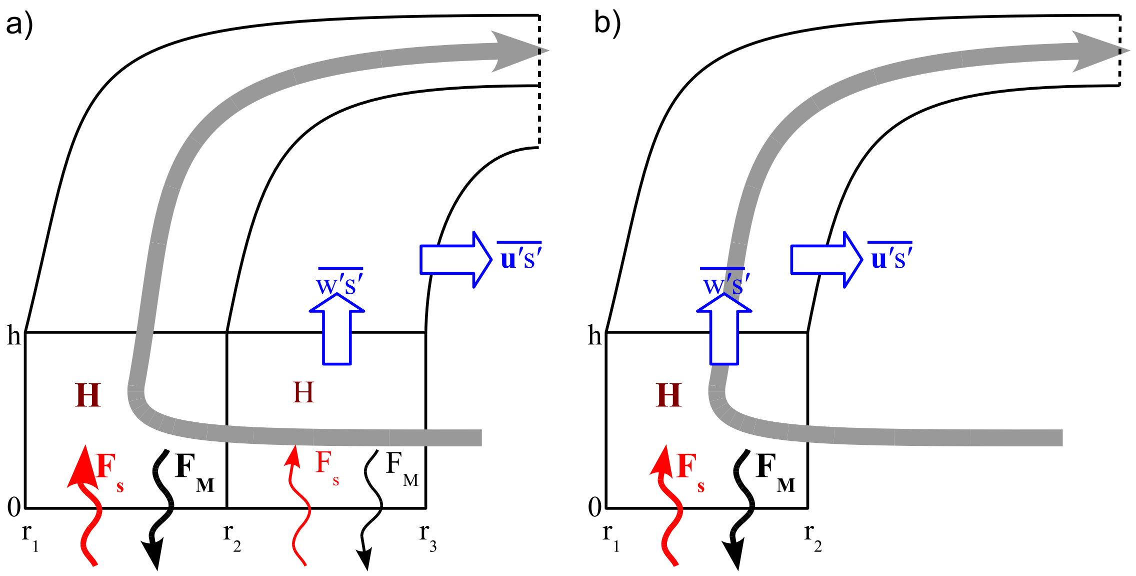

Figure 2-4: Sources and sinks of entropy and angular momentum in the subcloud layer and free troposphere for (a) the low-level pathway and (b) the midlevel pathway: surface fluxes of entropy, $F_s(z=0)$, and angular momentum, $F_M(z=0)$ (wavy arrows); dissipative heating, H; advection by the secondary circulation (gray arrow); convective entropy flux, $\overline{w's'}$ (vertical block arrow); and eddy entropy flux, $\overline{\mathbf{u}'s'}$, through outer angular momentum surface in the free troposphere (horizontal block arrow).

tion that can be used to study both the low-level and midlevel ventilation pathways sketched in Fig. 2-1.

In a steady state, the flux of entropy by the mean transverse circulation through the boundaries of the subcloud layer control volume must be equal to the sum of internal sources and sinks of entropy:

$$\int \mathbf{u}\rho s \cdot \mathbf{n} d\sigma = \int \left[-\frac{\partial}{\partial z}\left(\rho F_s\right) + \rho H \right] dV, \tag{2.4}$$

where $d\sigma$ is a surface integration element. To evaluate the left hand side of (2.4), the definition of the mass streamfunction,

$$(u, w) = \frac{1}{\rho r}\left(-\frac{\partial \psi}{\partial z}, \frac{\partial \psi}{\partial r}\right), \tag{2.5}$$

is substituted, and the resulting expression is integrated by parts. Assuming ψ vanishes at the surface and s is constant with height in the subcloud layer,

$$\int \mathbf{u}\rho s \cdot \mathbf{n} d\sigma = -2\pi \int_{r_1}^{r_3} \psi \frac{\partial s}{\partial r}\bigg|_h dr \approx -2\pi \overline{\psi} \delta s_b, \tag{2.6}$$

where h is the height of the subcloud layer. The last step in (2.6) approximates the integral using the average value of ψ at $z = h$ over the radial interval.

Next, the right hand side of (2.4) must be evaluated separately for the inner and outer regions. The aerodynamic flux formula is used for the surface flux of entropy:

$$F_s(z = 0) = C_k \left|\mathbf{u}\right| (s^*_{SST} - s_b), \tag{2.7}$$

along with the expression for the contribution of dissipative heating to the entropy equation from BE98:

$$\int_0^h H dz = \frac{C_D}{T_s} \left|\mathbf{u}\right|^3, \tag{2.8}$$

where C_k and C_D are the enthalpy and drag coefficients, s^*_{SST} is the saturation entropy at the sea surface temperature, and T_s is the surface temperature. Using (2.7) and (2.8) in the right hand side of (2.4) results in

$$\begin{aligned} \int \left[-\frac{\partial}{\partial z}(\rho F_s) + \rho H \right] dV = 2\pi \Bigg\{ &\int_{r_1}^{r_2} \left[\rho C_k \left|\mathbf{u}\right| (s^*_{SST} - s_b) + \frac{\rho C_D}{T_s} \left|\mathbf{u}\right|^3 \right] r dr \\ &+ \int_{r_2}^{r_3} \left[\rho C_k \left|\mathbf{u}\right| (s^*_{SST} - s_b) + \frac{\rho C_D}{T_s} \left|\mathbf{u}\right|^3 - \rho \overline{w's'} \right] r dr \Bigg\}. \end{aligned} \tag{2.9}$$

In order to arrive at a tractable expression, each integrand is assumed to be constant in each region. This approximation is applied by expressing $\mathbf{u}$ as some fraction of the maximum wind velocity, $\mathbf{u}_m$, and r as some proportion of the radius of maximum wind, r_m, in the following fashion:

$$\mathbf{u} = \begin{cases} \mathbf{u}_m & r_1 < r < r_2 \\ \gamma \mathbf{u}_m & r_2 < r < r_3 \end{cases}$$

$$r = \begin{cases} r_m & r_1 < r < r_2 \\ \alpha r_m & r_2 < r < r_3. \end{cases} \tag{2.10}$$

Two external parameters are introduced: γ $(0 \leq \gamma \leq 1)$ controls the radial wind decay and α $(\alpha \geq 1)$ controls the ratio of the width of both the inner and outer regions to the radius of maximum wind. Applying (2.10) in (2.9),

$$\int \left[-\frac{\partial}{\partial z} \left(\rho F_s \right) + \rho H \right] dV \approx 2\pi \rho r_m \delta r \left[C_k \left| \mathbf{u}_m \right| \left(s^*_{SST} - s^i_b \right) + \frac{C_D}{T_s} \left| \mathbf{u}_m \right|^3 \right. \\ \left. + C_k \alpha \gamma \left| \mathbf{u}_m \right| \left(s^*_{SST} - s^o_b \right) + \frac{C_D}{T_s} \alpha \gamma^3 \left| \mathbf{u}_m \right|^3 - \alpha \overline{w's'} \right], \tag{2.11}$$

where $\delta r = r_2 - r_1 = r_3 - r_2$, s^i_b is the subcloud layer entropy of the inner region, and s^o_b is the subcloud layer entropy of the outer region. The width of both regions is chosen to be equal to simplify the analysis and should have a value that is roughly the characteristic width of a TC's eyewall. The approximation obviously degrades if the width of each region is too large.

Equating (2.6) and (2.11) yields an expression for δs_b or, equivalently, δs^*:

$$\delta s^* = -\frac{\rho r_m \delta r}{\overline{\psi}} \left\{ C_k \left| \mathbf{u}_m \right| \left[(1 + \alpha\gamma) s^*_{SST} - (s^i_b + \alpha \gamma s^o_b) \right] + \frac{C_D}{T_s} (1 + \alpha \gamma^3) \left| \mathbf{u}_m \right|^3 - \alpha \overline{w's'} \right\}. \tag{2.12}$$

Next, s^i_b and s^o_b must be related to one another. A simple approach is to use an "upwind" like approximation where $s^o_b = s_a$, the entropy of air entering the outer region at r_3. An accurate value of s_a is ultimately needed to close the expression for the potential intensity, which requires information about the entropy of the ambient environment along with assumptions of processes that occur along the entire inflow leg (Emanuel, 1986). In this framework, an accurate value of s_a is not critical for the goal of understanding how ventilation causes differences between the steady-state intensity and potential intensity.

To get an expression for s_b^i, one must determine the entropy increase as air travels from r_3 to r_2. Consider the vertically averaged entropy equation in the subcloud layer:

$$< u > \frac{\partial s_b}{\partial r} = \frac{1}{h} \int_0^h \left(-\frac{\partial F_s}{\partial z} + H \right) dz. \tag{2.13}$$

where $< u >$ is the vertically averaged radial velocity in the subcloud layer. Using (2.7) and (2.8) and integrating from r_2 to r_3,

$$< u > (s_b^o - s_b^i) = \frac{1}{h} \int_{r_2}^{r_3} \left[-\overline{w's'} + C_k \left| \mathbf{u} \right| (s_{SST}^* - s_a) + \frac{C_D}{T_s} \left| \mathbf{u} \right|^3 \right] dr, \tag{2.14}$$

and after applying (2.10) and assuming the integrands are constant, s_b^i can be expressed as

$$s_b^i = s_b^o - \frac{\delta r}{< u > h} \left[-\overline{w's'} + C_k \gamma \left| \mathbf{u}_m \right| (s_{SST}^* - s_a) + \frac{C_D}{T_s} \gamma^3 \left| \mathbf{u}_m \right|^3 \right]. \tag{2.15}$$

The difference in entropy between the outer and inner regions is controlled by entropy fluxes at the top and bottom of outer region's subcloud layer, dissipative heating, the depth of the subcloud layer, and the mean advection timescale for parcels to travel across the outer region (i.e. $\delta r / < u >$).

In order to have as few externally set parameters as possible, $< u >$ can be estimated by considering the vertically averaged, steady angular momentum equation for a well-mixed subcloud layer:

$$\frac{1}{h}\int_0^h u\frac{\partial M}{\partial r}dz = \frac{1}{h}\int_0^h -\frac{\partial F_M}{\partial z}dz. \tag{2.16}$$

F_M, the turbulent flux of angular momentum, at the surface is given by the aerodynamic flux formula:

$$F_M(z=0) = -C_D\left|\mathbf{u}\right| rv, \tag{2.17}$$

where v is the azimuthal velocity. Upon evaluating (2.16) with the assumption that $M \approx rv$ and applying (2.17) followed by (2.10), an expression for $< u >$ in the outer region is obtained:

$$< u >\approx -\frac{C_D\gamma\left|\mathbf{u}_m\right|\alpha r_m}{h}. \tag{2.18}$$

Substituting (2.18) into (2.15) and noting that $\alpha \equiv 1 + \delta r/r_m$,

$$\begin{aligned} s_b^i &= s_b^o + \Delta s = s_a + \Delta s \\ \Delta s &= \frac{\alpha - 1}{C_D\alpha\gamma\left|\mathbf{u}_m\right|}\left[-\overline{w's'} + C_k\gamma\left|\mathbf{u}_m\right|(s^*_{SST} - s_a) + \frac{C_D}{T_s}\gamma^3\left|\mathbf{u}_m\right|^3\right]. \end{aligned} \tag{2.19}$$

2.3.2 Free troposphere entropy

Convective fluxes, particularly downdrafts, are a key ingredient in the subcloud layer entropy budget in the outer region. Ventilation manifests itself through these downdrafts that are driven by the evaporation of precipitation into subsaturated air. However, it remains to be seen how the direct effect of ventilation, namely radial eddy fluxes of entropy in the free troposphere, is connected to these convective fluxes through the top of the subcloud layer. Precisely connecting radial to convective fluxes is non-trivial as it requires treatment of microphysical processes.

However, microphysical considerations can be circumvented by applying the assumption of steadiness, which requires there be no net flux of entropy through the sides of any control volume in the absence of internal sources and sinks of entropy.

Taking the control volume to be the free troposphere above the outer region (upper right region in Fig. 2-4a), the two prescribed fluxes that must be in balance are an inward eddy flux of low-entropy air and evaporatively cooled downdrafts at the cloud base. The latter is present if the column remains convectively active as to maintain slantwise neutrality. If so, there is a one-to-one correspondence between these two transient fluxes:

$$2\pi \int_{r_2}^{r_3} \rho \overline{w's'} r dr = \int_{M_o} \rho \overline{\mathbf{u}'s'} \cdot \mathbf{n} d\sigma. \tag{2.20}$$

Only radial eddy fluxes of entropy through the outer angular momentum surface, M_o, are considered in this case. Moreover, irreversible sources of entropy, such as that due to mixing or evaporation, have been neglected. Evaluating the left hand side using (2.10) along with the constant integrand assumption and solving for $\overline{w's'}$,

$$\overline{w's'} = \frac{1}{2\pi \rho \alpha r_m \delta r} \int_{M_o} \rho \overline{\mathbf{u}'s'} \cdot \mathbf{n} d\sigma \equiv \mathcal{V}. \tag{2.21}$$

The ventilation, $\mathcal{V}$, is defined as the integrated eddy flux of entropy perpendicular to the outer angular momentum surface scaled by the downdraft area. Henceforth, $\mathcal{V}$ is substituted where $\overline{w's'}$ appears in (2.12) and (2.19).

2.3.3 Subcloud layer angular momentum

The subcloud layer angular momentum budget proceeds similar to the entropy budget derivation. In a steady state, the flux of angular momentum through the boundaries of each subcloud layer region must be equal to the turbulent flux of angular momentum at the surface as sketched in Fig. 2-4a. The fundamental equation for this balance is given by

$$\int \mathbf{u} \rho M \cdot \mathbf{n} d\sigma = \int -\frac{\partial \rho F_M}{\partial z} dV. \tag{2.22}$$

In the outer region, the convective flux of angular momentum is neglected in order to isolate the thermodynamic effect of ventilation, though it should be noted that convective fluxes of angular momentum at the top of the subcloud layer have been shown to locally increase the entropy gradient and hence the maximum tangential winds within the boundary layer by 5-10% in numerical simulations (O. Pauluis and A. Mrowiec 2008, personal communication). Evaluation of (2.22) for each region proceeds similarly to the derivation for (2.12). With the use of (2.10) and (2.17),

$$\delta M = \begin{cases} \frac{r_m^2 \delta r}{\overline{\psi}} \rho C_D \left|\mathbf{u}_m\right| v_m & r_1 < r < r_2 \\ \frac{\alpha^2 r_m^2 \delta r}{\overline{\psi}} \rho C_D \gamma^2 \left|\mathbf{u}_m\right| v_m & r_2 < r < r_3. \end{cases} \tag{2.23}$$

Additionally, $\overline{\psi}$ in each region is assumed to be approximately equal since the mean vertical velocity, and thus $\partial\overline{\psi}/\partial r$, is assumed to be small at the top of the subcloud layer in the outer region[3].

2.3.4 Steady-state intensity

All the pieces needed to evaluate the terms in (2.3) have now been derived. Combining (2.12), (2.19), and (2.21) in the first term; (2.23) and assuming $M \approx rv$ in the second term; and ignoring the third term for large r_o results in

$$\begin{aligned} -(T_h - \overline{T_o})\frac{\rho r_m \delta r}{\overline{\psi}} \left\{ C_k \left|\mathbf{u}_m\right| \left[(1+\alpha\gamma)\left(s^*_{SST} - s_a\right) - \Delta s \right] + \frac{C_D}{T_s}(1+\alpha\gamma^3)\left|\mathbf{u}_m\right|^3 - \alpha\mathcal{V} \right\} \\ + \int_{r_1}^{r_2} \frac{v}{r}\frac{r_m^2}{\overline{\psi}} \rho C_D \left|\mathbf{u}_m\right| v_m dr + \int_{r_2}^{r_3} \frac{v}{r}\frac{\alpha^2 r_m^2}{\overline{\psi}} \rho C_D \gamma^2 \left|\mathbf{u}_m\right| v_m dr = 0. \end{aligned} \tag{2.24}$$

Evaluating the integrals using (2.10) and simplifying,

$$\begin{aligned} -(T_h - \overline{T_o}) \left\{ C_k \left|\mathbf{u}_m\right| \left[(1+\alpha\gamma)\left(s^*_{SST} - s_a\right) - \Delta s \right] + \frac{C_D}{T_s}(1+\alpha\gamma^3)\left|\mathbf{u}_m\right|^3 - \alpha\mathcal{V} \right\} \\ + C_D \left|\mathbf{u}_m\right| v_m^2 (1+\alpha\gamma^3) = 0. \end{aligned} \tag{2.25}$$

---

[3] An more accurate derivation would use (B.1) and (2.18) to derive an expression for $\overline{\psi}$ in each separate region. For the inner region, $\overline{\psi} = \rho C_D \left|\mathbf{u}_m\right| r_m^2$; and for the outer region, $\overline{\psi} = \alpha^2 \gamma \rho C_D \left|\mathbf{u}_m\right| r_m^2$. Note that this change must also be applied in the preceding sections wherever $\overline{\psi}$ appears in order to be consistent. Nonetheless, it appears that there is still quite a bit of cancellation in the end.

The first term in the curly braces represents the energy source due to the air-sea disequilibrium with a modification factor, given by Δs, that increases the disequilibrium in the presence of downdrafts and decreases the disequilibrium due to entropy sources in the outer region. The second term is the recycling effect of dissipative heating that increases the wind speed, as noted by BE98. The final term in the curly braces represents the power sink due to ventilation. The last term in (2.25) is the power dissipated by friction in the TC subcloud layer.

Thus far, the framework presented resembles the low-level ventilation pathway only. However, specifying $\alpha = 1$ and $\gamma = 0$ transforms the framework into one describing the midlevel ventilation pathway as shown in Fig. 2-4b. Setting $\alpha = 1$ superposes the processes in the outer region on top of those in the inner region. Ventilation now occurs through the angular momentum surface bounding the inner region (eyewall), and convective fluxes act to redistribute entropy changes through the entire eyewall as saturation is maintained. Moreover, setting $\gamma = 0$ is necessary in order to prevent a double counting of surface fluxes, dissipation, and dissipative heating in the subcloud layer. The midlevel ventilation pathway is therefore a special case of the more general framework.

As is done in BE98, it is assumed that $T_h \approx T_s$ and $v_m \approx |\mathbf{u}_m|$. Upon expanding Δs and rearranging (2.25) in to a cubic polynomial in $|\mathbf{u}_m|$,

$$\begin{aligned}
&\left[\left(\frac{T_s - \overline{T_o}}{T_s}\right)\frac{C_k(\alpha-1)\gamma^2}{\alpha} + \frac{\overline{T_o}}{T_s}C_D(1+\alpha\gamma^3)\right]|\mathbf{u}_m|^3 \\
&+ (T_s - \overline{T_o})C_k\left(s^*_{SST} - s_a\right)\left[-(1+\alpha\gamma) + \frac{C_k(\alpha-1)}{C_D\alpha}\right]|\mathbf{u}_m| \\
&+ (T_s - \overline{T_o})\left[-\frac{C_k(\alpha-1)}{C_D\alpha\gamma} + \alpha\right]\mathcal{V} = 0. \qquad (2.26)
\end{aligned}$$

For the trivial case where there is no ventilation ($\mathcal{V} = 0$), the steady-state intensity is simply equal to the potential intensity:

$$\left|\mathbf{u}_{PI}^{I}\right|^2 = \frac{(T_s - \overline{T_o})C_k\left(s_{SST}^{*} - s_a\right)\left[(1+\alpha\gamma) - \frac{C_k(\alpha-1)}{C_D\alpha}\right]}{\left(\frac{T_s-\overline{T_o}}{T_s}\right)\frac{C_k(\alpha-1)\gamma^2}{\alpha} + \frac{\overline{T_o}}{T_s}C_D(1+\alpha\gamma^3)}, \tag{2.27}$$

which looks different from the expression in BE98. However, superposing the inner and outer regions by setting $\alpha = 1$ and $\gamma = 0$ collapses the current framework in to that used by BE98 and results in their expression for the potential intensity:

$$\left|\mathbf{u}_{PI}^{II}\right|^2 = \frac{T_s(T_s - \overline{T_o})}{\overline{T_o}}\frac{C_k}{C_D}\left(s_{SST}^{*} - s_a\right). \tag{2.28}$$

The difference between the potential intensities using (2.27) and (2.28) turns out to be quite small ($< 10\%$) for plausible combinations of α and γ, implying that the balance between surface fluxes and dissipation solely near the radius of maximum wind is sufficient for potential intensity estimates versus needing to consider the balance over a larger region of the TC.

Using (2.27) or (2.28), two expressions for the steady-state intensity are presented when $\mathcal{V} \neq 0$. First, the steady-state intensity for the low-level pathway whereby the boundary layer is flushed with low-entropy air from downdrafts outside the eyewall is

$$\left|\mathbf{u}_m\right|^3 = \left|\mathbf{u}_{PI}^{I}\right|^2\left|\mathbf{u}_m\right| - \frac{(T_s - \overline{T_o})\left[-\frac{C_k(\alpha-1)}{C_D\alpha\gamma} + \alpha\right]}{\left(\frac{T_s-\overline{T_o}}{T_s}\right)\frac{C_k(\alpha-1)\gamma^2}{\alpha} + \frac{\overline{T_o}}{T_s}C_D(1+\alpha\gamma^3)}\mathcal{V}. \tag{2.29}$$

Second, the steady-state intensity for the midlevel pathway whereby the eyewall is directly ventilated can be represented by letting $\alpha = 1$ and $\gamma \to 0$, and (2.26) reduces to

$$\left|\mathbf{u}_m\right|^3 = \left|\mathbf{u}_{PI}^{II}\right|^2\left|\mathbf{u}_m\right| - \frac{T_s(T_s - \overline{T_o})}{\overline{T_o}}\frac{1}{C_D}\mathcal{V}. \tag{2.30}$$

2.4 Behavior of a ventilated TC

Along with the heuristic picture presented in section 2, a quantitative framework for assessing midlevel ventilation's constraint on the maximum achievable steady-state gradient wind has been devised in the form of (2.29) and (2.30). To evaluate the behavior of both equations, it is convenient to nondimensionalize the wind speed by the potential intensity, as given by (2.27) or (2.28) depending on the pathway of interest, and the ventilation by the value of $\mathcal{V}$ where the discriminant of the cubic polynomial vanishes:

$$\mathcal{V}_{thresh} = \frac{2}{3\sqrt{3}} \frac{\left|\mathbf{u}_{PI}^{I\mathrm{or}II}\right|^3}{|\xi|}, \tag{2.31}$$

where ξ is the coefficient in front of $\mathcal{V}$ in (2.29) or (2.30). The resulting nondimensionalization,

$$\begin{aligned} |\mathbf{u}_m| &\to \left|\mathbf{u}_{PI}^{I\mathrm{or}II}\right| u^\dagger \\ \mathcal{V} &\to \mathcal{V}_{thresh} \mathcal{V}^\dagger, \end{aligned} \tag{2.32}$$

when substituted into either (2.29) or (2.30) results in

$$u^{\dagger 3} = u^\dagger - \frac{2}{3\sqrt{3}} \mathcal{V}^\dagger, \tag{2.33}$$

where the dagger denotes a nondimensional variable.

Solving (2.33) results in up to three steady-state intensities for a ventilated TC, but only positive, real solutions are shown in Fig. 2-5. The first solution branch is given by the solid line. It begins at a normalized intensity of one (the potential intensity) and decreases monotonically as the ventilation increases, with the intensity decrease accelerating for larger values of ventilation. The second branch is given by the dashed line starting at 0 $\mathrm{m\,s^{-1}}$ and increases in intensity as the ventilation increases.

The physicality of these equilibrium solutions can be elucidated by considering the stability of each branch. Evaluating the residual of (2.25) as a function of $|\mathbf{u}_m|$ and $\mathcal{V}$ for an arbitrary set of parameters and then nondimensionalizing gives a stability

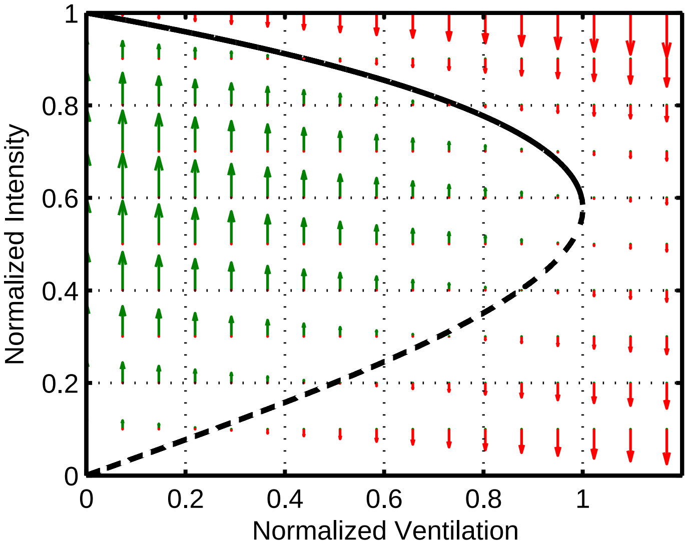

Figure 2-5: Normalized equilibrium solutions (solid and dashed lines) for the steady-state intensity of a ventilated TC. Arrows denote intensifying and weakening TCs for off-equilibrium values of nondimensional ventilation and intensity.

diagram as depicted by the arrows in Fig. 2-5. Arrows pointing up indicate net energy generation and a strengthening TC while those pointing down indicate net energy dissipation and a weakening TC. Along the equilibria branches, the net energy generation must of course vanish. The arrows converge toward the first, solid solution branch indicating that it is a stable equilibrium. Conversely, the arrows diverge from the second, dashed solution branch indicating that it is an unstable equilibrium so that it is, in fact, an unobservable solution. Consequently, the only steady-state solution that may be observed is given by the first branch.

However, the unstable branch is useful in that it delineates intensifying and weakening regions in the $\mathcal{V}^{\dagger}$ and $u^{\dagger}$ phase space. Thus, the unstable equilibrium can be interpreted as the initial amplitude a TC needs in order to survive and grow in the face of ventilation. For large values of ventilation, the initial amplitude can exceed half the potential intensity.

For a normalized ventilation equal to one, representing the threshold ventilation value, the steady-state intensity is reduced to 58% of the potential intensity. Beyond this, the ventilation exceeds $\mathcal{V}_{thresh}$, and no steady tropical cyclone can exist. Hence,

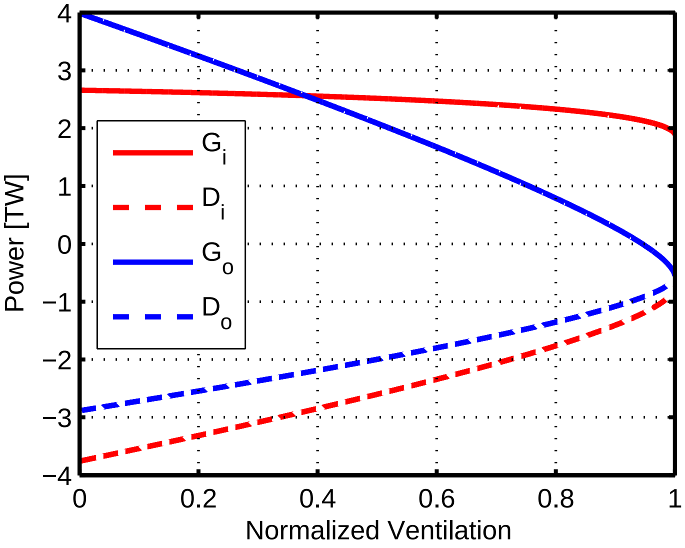

Figure 2-6: Power generation and dissipation in the subcloud layer due to the combination of surface entropy fluxes, dissipative heating, and convective entropy fluxes (G) and friction (D). Subscript 'i' refers to inner region while 'o' refers to outer region.

$\mathcal{V}_{thresh}$ marks the boundary between potential growth and absolute decay of a TC.

2.4.1 Energy budget

The monotonic decrease in intensity with increasing ventilation and threshold behavior noted in Fig. 2-5 can be explained further by examining the energy generation budget within the subcloud layer as shown in Fig. 2-6 for the more general low-level ventilation pathway. In this calculation, $|\mathbf{u}_{PI}| = 100$ m s^{-1}, $T_s = 28$°C, $\overline{T_o} = -70$°C, $C_k = C_D = 3 \times 10^{-3}$, $\alpha = 1.5$, and $\gamma = 0.8$. The power generation due to surface entropy fluxes, dissipative heating, and convective entropy fluxes (terms in curly braces in (2.25)) are grouped together and denoted as G_x while the power loss due to frictional dissipation (final term in (2.25)) is denoted as D_x, where $x = i$ corresponds to the inner region and $x = o$ to the outer region.

For low values of ventilation, convective entropy fluxes in the outer region are weak and surface fluxes dominate the budget, yielding positive power generation to balance out the frictional dissipation in both regions. As ventilation increases, G_o decreases quickly as downdrafts flush the subcloud layer with greater amounts of low entropy leaving G_i to bear more of the burden in maintaining the TC's winds against dissipation. Once the normalized ventilation approaches one, G_o actually becomes negative as downdrafts completely overwhelm surface entropy fluxes and dissipative heating in the outer region. Now, only G_i can sustain the mechanical energy generation combating both the power dissipation due to friction and downdrafts. Ultimately, increasing the ventilation beyond the threshold level overwhelms G_i leading to absolute decay.

A key component of G_i is the recovery of downdraft air due to the increased air-sea thermodynamic disequilibrium. Examining (2.29) reveals that the recovery of downdraft air reduces the ventilation term by a factor of $C_k(\alpha-1)/(C_D\alpha\gamma)$. Increasing C_k or α increases the magnitude and area over which surface fluxes act to restore the downdraft-modified air back to unperturbed values. On the other hand, increasing C_D or γ increases the frictionally driven inflow and reduces the time available for surface fluxes to act. The available recovery time is an important variable also highlighted by Powell (1990) where the short trajectories of downdraft-modified boundary layer parcels in Hurricane Floyd (1981) contributed to the incomplete recovery of parcels as they spiraled in toward the radius of maximum wind.

In contrast to the low-level pathway, the midlevel pathway is more deleterious as there is no possibility of modification of the low-entropy air by surface fluxes before reaching the eyewall. One way of seeing this effect is to eliminate the recovery term in (2.29) by removing $-C_k(\alpha - 1)/(C_D\alpha\gamma)$ from the numerator of the ventilation coefficient. Since this factor is negative definite, its elimination will increase the magnitude of the ventilation term. In terms of energetics, this corresponds to a more severe reduction of G_i as the power generation in the inner region must now battle both dissipation and ventilation directly leading to more than a 40% decrease in the ventilation threshold compared to that of the low-level pathway.

2.4.2 Midlevel pathway in Hurricane Bonnie (1998)

Cram et al. (2007) studied Lagrangian back trajectories of parcels from an origin point in the eyewall of a numerical simulation of Hurricane Bonnie (1998), which at the time was subjected to approximately 12 m s^{-1} of deep layer environmental vertical shear[4] and had a fairly steady intensity. An estimate of the ventilation can be obtained by examining the characteristics of their "class IV," midlevel ventilation parcels. Trajectories show that parcels had a radial velocity of approximately -2 to -4 m s^{-1} while the entropy perturbations were approximately -10 to -12 J (kg K)$^{-1}$. From their figures, it is deduced that $r_m \approx 40$ km, $\delta r \approx 10$ km, $\rho \approx 1$ kg m^{-3} at cloud base, $\rho \approx 0.75$ kg m^{-3} in the ventilating layer, the radius at which ventilation occurs is about 50 km, and the depth of the ventilation layer is about 2 km. Assuming the effect of the slope of the angular momentum surface is small, plugging all these values into (2.21) and setting $\alpha = 1$ yields an estimate of the ventilation, $\mathcal{V}$, of $3.7 - 9$ m s^{-1} J (kg K)$^{-1}$. However, ventilation only occurs in the upshear semicircle of the storm, hence the effective ventilation is estimated to be half this range, or between $1.8 - 4.5$ m s^{-1} J (kg K)$^{-1}$.

Ideally, the next step would be to calculate a ventilation modified steady-state intensity using (2.30) to compare to the simulated maximum intensity of about 55 m s^{-1}. However, this requires knowledge of the *model's* potential intensity, which is not only a function of the background thermodynamic state but also the configuration of the model itself including its resolution and turbulence parameterization (Rotunno et al., 2009). Using the background state only, the potential intensity in the simulation of Bonnie is estimated to range anywhere from $27 - 74$ m s^{-1} depending on the ratio of exchange coefficients, the relative humidity in the boundary layer, and the background sounding. The lower end of the potential intensity range is estimated using a surface relative humidity of 90% and a ratio of C_k to C_D of 0.35. The upper end of the potential intensity range is estimated using a pre-storm sounding from NCEP/NCAR reanalysis data at Bonnie's position on Aug. 23, 1998 at 12Z, pseudoadiabatic assumptions, and a ratio of C_k to C_D of 0.65. For instance, using the upper limit of the potential intensity range along with $T_s = 30°\text{C}$, $\overline{T_o} = -63°\text{C}$, and $C_D = 2 \times 10^{-3}$ would yield a ventilation modified steady-state intensity of $47 - 65$ m s^{-1}, which en-

---

[4] The metric for vertical shear is the magnitude of the vector difference between the environmental winds at upper- and low-levels of the troposphere, usually 200 hPa and 850 hPa.

compasses the simulated intensity of Bonnie[5]. On the other hand, using the lower half of the potential intensity range would yield no steady TC as the ventilation threshold would be exceeded.

It should be emphasized that even with knowledge of the model's potential intensity, there remain a few caveats which must be highlighted. The ventilation calculation assumes that eddies and convective motions are 100% efficient at transferring the low entropy through a deep layer in the eyewall. If evaporation of rain in subsaturated air does not occur, the low-entropy air may simply enter and exit the eyewall region without much modification, leading to a reduction in the eddy entropy flux efficiency. Also, given that the standard deviation of the entropy perturbations is quite large in the Cram et al. (2007) study, the actual covariance between u' and s' may be significantly different from simply using the means of each to get a ballpark estimate. More precise accounting of parcels would be needed to obtain an accurate value of the ventilation parameter $\mathcal{V}$. Lastly, since the theory only accounts for the maximum gradient wind, unbalanced forces may play a role in allowing the storm to survive even though the theoretical ventilation-modified intensity suggests otherwise, i.e. the ventilation threshold may be significantly higher for a superintense storm.

2.4.3 Interactive thermodynamic efficiency

In the analysis up to this point, the thermodynamic efficiency was held fixed, but ventilation acts to reduce the buoyancy of eyewall parcels relative to the environment causing the outflow temperature to increase. Such shallowing of the TC structure is supported by composited satellite derived analyses of sheared TCs (Knaff et al., 2004).

The outflow temperature is defined as the entropy-weighted temperature along surfaces of angular momentum or saturation entropy where they flare out to large radii:

---

[5] Dissipative heating is excluded from the model and the ventilation modified stead-state intensity calculation. This effectively causes $\overline{T_o}$ in the denominator of the thermodynamic efficiency in second term on the right hand side of (2.30) to be replaced by T_s

$$\overline{T_o} = \frac{1}{s_{max} - s_{min}} \int_{s_{min}}^{s_{max}} T_o ds \tag{2.34}$$

where s_{min} and s_{max} are the minimum and maximum entropy in the TC's subcloud layer. The methodology for applying (2.34) to a sounding is elaborated upon in appendix B.

Using the Jordan hurricane season mean sounding (Jordan, 1958), the outflow temperature and height as a function of the normalized ventilation is shown in Fig. 2-7 for the low-level pathway. The same figure for the midlevel pathway is nearly identical. For no ventilation, the average outflow temperature is about −68°C corresponding to a thermodynamic efficiency, $(T_s - \overline{T_o})/\overline{T_o}$, of 0.46. As ventilation increases, the outflow temperature warms and the outflow height lowers. As the ventilation threshold is neared, the outflow temperature increases more rapidly as s_{min} decreases below s_a and less buoyant parcels are included in the calculation of $\overline{T_o}$. Consequently, the efficiency is reduced to 0.42 at the ventilation threshold. Knaff et al. (2004) noted the height of the balanced vortex is approximately 1 km shallower in high-shear storms compared to low-shear storms, which is consistent with the change in outflow height between relatively low and high amounts of ventilation.

In comparison with fixed thermodynamic efficiency, the normalized intensity when the thermodynamic efficiency interacts with ventilation is depicted in Fig. 2-8. For most values of ventilation, the efficiency change contributes approximately 5 - 10% to the total intensity decrease from the potential intensity, but once the ventilation becomes large, the percentage becomes much more significant. Once $\mathcal{V}^{\dagger} > 0.9$, the contribution increases from 10% to 25% in exponential fashion.

The decreased thermodynamic efficiency is also responsible for increasing the equilibrium values along the unstable branch (not shown), which corresponds to a higher minimum intensity needed for sustainability. This change is more pronounced for larger values of ventilation. Moreover, the decrease in efficiency reduces the ventilation threshold value by a small margin over the threshold when the thermodynamic efficiency is held fixed.

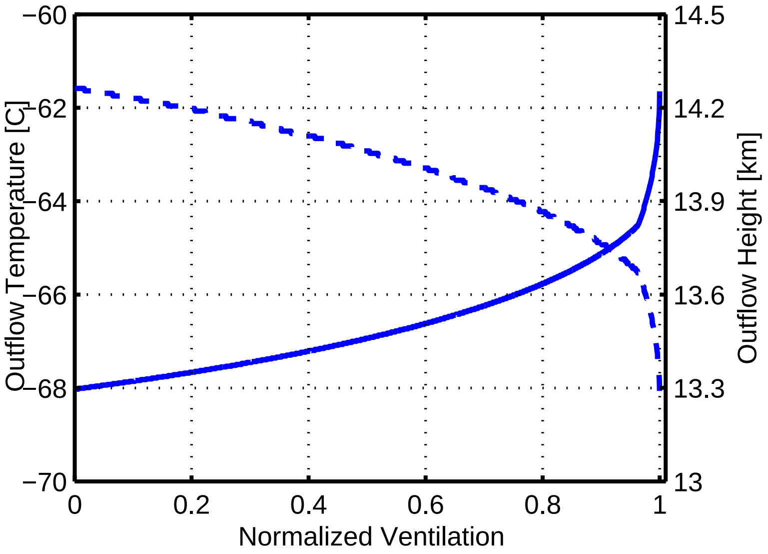

Figure 2-7: Outflow temperature (solid) and height (dashed) for a ventilated TC using the Jordan hurricane season mean sounding.

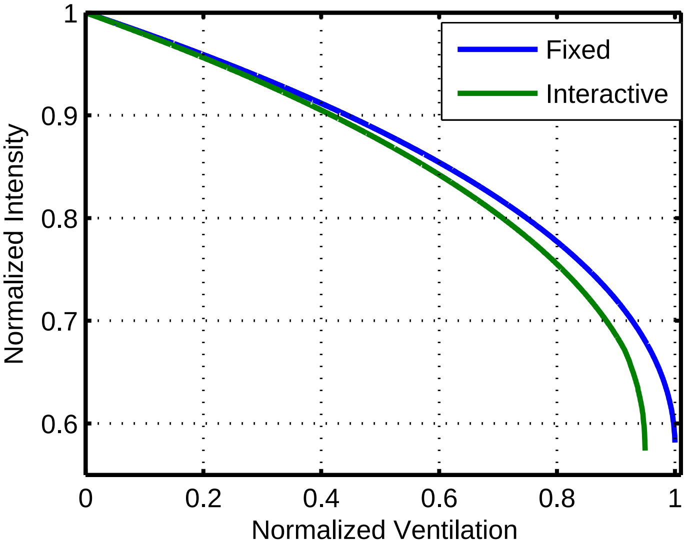

Figure 2-8: Normalized steady-state intensity for fixed efficiency (blue) and interactive efficiency (green).

2.5 Sensitivity to parameters

2.5.1 Potential intensity

The nondimensional form of the steady-state intensity of a ventilated tropical cyclone lacks any reference to the potential intensity, implying that the nondimensional formulation is invariant across all background thermodynamic states. This arises due to the normalization of the ventilation by the cube of the potential intensity in (2.32) via (2.31). Differing degrees of feedback between the thermodynamic efficiency and the ventilation introduces a nominal amount of variance in the normalized intensity between thermodynamic states, especially as the ventilation approaches the threshold value, but this effect can mostly be ignored.

It is important to keep in mind the actual ventilation can affect tropical cyclones embedded in different thermodynamic states quite differently, as shown in Fig. 2-9 for a range of mean tropical maritime soundings binned by sea surface temperature. The soundings are composited using 15 years of northern hemisphere July-October NCEP/NCAR reanalysis data (Kalnay et al., 1996). The same value of ventilation can conceivably yield a strong TC in the more favorable thermodynamic environment and no steady TC in the other, depending on whether the respective ventilation threshold has been exceeded. To observe the invariance across the environments, one must scale the intensity by the potential intensity and the ventilation by the ventilation threshold, transforming the family of curves in Fig. 2-9 to the single curve in Fig. 2-5.

2.5.2 Alpha and gamma

The sensitivity of the framework to the two parameters, α and γ, is now assessed. Recall that α controls the ratio of the width of the eyewall and downdraft regions to the radius of maximum wind, and γ controls the radial decay of the wind velocity from the inner to outer regions. Given that the potential intensity only varies slightly over the plausible range of α and γ, the sensitivity can be assessed by simply examining

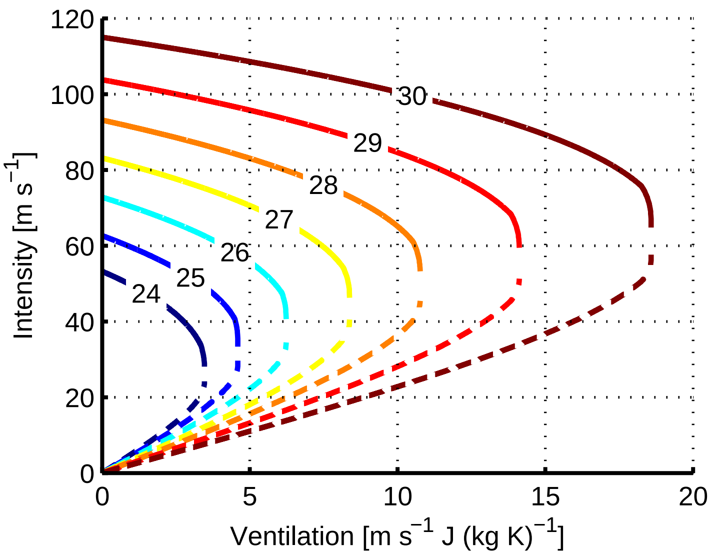

Figure 2-9: Steady-state intensity curves with interactive efficiency for various thermodynamic environments binned by SST.

the coefficient in front of $\mathcal{V}$ in (2.29) as a function of α and γ while holding $T_s = 28°\text{C}$, $\overline{T_o} = -70°\text{C}$, and $C_k = C_D = 3 \times 10^{-3}$ as shown in Fig. 2-10. Combinations of α and γ that yield inertially unstable configurations are blacked out.

Increasing α allows a greater amount of low-entropy air to infiltrate the subcloud layer. However, increasing α also allows for greater surface fluxes and recovery of downdraft air. For relatively high values of γ, these effects offset one another and there are only modest changes to the ventilation coefficient as α varies. For smaller values of γ, the sensitivity of the ventilation coefficient to α increases as smaller surface fluxes in the outer region are unable to promote as much recovery of downdraft air.

Over most of the parameter phase space, the ventilation coefficient is more sensitive to γ. As previously mentioned, γ controls the recovery of downdraft air with larger values of γ diluting the detrimental effects of downdrafts. Additionally, the frictionally induced inflow, and hence the inverse of the advective timescale ($\delta r / < u >$), is also directly proportional to γ. For relatively large α, decreasing γ beyond a certain value results in a decrease in the ventilation coefficient as the large advective timescale more than compensates the small surface fluxes in the outer region.

The above results are somewhat sensitive to the ratio of C_k to C_D. Reducing the

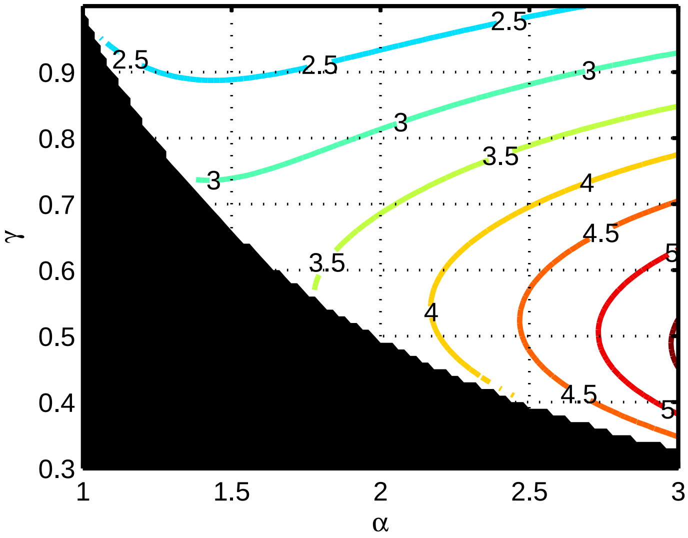

Figure 2-10: Ventilation coefficient in (2.29) as a function of α and γ. Values are divided by 10^4. Inertially unstable combinations of α and γ are blacked out.

ratio to 0.5 results in an increase in the ventilation coefficient by roughly a factor of two through all the parameter space in Fig. 2-10 (not shown). Surface fluxes are unable to increase the entropy of downdraft-modified air as rapidly in the amount of time it takes a parcel to reach the eyewall, which makes the TC more sensitive to the ventilation. Moreover, at large α and small γ, the ventilation coefficient does not show a pronounced maximum axis because the entropy recovery timescale is still large relative to the advective timescale.

Note that the nondimensional formulation is independent of α, γ, C_k, and C_D. Therefore, none of these parameters affect the shape of the steady-state intensity curve in nondimensional space.

2.6 Conclusions

In the Carnot heat engine analogue of a tropical cyclone, ventilation acts to reduce the maximum entropy obtained in the eyewall of the TC and reduces the thermodynamic efficiency, resulting in a decrease in the total amount of work that can be performed by the TC to combat frictional dissipation. We developed an idealized framework for analyzing the consequences of ventilation via two pathways. The first is a low-level pathway where rain evaporating into dry air aloft produces low-entropy downdrafts that are swept inwards by the radial inflow in the subcloud layer, and the second is a midlevel pathway where eddies flux low-entropy air directly into the eyewall.

Qualitatively, the behavior captured by the solutions of the analytical formulation mimics some of the gross behavioral aspects of sheared TCs. The most apparent aspect is that the maximum attainable intensity is reduced up to 58% of the potential intensity as the ventilation becomes stronger. Secondly, there is a theoretical ventilation threshold beyond which a steady tropical cyclone cannot be maintained and only a trivial solution is possible (i.e. one with no tropical cyclone at all). This is analogous to cases when the vertical wind shear overwhelms a tropical cyclone, resulting in its quick demise. Additionally, this may also explain why there are very few TCs observed for vertical wind shears greater than 20 $\mathrm{m\,s^{-1}}$ (Zeng et al., 2007, 2008). Lastly, for nonprohibitive magnitudes of ventilation, there is an unstable equilibrium intensity separating growing and decaying TCs, which may be a reason why stronger and weaker storms respond differently to comparatively similar magnitudes of vertical wind shear (DeMaria et al., 2005).

The outflow temperature is affected by a shallowing of the TC's eyewall convection, as its buoyancy relative to the background environment is reduced due to ventilation. This results in a reduction in the thermodynamic efficiency, which serves to compound the effects of ventilation. This is especially severe for large values of ventilation, where 10 - 25% of the total weakening relative to the potential intensity can be attributed to ventilation's feedback on the thermodynamic efficiency.

TCs in environments with more favorable thermodynamic profiles, i.e. with higher potential intensities, are able to withstand ventilation better as the steady-state intensity and threshold ventilation both increase while the minimum intensity needed for sustainability decreases with increasing potential intensity. Hence, the same magnitude of vertical wind shear may have quite different effects in different thermodynamic environments, allowing a fairly strong TC to be maintained in a high potential intensity environment while dissipating another TC in a low potential intensity environment.

Normalizing the steady-state intensity by the potential intensity and the ventilation by the threshold ventilation for each respective thermodynamic environment collapses the framework into a single curve that is invariant across all thermodynamic states. It would be interesting to see if, observationally, nature also follows this law. The difficulty in doing this arises in estimating the actual ventilation with observations, as it would require high density time and space observations of radial flow and entropy at lower to middle levels in the inner core. A possible field experiment to assess these variables would involve a circular flight at midlevels just radially outside the eyewall with preferably more than one plane or combination of unmanned aerial vehicles using dropsondes to gather thermodynamic data and dual Doppler radar to assess the flow.

In the meantime, it may be possible to relate the ventilation to larger scale, more easily observed features such as the magnitude of the vertical wind shear and internal parameters related to the TC structure, such as done in Emanuel et al. (2004). The ventilation calculated over a larger domain from coarse gridded data, such as done in Marin et al. (2009) with the Global Forecast System model, may be sufficient for capturing some of the variance associated with ventilation induced intensity changes. Ideally, the ventilation should be calculated as close to the inner core as possible.

A sensible approach to carry out this calculation and to test the theoretical characteristics of ventilated TCs is to use numerical simulations of ventilated or sheared TCs. An axisymmetric TC model with parameterized eddy fluxes at midlevels would be an efficient way to assess the behavior and intensity of a ventilated TC over a wide array of ventilation values and thermodynamic environments. Moreover, it would be interesting to see if the gross properties of this formulation also carry over to 3D, high-resolution simulations of sheared TCs. In particular, the connection between ventilation and resulting downdrafts needs to be examined along with the energy and entropy budgets at different annuli, specifically around the eyewall and any widespread downdrafts.

Lastly, it has been noted that changes in vertical wind shear may be an important factor in future changes in TC activity (Vecchi and Soden, 2007b). With an increase in potential intensity, the same amount of ventilation does comparatively less. However, as elaborated upon in Emanuel et al. (2008), the entropy deficit between the boundary layer and midlevels should increase with global warming under the assumption of constant relative humidity. Since ventilation is a function of this entropy deficit, the ventilation should correspondingly increase, leading to an increase in the entropy eddy flux and downdraft convective available potential energy even in the event that eddy velocities are invariant with time (Nolan and Rappin, 2008). Whether this corresponds to a change in the normalized ventilation, which is the relevant quantity to consider, depends largely on how the combination of vertical wind shear, entropy deficit, and potential intensity evolve with climate change.

Chapter 3

A Ventilation Index for Tropical Cyclones: Climatology and Projections

3.1 Introduction

A number of environmental factors control tropical cyclogenesis and tropical cyclone (TC) intensity, contributing to the challenge of TC prediction. Among these environmental controls is the interaction of TCs with environmental vertical wind shear associated with upper tropospheric troughs (Hanley et al., 2001), midlevel jets such as that associated with the Saharan air layer (Dunion and Velden, 2004), and outflow from other TCs and monsoon depressions (Elsberry and Jeffries, 1996). Since environmental vertical wind shear is always present in varying amounts during the course of any TC's life, it is important to understand how wind shear affects TCs to improve intensity and genesis forecasts and to assess how TC statistics may change with climate.

3.1.1 Genesis and Intensity

Environmental vertical wind shear is generally thought to be detrimental to tropical cyclogenesis. Based on analysis of developing and nondeveloping systems in both the Northwest Pacific and North Atlantic, McBride and Zehr (1981) and Zehr (1992) concluded that the vertical wind shear must be close to zero near the system's center for genesis to occur. These empirical observations led to the development of regional and global genesis indices for the North Atlantic and globe in which the inclusion of vertical wind shear is necessary to produce skillful indices (Gray, 1979; DeMaria et al., 2001; Emanuel and Nolan, 2004). In addition to the case studies and statistics, a numerical modeling study by Nolan and Rappin (2008) found that vertical wind shear slows the development of an incipient vortex. In experiments where the shear is very strong, weak vortices do not develop at all.

Vertical wind shear may discourage genesis by ventilating the incipient disturbance with low-entropy or moist static energy air. Gray (1968) hypothesized that differential advection by the environmental flow removes the "condensation heat" from a vortex preventing it from deepening. Ventilation also occurs as drier air is advected into the disturbance, disrupting the formation of a deep, moist column which is postulated to be imperative for genesis (Emanuel, 1989; Bister and Emanuel, 1997). However, there are some studies that also hypothesize that modest shear, which induces synoptic-scale ascent on the downshear side of the system, may help organize convection in a developing system as well (Bracken and Bosart, 2000; Davis and Bosart, 2003; Musgrave et al., 2008).

Environmental vertical wind shear is also observed to be an impediment to TC intensification. Intensity changes at various time intervals are strongly and negatively correlated with the vertical wind shear (DeMaria, 1996; Gallina and Velden, 2002), and thus, vertical wind shear is one of the most important predictors in statistical-dynamical intensity models (DeMaria et al., 2005) and simplified dynamical intensity models (Emanuel et al., 2004; DeMaria, 2009). Zeng et al. (2007, 2008) found that most TCs in the Northwest Pacific and the North Atlantic achieve their maximum lifetime intensity when the vertical wind shear is less than 20 $\mathrm{m\,s^{-1}}$. A number of 3D numerical modeling studies of TCs in idealized shear environments also simulate decreases in intensity, but there are a number of hypotheses as to what causes the weakening, including outward eddy fluxes of entropy and potential vorticity that erode the TC from the top down (Frank and Ritchie, 2001), stabilization caused by midlevel warming (DeMaria, 1996), reversal of the secondary circulation on the upshear side allowing shear-induced entrainment of environmental air at upper levels (Wong and Chan, 2004), and eddy momentum fluxes that weaken the mean tangential winds (Wu and Braun, 2004).

Another hypothesis is that vertical wind shear may act to decrease the efficiency of the hurricane heat engine by exciting inner-core asymmetries that can then ventilate the TC inner core with low-entropy air at *midlevels* (Simpson and Riehl, 1958; Cram et al., 2007) or induce convective downdrafts by evaporative cooling, which are then swept inward by the radial inflow in the boundary layer (Powell, 1990; Riemer et al., 2010). In Ch. 2, a simple framework was developed to study ventilation's constraint on a TC's steady-state intensity. Ventilation weakens the TC because it siphons power away from the TC that would otherwise to be used to power the TC's winds against dissipation.

If ventilation is an important environmental control for both tropical cyclogenesis and TC intensity, then such a signal should be detectable in observations. The difficulty in performing such an analysis is that an accurate calculation of the ventilation requires high spatial and temporal observations of the TC's kinematic and thermodynamic structure, which is quite an onerous dataset to obtain given the limited resources available for in situ observations. Instead, numerical models have been used to study ventilation by investigating Lagrangian back trajectories of parcels (Cram et al., 2007) and budget analysis from gridded numerical weather prediction models (Marin et al., 2009). The latter study showed that TC intensification in the Global Forecast System model is correlated to the ventilation calculated over a $4^\circ \times 4^\circ$ area around the TC, implying that large scale environmental fields, rather than mesoscale features that aren't resolved by the model, capture at least a portion of ventilation's effects on TCs.

The lack of high resolution observations and high computational expense to run 3D TC simulations has limited ventilation studies to only a handful of cases. By using a result from Ch. 2, a ventilation index (VI) is proposed in section 3.2 that scales with the actual ventilation and can be easily calculated from reanalysis fields. In section 3.3, the VI is then used to assess the degree to which ventilation controls global TC genesis and intensity statistics.

3.1.2 Changes with Climate

Climate models indicate changes in the large-scale circulation along with warming of the SSTs and the thermal profile over the tropics. As such, robust discussion continues as to how global and regional TC statistics will respond to these large scale changes. Two main approaches have been used to study this problem: examining TC-like vortices in GCM output (Bengtsson et al., 1996; Oouchi et al., 2006; Yoshimura et al., 2006; Bengtsson et al., 2007; Zhao et al., 2009) and downscaling GCM fields using a higher resolution regional or TC model (Knutson and Tuleya, 2004; Emanuel et al., 2008; Knutson et al., 2008; Garner et al., 2009; Bender et al., 2010). A review of the studies performed to date indicates a global decrease in TC frequency by $6-34\%$ and an increase in intensity by $2-11\%$ by 2100 under the Intergovernmental Panel on Climate Change's A1B scenario (Knutson et al., 2010). However, there is large variability in individual TC basins and between different GCMs.

The shifts in TC frequency and intensity noted in GCMs are driven in part by changes in the distributions of environmental variables that control TCs. For example, Vecchi and Soden (2007b) and Garner et al. (2009) noted that the consensus of GCMs project an increase in vertical wind shear stretching from the Caribbean to the central North Atlantic. Such a pattern would result in more hostile conditions for TCs in these regions. However, most GCMs also project a small increase in potential intensity over most of the tropics, which would make thermodynamic conditions more favorable. Hence, there exist a multitude of competing factors and it is unclear which effects dominate.

One way to approach this problem is to regress different environmental factors on to the spatial and temporal distribution of tropical cyclogenesis events or accumulated statistics of TC intensity. For example, Emanuel and Nolan (2004) formulated a genesis potential index (GPI) with four environmental variables: the potential intensity (u_{PI}), low-level absolute vorticity (η), deep layer vertical wind shear (u_{shear}), and nondimensional entropy deficit (χ_m). The most recent form of the GPI is (Emanuel, 2010)

$$\mathrm{GPI} = \frac{|\eta|^3 \, \mathrm{MAX}(u_{PI} - 35, 0)^2}{\chi_m^{4/3}(u_{shear} + 25)^4}. \tag{3.1}$$

The nondimensional entropy deficit is defined as

$$\chi_m = \frac{s_m^* - s_m}{s_{SST}^* - s_b}, \tag{3.2}$$

where s_m is the midlevel entropy, s_b is the boundary layer entropy, and s^* is the saturation entropy. Evaluation of the GPI and similar seasonal genesis parameters in GCM simulations of the present climate reveals that they are capable of capturing the seasonality of TC activity along with the main regions of genesis (Camargo et al., 2007; Caron and Jones, 2008). A natural extension is to use the genesis indices as proxies for assessing possible long-term changes in genesis locations and numbers (McDonald et al., 2005). Similarly, Emanuel (2007) found that the low-level absolute vorticity, potential intensity, and vertical wind shear are all important predictors of the seasonal power dissipation index[1], and that subsequent changes in seasonal power dissipation in the future may strongly depend on these environmental factors.

Although the empirical indices work well for describing current TC climatology, there is always some subjectivity when it comes to choosing the statistical model and environmental variables to include. Increased understanding of physical pathways by which environmental factors affect genesis and intensity will lead to more refined variables or the consideration of new variables. One possible candidate for such a

---

[1] The seasonal power dissipation index is the cube of the maximum wind speed integrated over the lifetime of all TCs in a season.

refinement lies in the ventilation hypothesis and theoretical framework of Ch. 2. After a suitable normalization, the nondimensional ventilation is invariant across all thermodynamic states (potential intensities). Thus, the nondimensional ventilation serves as a more complete metric to explain projected changes in TC climatology versus simply looking at changes in vertical wind shear alone.

In section 3.4, the ventilation is calculated using output from GCMs over two periods: 1981-2000 and 2181-2200. First, the GCMs are compared to a reanalysis in order to assess how well they represent spatial patterns of ventilation from 1981-2000. Second, changes in the ventilation between the two twenty-year periods are calculated and implications for shifts in future TC climatology are discussed. Conclusions follow in section 3.5.

3.2 Ventilation Index

Under the assumptions of axisymmetry, steadiness, and slantwise neutrality, an expression for the ventilation-modified steady-state intensity is derived in Ch. 2. Upon nondimensionalizing the maximum wind speed (u_m) by the potential intensity and the ventilation ($\mathcal{V}$) by the ventilation threshold[2], the intensity equation takes the simple form

$$u^{\dagger 3} = u^{\dagger} - \frac{2}{3\sqrt{3}}\mathcal{V}^{\dagger}, \tag{3.3}$$

where $u^{\dagger}$ is the nondimensional maximum wind speed and $\mathcal{V}^{\dagger}$ is the nondimensional ventilation. The advantage of such a nondimensionalization is that the interaction between the potential intensity and vertical wind shear is effectively merged into a single term, making $\mathcal{V}^{\dagger}$ a convenient metric for assessing how future changes in environmental vertical wind shear may affect TC climatology.

The ventilation itself can be interpreted as the radial flux of entropy through a control volume above the boundary layer surrounding the eyewall of a TC, scaled by

---

[2] The ventilation threshold is defined to be the maximum ventilation at which a steady TC can exist.

a characteristic convective width. Assuming that the ventilation occurs at midlevels where the entropy deficit is the largest, the ventilation can be approximated as

$$\mathcal{V} \approx u'(s_m^* - s_m), \tag{3.4}$$

where u' is the radial velocity associated with inner-core asymmetries. Inner-core asymmetries, such as vortex Rossby waves, are excited by environmental vertical wind shear. This occurs as the vortex becomes tilted by differential advection, inducing a wavenumber one discrete mode of the vortex core (Schecter et al., 2002). Additionally, strong convection that preferentially forms in the downshear sector of the vortex will diabatically form low-wavenumber asymmetries (Reasor et al., 2000; Corbosiero et al., 2006). Reasor et al. (2004) derived an expression relating the environmental vertical wind shear forcing to the perturbation potential vorticity of vortex Rossby waves in a linearized primitive equation framework. Since vortex Rossby waves are quasi-balanced phenomena (Wang, 2002a), one should then be able to relate the flow associated with the perturbation PV in terms of the environmental vertical wind shear forcing as well, though such an exercise is left to future work. As a first step, this complication is avoided by assuming a linear relationship between u' and u_{shear}. Applying this to (3.4),

$$\mathcal{V} = k u_{shear}(s_m^* - s_m). \tag{3.5}$$

Next, the ventilation threshold (2.31) can be expressed as

$$\mathcal{V}_{thresh} = \frac{2}{3\sqrt{3}} u_{PI} C_k \left(s_{SST}^* - s_b\right), \tag{3.6}$$

where C_k is the enthalpy exchange coefficient. Dividing (3.5) by (3.6), results in an expression for the nondimensional ventilation:

$$\mathcal{V}^{\dagger} = \frac{k u_{shear}(s_m^* - s_m)}{\frac{2}{3\sqrt{3}} u_{PI} C_k \left(s_{SST}^* - s_b\right)}. \tag{3.7}$$

Based on (3.7), a ventilation index is defined:

$$\mathrm{VI} = \frac{u_{shear}\chi_m}{u_{PI}}, \tag{3.8}$$

where (3.2) has been substituted. The ventilation index increases with increasing environmental vertical wind shear and midlevel drying. However, increasing potential intensity will decrease the VI. In essence, it is the interaction of these three parameters that is important to TCs in this framework.

Comparing (3.1) and (3.8) reveals that there is a common link between the GPI and VI. Specifically, the GPI is proportional to some negative power of the VI, with the best fit using a power between -1 and -2. Hence, a portion of the variability of the spatial and temporal climatology of tropical cyclogenesis can be explained by ventilation. Since the GPI is a purely empirically derived quantity, some theoretical underpinning is garnered by the similarity to the VI.

However, it should also be remembered that the theoretical framework used to derive the VI is most applicable to mature TCs, so although ventilation is hypothesized to be important to all TCs in a broad sense, the exact processes by which low-entropy air is fluxed into the TC are likely quite different in the genesis versus mature stage. The high sensitivity of genesis to vertical wind shear, given by its quartic power in the GPI, may be due to the increased efficiency by which environmental air can intrude into the nascent disturbance due to lack of a large stagnation radius associated with a strong vortex (Dunkerton et al., 2009). Moreover, the terms that comprise the GPI can influence genesis in other ways besides ventilation. For example, vertical wind shear may discourage genesis by promoting linear versus circular convective organization (Robe and Emanuel, 2001; Dunkerton et al., 2009).

3.3 Ventilation Climatology

Daily ERA-40 reanalysis data (Uppala et al., 2005) from 1981-2000 is used to calculate the VI. The environmental vertical wind shear is defined to be the magnitude of the vector difference between the winds at 850 mb and 200 mb. For the nondimensional entropy deficit calculation, the reversible formulation of entropy (Emanuel (1994) pg.

120) is used, ignoring the liquid water heat capacity term. The 600 mb fields are used to calculate the (saturation) entropy at midlevels and the SST fields from the reanalysis are used to calculate s^*_{SST} assuming a surface pressure of 1015 mb. In lieu of using the 1000 mb ERA-40 fields for s_b, a relative humidity of 80% and a temperature that is 1 K less than the SST are assumed, which are typical values in Tropical Atmospheric Ocean buoy data. The motivation for doing this lies in the comparison with GCM data in the next section, in which the same approximation is made because the 1000 mb fields are not internally archived on disk. A comparison of s_b calculated using this approximation versus using the actual 1000 mb ERA-40 data reveals small differences equatorward of 25°. Lastly, the potential intensity is calculated using a reversible formulation, dissipative heating, and a ratio of enthalpy to drag coefficients of 0.9, which is the same configuration used in the Emanuel et al. (2008) study, hereafter E08.

It is important to note that TCs themselves have an influence on the VI as the TC's circulation increases the vertical wind shear around the storm, decreases the midlevel entropy deficit close to the center, and decreases the potential intensity. Since we wish to isolate the environment in which TCs are embedded, it is necessary to filter out any data contaminated by TCs. Therefore, any data within a $10° \times 10°$ box around a TC's best track position is removed[3].

After filtering TCs out of the data, the VI is calculated over the peak four months of each hemisphere's TC season (Jul.-Oct. for the Northern Hemisphere and Dec.-Mar. in the Southern Hemisphere) and averaged from 1981-2000, as shown in figure 3-1. Results are shown as $\log_{10}$(VI) in order to resolve detail in the tropics. In areas frequented by tropical cyclones in the tropics, the seasonally averaged VI is less than 0.1 and demarcates regions of high potential intensity, moist midlevels, and low vertical wind shear. The tongues of higher VI in the subtropics on the eastern side of the ocean basins are due to axes of higher vertical wind shear coinciding with dry air at midlevels despite fairly high potential intensity. Poleward of 30°N in the Northern

---

[3] The reanalysis TC positions can sometimes differ from the best track positions, but the area removed is large enough such that this should not be a problem.

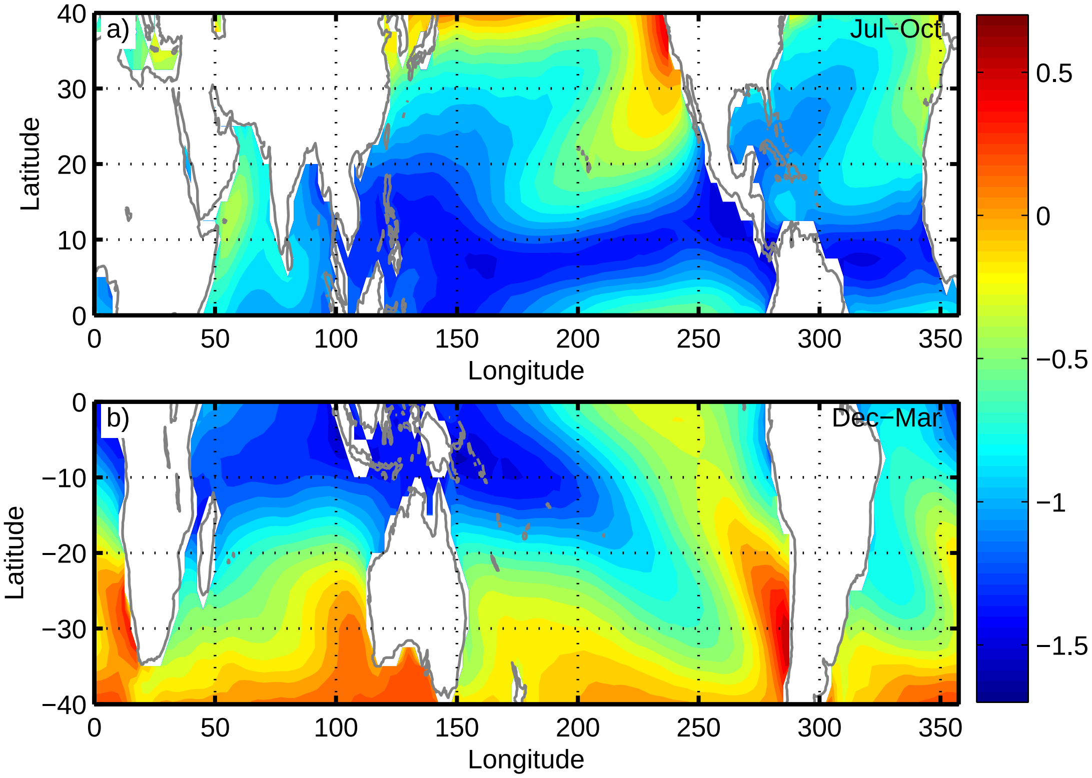

Figure 3-1: (a) Jul.-Oct. ventilation index for the Northern Hemisphere and (b) Dec.-Mar. ventilation index for the Southern Hemisphere averaged over 1981-2000. Results are shown as the $\log_{10}$(VI).

Hemisphere and 20°S in the Southern Hemisphere, the VI increases quickly due to increasing upper level westerlies and a sharp decrease in potential intensity.

3.3.1 Genesis

For individual tropical cyclogenesis events, the ventilation index on daily time scales is a more relevant metric to examine. Using daily ERA-40 data, two distributions of VI are constructed. The first distribution is called the “daily VI” and is defined to be the climatological distribution of daily VI accumulated over each point in the main genesis regions (MGR) of the tropics from 1981 to 2000. The MGR is defined in Tab. 3.1, and TC contaminated points have been eliminated using the same process outlined in the previous section. The second distribution is called the “genesis VI” and is defined to be the daily VI at genesis locations in the MGR one day before

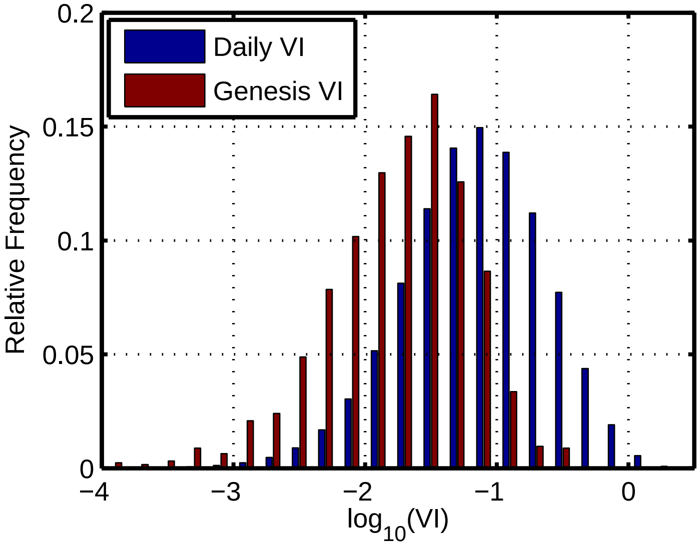

Figure 3-2: Normalized distribution of the climatological daily VI (blue bars) and genesis VI (red bars) in the main genesis regions (see Tab. 3.1 for definition). See text for precise definitions of each distribution. Daily VI data from 1981-2000 is used to construct both histograms.

genesis occurs. Thus, the genesis VI is simply a subset of the daily VI distribution isolated for tropical cyclogenesis events only. Both distributions are normalized and plotted in Fig. 3-2 on a logarithmic VI scale. Clearly, a significant portion of the genesis VI distribution, which has a median of 0.02, is comprised from the lower half of the daily VI distribution, which has a median of 0.07. Genesis is often associated with extremely low values of ventilation. Additionally, the genesis VI has a much sharper falloff to the right of its mode than the daily VI. Approximately 95% of all global tropical cyclogenesis events occur at a VI that is less than 0.1 with no events occurring above a VI of 0.4.

The 95th percentile for the genesis VI serves as a useful threshold for delineating global genesis regions. Figure 3-3 shows the percentage of days in each hemisphere's TC season when the daily VI is below the threshold value of 0.1. Approximately 98% of tropical cyclogenesis events occur at locations where more than 30% of the days in the TC season are below the VI threshold. A notable exception to this pattern is near the equator where there is a dearth of genesis events due to the low Coriolis

Table 3.1: TC basin and season definitions. All land areas within each basin are excluded.

Basin	Abbreviation	Season	Area
Main Genesis Regions	MGR	Jul.-Oct.	5-25N, 60-340E
		Dec.-Mar.	5-25S, 40-200E
North Atlantic	NATL	Jul.-Oct.	10-30N, 30-87.5W
Northeast Pacific	EPAC	Jul.-Oct.	10-25N, 95-140W
Northwest Pacific	WPAC	Jul.-Oct.	5-30N, 100-170E
North Indian	NIND	Jul.-Oct.	10-25N, 60-100E
Southern Hemisphere	SHEM	Dec.-Mar.	5-25S, 40-200E

parameter despite the high percentage of days with a VI below 0.1. There are no tropical cyclogenesis events at any location where less than 10% of the days are below the VI threshold, such as the area around Hawaii. In other words, tropical cyclogenesis is precluded from occurring where the VI is seasonally high, and a sufficiently low VI appears to be a necessary condition for tropical cyclogenesis.

3.3.2 Intensity

In addition to genesis, the *normalized* intensity, defined to be the TC's maximum, symmetric wind speed divided by the local potential intensity, is constrained by ventilation. The maximum, symmetric wind speed is estimated by subtracting 70% of the TC's translation speed from the best track maximum wind speed, with the 70% factor chosen to best correspond to observations (K. Emanuel, personal communication). To minimize the inclusion of hybrid storms or TCs undergoing extratropical transition, the analysis is confined to the MGR over the peak TC season. To minimize contamination by the TCs themselves, the VI is calculated by taking an average along a $10^\circ \times 10^\circ$ perimeter surrounding the TC center. Since the potential intensity is slowly varying, the potential intensity at a 3 day lead is used. Additionally, the potential intensity is then multiplied by 80% to account for the reduction of winds from the top of the boundary layer to 10 m in order to conform to the best track data before calculating the normalized intensity. The grayscale shading in Fig. 3-4

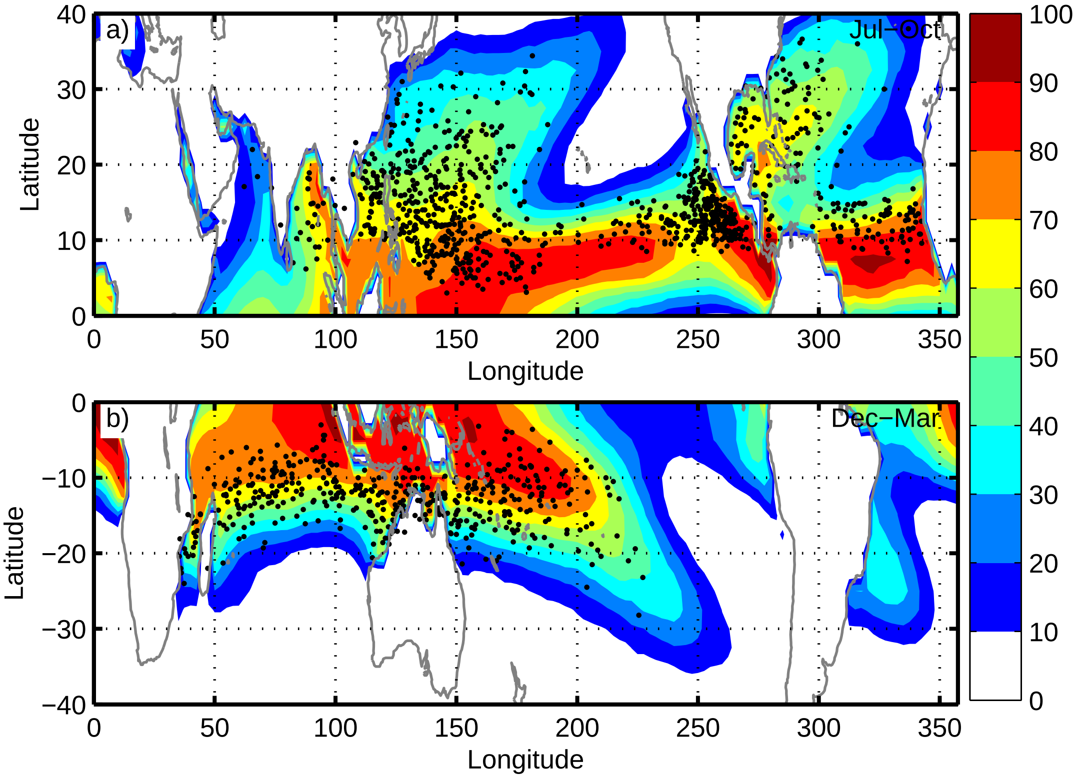

Figure 3-3: Percentage of days with a VI below 0.1 for (a) the Northern Hemisphere TC season and (b) the Southern Hemisphere TC season (shaded with contours every 10%). TC genesis points for the same period are denoted by black dots.

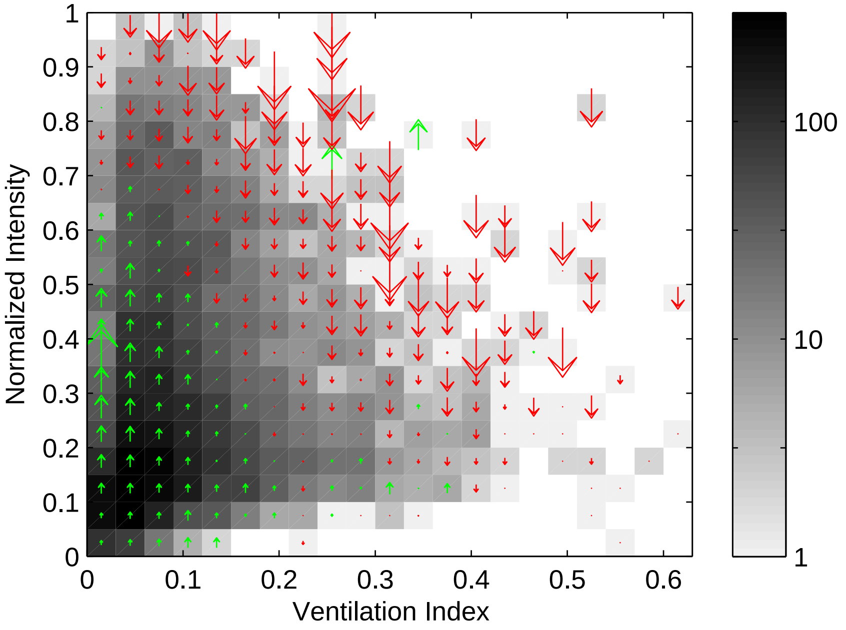

Figure 3-4: Grayscale shading indicates the number of daily TC observations in the MGR as a function of the VI and normalized intensity, i.e. the maximum, symmetric wind speed divided by the local potential intensity. Arrows signify the mean 24 hour normalized intensity change for TCs in each bin with green and red arrows indicating normalized strengthening and weakening, respectively. The maximum arrow length corresponds to a normalized intensity change of 0.4 over 24 hours.

shows the number of daily TC observations in the MGR as a function of both the VI and normalized intensity. Darker shading indicates a larger number of daily TC observations within each joint VI and normalized intensity bin. For low values of ventilation, TCs are observed with intensities from tropical depression strength to just above the potential intensity with the largest concentration of TC observations around 20% the potential intensity. As the VI increases, the overall number of TC observations decreases, but most starkly for high normalized intensities where there are only a few instances of TCs with normalized intensities above 0.6 for a VI greater than 0.4. This supports the conclusions from Ch. 2 and Zeng et al. (2008) that increasing ventilation or vertical wind shear acts to decrease the upper bound on a TC's intensity.

More intriguing is the relationship between the ventilation and normalized intensification, defined to be the change in normalized intensity over a given period of time. It is important to remember that the normalized intensification is usually different from the raw intensification as the potential intensity along the TC's track changes. For instance, one could have normalized strengthening despite a decrease in intensity if the potential intensity along the TC's track is dropping faster than the intensity. For the TCs in each joint bin in Fig. 3-4, the mean 24-hour normalized intensification is given by the arrows. Upward pointing green arrows indicate a mean normalized strengthening while downward pointing red arrows indicate a mean normalized weakening. The length of the arrow is reflective of the magnitude of the mean 24-hour normalized intensity change. Unless otherwise stated, all subsequent mentions of strengthening and weakening will be in the normalized sense.

There is a clear delineation between strengthening and weakening TCs in Fig. 3-4. TCs at low VIs and normalized intensities (lower left region of Fig. 3-4) tend to strengthen while TCs at high VIs and normalized intensities (upper right region of Fig. 3-4) tend to weaken. Additionally, there exists a fairly narrow region where the arrows converge, implying an equilibrium boundary. The boundary appears to be horizontal around a normalized intensity of 0.7 for the lowest few VI bins and then bends downward as the VI increases to 0.2. This behavior is qualitatively similar to the stable equilibrium solution of the theoretical framework, given by the solid curve in Fig. 2-5, where the steady-state intensity decreases more rapidly as the normalized ventilation increases. However, the observed equilibrium boundary does not extend all the way to the potential intensity. This may be due to uncertainties in the potential intensity, uncertainties in the best track intensities, and the fact that ventilation is not the only mechanism that controls intensity.

The greatest strengthening tends to occur at the lowest values of ventilation and normalized intensities around 0.4, while the greatest weakening tends to occur at high normalized intensities combined with intermediate to large VIs. The similarity with the stability analysis in Ch. 2, shown by the arrows in Fig. 2-5, is quite striking, particularly in the upper half of the figure. TCs far away from equilibrium tend to have a much larger normalized intensification. However, in the lower part of Fig.

3-4, the results are much less clear. There does not seem to be an unstable equilibrium separating strengthening and weakening TCs at low normalized intensities. One would expect the assumptions used in the theoretical framework would not apply as well to weaker storms due to the lack of axisymmetry and slantwise neutrality. The intensification of moderately sheared or ventilated TCs may be more dependent on mesoscale features such as transient bursts of convection (Nolan and Montgomery, 2002; Molinari et al., 2006). This would lead to much more variance in the intensification statistics, which may be responsible for the varied mean intensifications in bins with a VI between 0.2 and 0.4 and normalized intensities less than 0.4. Furthermore, it is also possible that there is a positive intensification bias at low normalized intensities in Fig. 3-4 because TCs that weaken below 15-20 knots are not included in the best track data and, therefore, are excluded from the sample.

While weakening can occur at all VIs, there appears to be an approximate upper bound on the VI for strengthening TCs. To assess where this upper bound may lie, the normalized VI distribution for strengthening TCs is shown in Fig. 3-5 by the green bars. Additionally, the distributions of the VI for weakening TCs and the daily VI in the MGR are added for comparison. As expected from the previous figure, the VI distribution for strengthening TCs is shifted to the left of the distribution for weakening TCs. The 95th percentile VI for strengthening TCs is 0.17 and corresponds closely to the transition zone in Fig. 3-4 where the mean normalized intensification becomes predominately negative. No TC is observed to strengthen when the VI is greater than 0.46, and the preponderance of those TCs that do strengthen in between a VI of 0.2 and 0.4 are at low normalized intensities, as mentioned previously.

There are several possibilities as to why there are few strengthening TCs observed at VI values below 0.01 whereas a significant portion of genesis events occur at VIs below 0.01. First, TCs tend to be steered away from genesis regions where the lowest VI is climatologically found, resulting in a predisposition to higher VIs. Second, some of the vertical wind shear associated with the TC circulation itself may be inflating the VI statistics, particularly if the storm is large and strong. A more sophisticated filter may be needed in order to filter out the TC's circulation to obtain a better

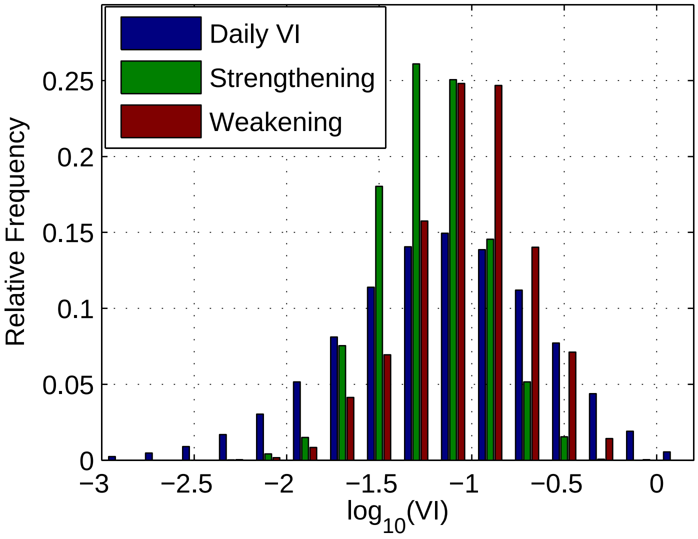

Figure 3-5: Normalized distribution of the logarithm of the VI for normalized strengthening and weakening TCs in the MGR from 1981-2000. The daily VI distribution from Fig. 3-2 is shown for comparison.

estimate of the environmental vertical wind shear and VI (see Appendix A for an example of such a filter). Finally, taking a $10° \times 10°$ perimeter average covers a rather large area and is likely canceling out some of the lowest values of VI around a TC, especially if the TC is embedded in an area with a large VI gradient. Despite these limitations, there is still a strong signal that appears in the statistics that supports a number of the results from Ch. 2, including a decrease in the maximum normalized intensity with increasing VI, the presence of a stable equilibrium boundary separating strengthening and weakening TCs, larger intensification rates for TCs located far from equilibrium, and an upper VI bound for strengthening TCs.

3.4 Ventilation in Global Climate Models

Monthly mean data from six GCMs are used to calculate the seasonal VI over two twenty year periods: 1981-2000 and 2181-2200. The six GCMs chosen are listed in Tab. 3.2 with their selection based on what was processed and archived internally on disk from the E08 study. Each variable in the VI is calculated in the same manner

Table 3.2: Models used in the VI comparison. Adapted from Emanuel et al. (2008)

Model	Institution
CNRM-CM3	Centre National de Recherches Meteorologiques, Meteo-France
CSIRO-Mk3.0	Australian Commonwealth Scientific and Research Organization
ECHAM5	Max Planck Institution
GFDL-CM2.0	NOAA Geophysical Fluid Dynamics Laboratory
MIROC3.2	CCSR/NIES/FRCGC, Japan
MRI-CGCM2.3.2a	Meteorological Research Institute Japan

as elaborated upon in the previous section. Additionally, it is assumed that

$$\overline{VI} \approx \frac{\overline{u_{shear}}\,\overline{\chi_m}}{\overline{u_{PI}}}, \tag{3.9}$$

where $\overline{(\ )}$ denotes a seasonal mean. This is tantamount to assuming the covariance between u_{shear} and χ_m along with the variance of u_{PI} are small. Comparing (3.9) to the full seasonal VI using ERA-40 data suggests that over the vast majority of the tropics, (3.9) is a good approximation.

3.4.1 1981-2000

The spatial pattern of the seasonal VI calculated from GCM data shows broad agreement in the tropics but larger variations in the subtropics. Like the reanalysis, the GCMs show very low seasonal VI in the primary tropical cyclogenesis regions. Moreover, there is a sharp increase in the VI as one moves toward the midlatitudes, with the largest VI consistently on the eastern side of ocean basins and the upwelling regions of the equatorial Pacific. The GCMs differ primarily in the extent and magnitude of the tongues of high VI that extend down through the subtropics on the eastern side of ocean basins. In the North Atlantic, for example, the CNRM has an extensive area of high VI extending down in to the main development region while ECHAM and GFDL models do not (not shown). Additionally, the magnitude of the local extrema of VI differ from model to model.

Compared to the reanalysis VI, the GCM VI has substantial errors, as shown in Fig. 3-6 for the Northern Hemisphere and Fig. 3-7 for the Southern Hemisphere. In the Northern Hemisphere, the bias is predominately positive in the CNRM, CSIRO, and MIROC, especially off the west coast of Africa and in the equatorial Pacific where the VI is more than three times that of the ERA-40's VI. The ECHAM, GFDL, and MRI show less extreme and more varied differences in the TC basins, but still show VI errors of upwards of ±50%. In the Southern Hemisphere, the CNRM, CSIRO, and MIROC have a predominately positive bias in the South Indian and the South Pacific Convergence Zone. On the other hand, the GFDL has a VI that is too low over almost all of the Southern Hemisphere, while the ECHAM and MRI are mixed.

One caveat to keep in mind are uncertainties in the reanalysis itself, particularly in data void regions. This is particularly true with the midlevel moisture or χ_m over the tropical oceans where there are very few observations to constrain the reanalysis. Therefore, it is impossible to equate the true VI to the reanalysis. Errors, especially small ones, should be viewed with caution. Nevertheless, there are clear differences amongst the GCMs themselves in their representation of the seasonal VI during the last twenty years of the 20th century.

Errors in the potential intensity, midlevel entropy deficit, and vertical wind shear all contribute to errors in the seasonal GCM VI, but there is a general latitudinal dependence on the partition of the error among the three variables. Poleward of 20°, potential intensity differences dominate the error. For instance, the large positive biases in the CNRM and CSIRO in the northern Pacific and in the northeastern Atlantic are caused by too sharp of a falloff of the potential intensity with latitude in these regions, which is likely a product of a cold bias in the SSTs (Yu et al., 2010). Equatorward of 20°, the GCMs estimate the potential intensity to a much better degree and the errors in the VI are caused more by disagreement in midlevel entropy deficit and vertical wind shear. Since these two variables are typically quite small in the tropics, small absolute differences between the GCMs and ERA-40 can translate to large percent errors in the VI.

Fig. 3-8 shows the distributions of the seasonal VI in the MGR for all six GCMs,

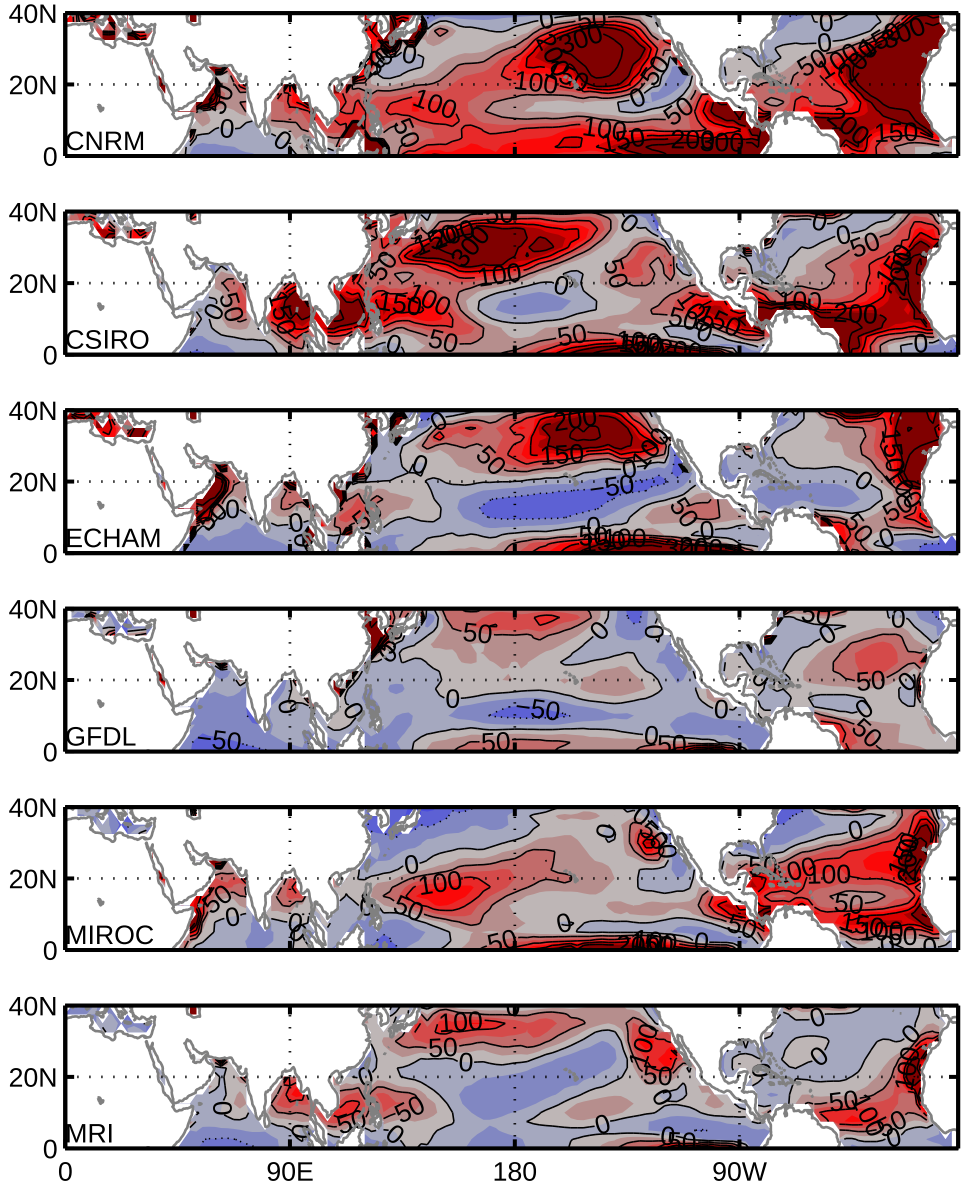

Figure 3-6: Percent difference between each GCM and ERA-40 seasonal VI in the Northern Hemisphere for 1981-2000. Blue (red) areas denote where the GCM has a seasonal VI that is lower (higher) than the ERA-40.

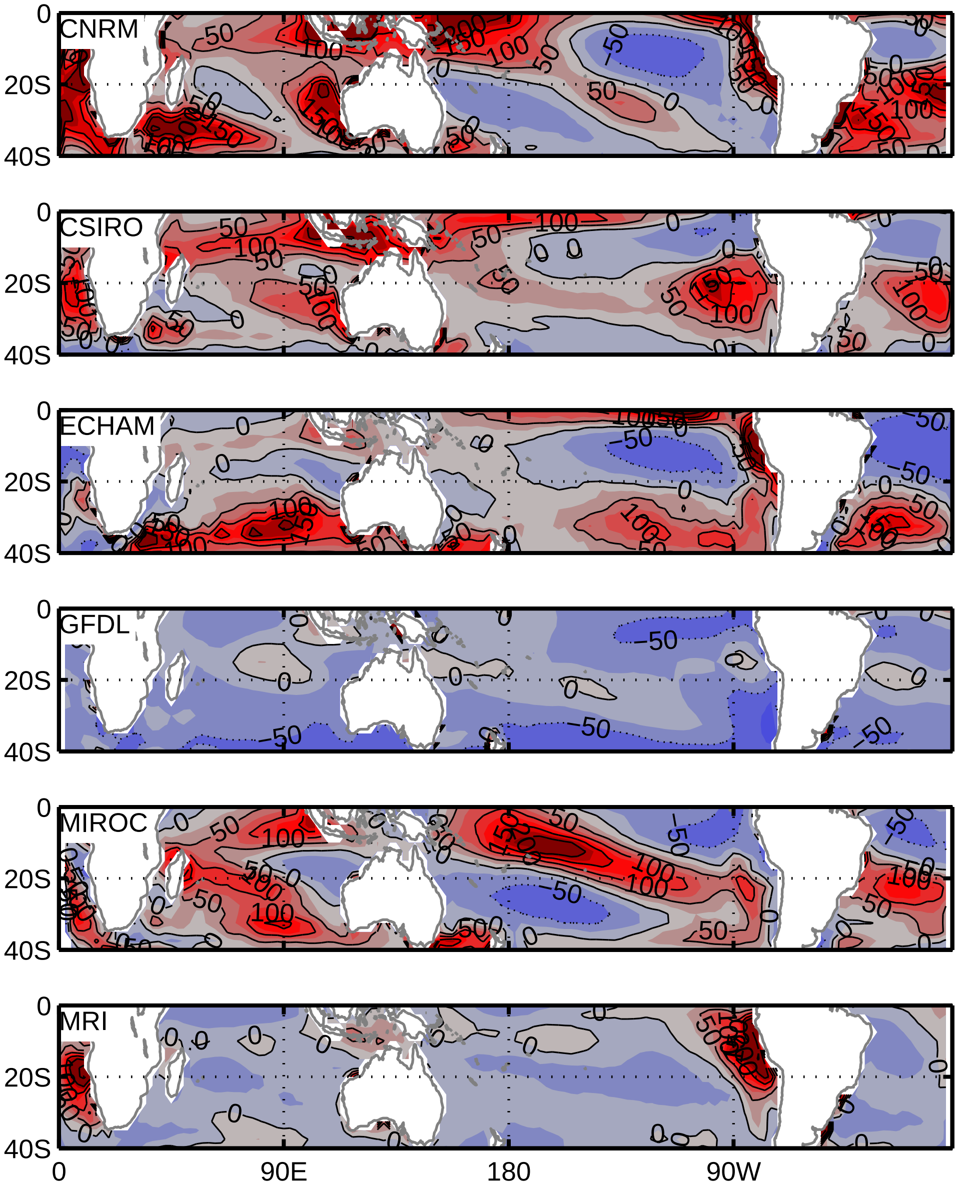

Figure 3-7: Similar to Fig. 3-6 but for the Southern Hemisphere.

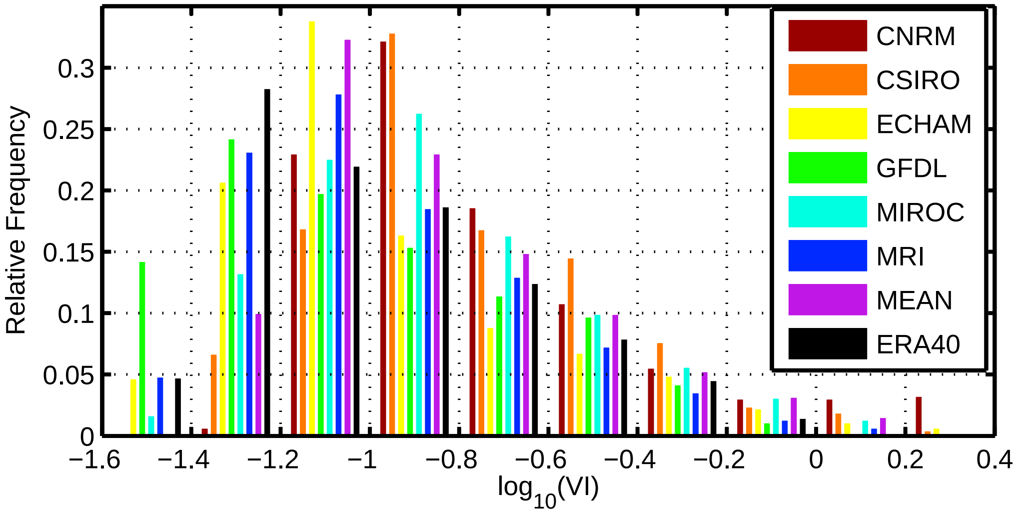

Figure 3-8: Normalized histograms of the seasonal VI in the MGR for all six GCMs, the mean of the GCMs, and the ERA-40 for 1981-2000.

the mean of the GCMs, and the ERA-40. As alluded to in the previous two figures, the CNRM and CSIRO both have positive biases with the mode at a value slightly greater than 0.1 compared to about 0.05 for the ERA-40. Additionally, the CNRM has a particularly long tail stretching to the largest VI bins. While the MIROC and consensus VI distributions do not appear to be as extreme as the former two models, they are also biased to larger values when compared to the ERA-40. On the flip side, the GFDL is biased too low, having about 14% of its grid points in the MGR in the lowest bin compared to under 5% in the ERA-40. While the ECHAM model shows little bias, it underestimates the spatial variance over the MGR. Overall, the MRI compares most favorably to the ERA-40.

Comparing the distributions of the daily VI in Fig. 3-5 to the seasonal VI in Fig. 3-8 for the ERA-40, it is apparent the seasonal VI lacks much of the left side of the distribution present in the daily VI. About 20-25% of the daily VI falls below $10^{-1.5}$ whereas almost none of the seasonal VI does. Hence, points where the VI stays very low do so for only for a limited duration. In contrast, there is no such drastic change between the daily and seasonal distributions at higher VI bins. The daily VI distributions for the GCMs should also have higher variances and may also show the same preference as the ERA-40 to extend to the left of the seasonal VI distribution; however, it is impossible to be sure without examining the daily VI distributions from each model, which is left as future work.

3.4.2 2181-2200

The sensitivity of both TC genesis and normalized intensity to the VI gives reason to believe that changes in the temporal and spatial distribution of the VI will lead to future changes in TC climatology. To ascertain possible changes, the seasonal VI is examined from 2181-2200 for the same six GCMs.

Figure 3-9 shows the percent change in seasonal (Jul.-Oct.) VI between 2181-2200 and 1981-2000 for the Northern Hemisphere. In each TC basin, the percent change is quite varied across the GCMs. In the North Atlantic, for instance, the CNRM and MIROC show increases in the western portion of the basin while the ECHAM and CSIRO show increases across the Caribbean and main development region. On the contrary, the GFDL shows decreases throughout most of the tropical North Atlantic while the MRI shows little change basin wide. In the Northeast Pacific, most of the models show an increase in the VI off the coast of Mexico, albeit to varying degrees. With the exception of the MIROC and MRI, the remainder of the GCMs show 0-30% increases in the seasonal VI in the Northwest Pacific from the Phillipines to just west of the dateline. In the North Indian, the results are just as varied, with half of the models showing upwards of a 40% decrease in the VI in the Arabian Sea and four of the models showing small increses in the Bay of Bengal.

Similarly, Fig. 3-10 shows the percent change in seasonal (Dec.-Mar.) VI between 2181-2200 and 1981-2000 for the Southern Hemisphere. Compared to the Northern Hemisphere, the changes are quite a bit stronger but still show regional variability across the GCMs. The most striking feature is a strong increase in the VI in portions of the South Pacific, particularly off the coast of South America. Additionally, the GCMs also decrease the ventilation over the equatorial Pacific, but since these regions of the Pacific are void of TCs in the current climate, changes in the VI here may be irrelevant unless there is a drastic change in the areas TCs populate, as is conjectured

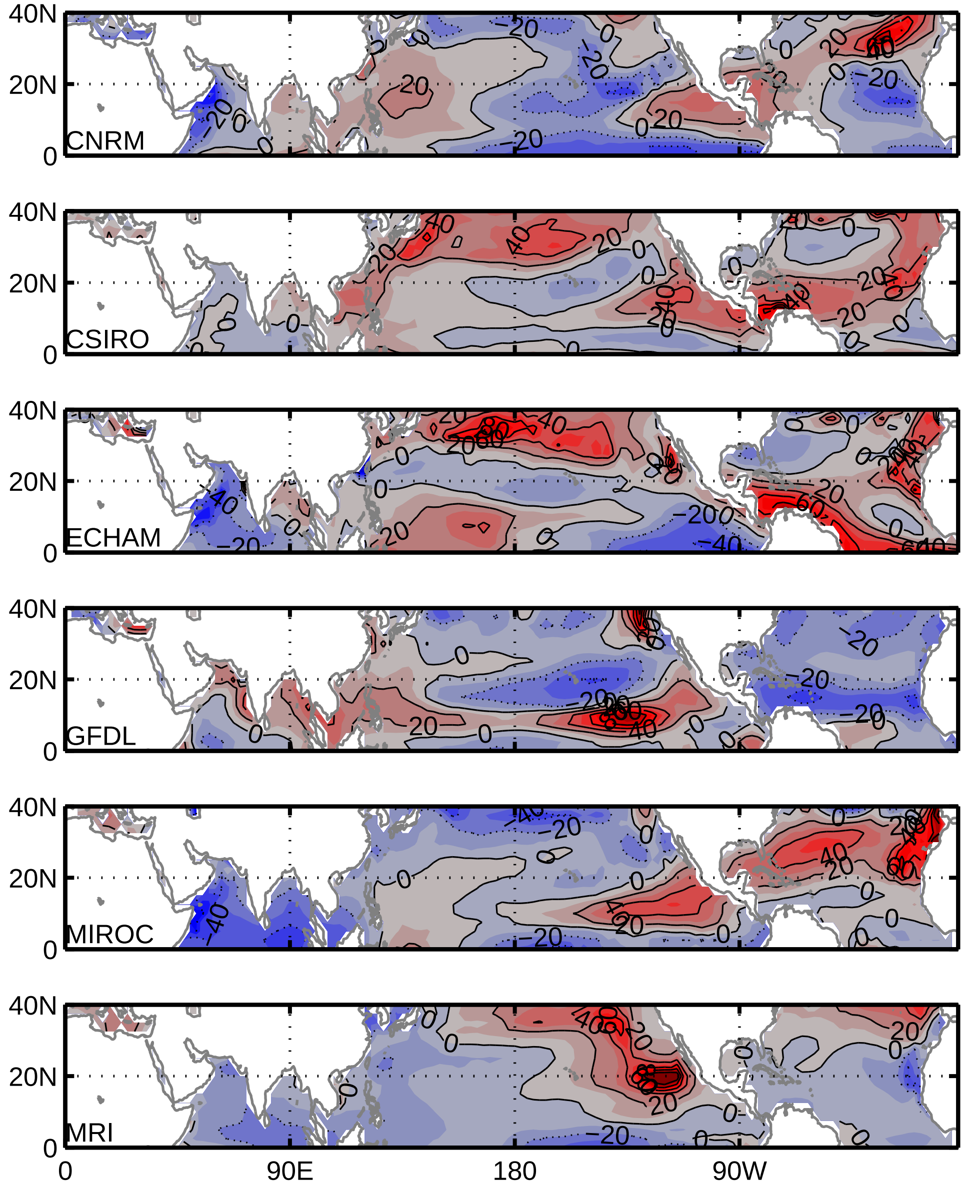

Figure 3-9: Percent change between the 2181-2200 and 1981-2000 Northern Hemisphere seasonal VI for all six GCMs.

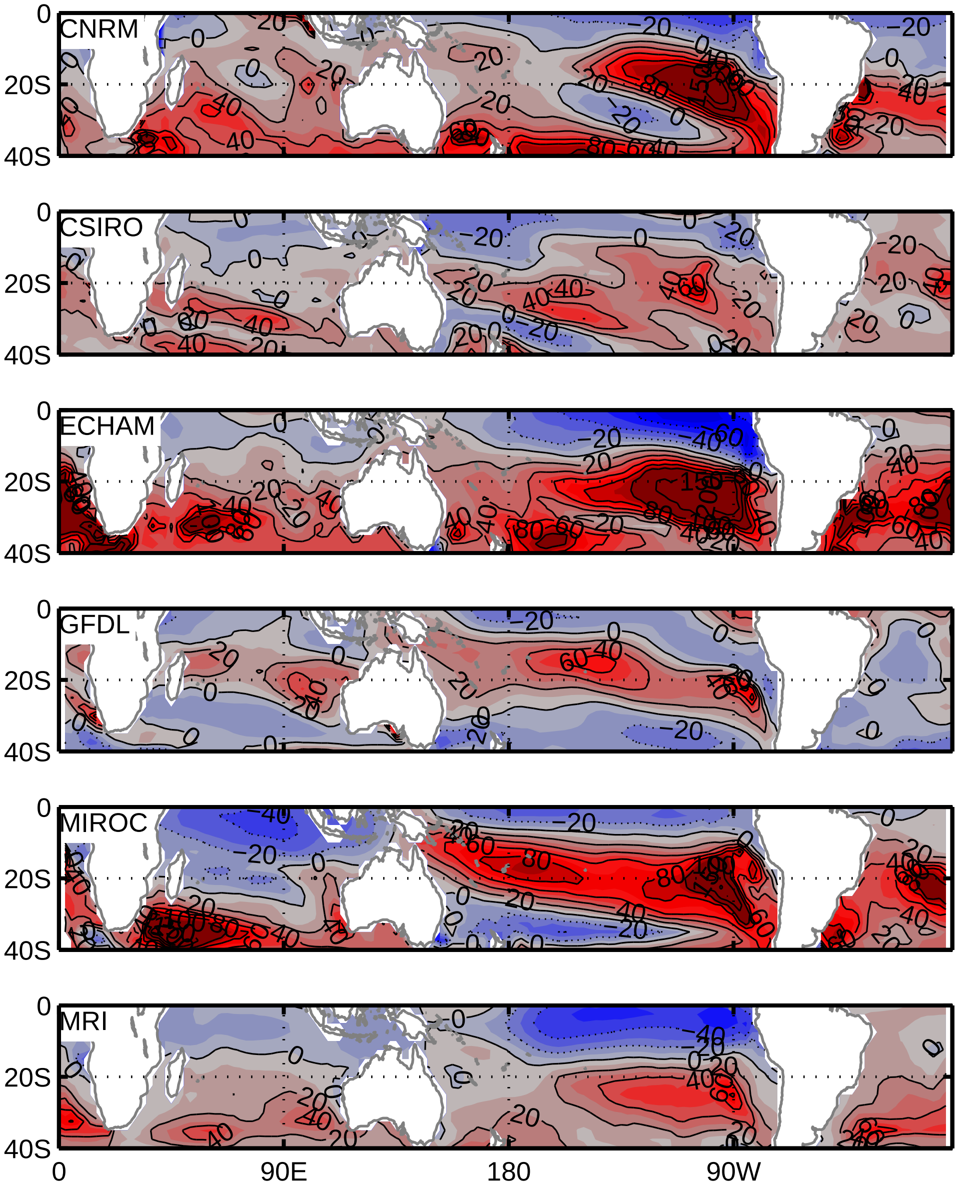

Figure 3-10: Similar to Fig. 3-9 but for the Southern Hemisphere.

to have occurred in the Pliocene (Fedorov et al., 2010). The changes in VI are weaker in regions frequented by TCs in today's climate. The models generally have a slight increase in the VI along 20°S with the exception of the MIROC, which shows considerable decreases in the South Indian and increases around Micronesia. Poleward of 20°S, the models generally increase the VI between 20-60%, and equatorward of 20°S, the models generally show little change.

Although there do appear to be pockets of agreement when one looks at the sign of the model changes, a better test is to rigorously assess the statistical significance of the seasonal VI change of the consensus of the six GCMs. An overwhelming portion of the oceans show no significant change in the VI at the 95% confidence level using a one sample t-test. It is possible that a more comprehensive examination of the the entire suite of CMIP3 model data would change this, but the six models chosen for in this study do not support the conclusion that there will be robust changes in the seasonal VI by the end of the 22nd century. However, the models individually show large changes, and if any realization is correct, there may be significant shifts in the VI climatology and thus the TC climatology in the future.

Despite the lack of statistical significance in changes in the GCM consensus of seasonal VI, it is still worthwhile to look at what is driving changes in the individual models. In a region from the Northeast Pacific stretching into the central North Atlantic, the VI increase is largely driven by an increase in vertical wind shear as noted in Vecchi and Soden (2007b). On the flip side, the GFDL has substantial decreases in vertical wind shear through most of the North Atlantic contributing to its decrease in the VI there. Elsewhere in both hemispheres, the spatial pattern of changes in vertical wind shear tend to be loosely correlated with changes in the seasonal VI, but clearly vertical wind shear does not provide the complete picture. For example, the GFDL model projects a small region in the Northeast Pacific to have a $> 60\%$ increase in seasonal VI despite a slight decrease in vertical wind shear in the same location. In other regions, especially the Southern Hemisphere, the percent change of the VI is quite a bit larger than would be implied by changes in vertical wind shear alone.

In addition to the vertical wind shear, the contribution of the nondimensional midlevel entropy deficit largely leads to an increase in the VI across much of the tropics. The reason for this, as explained in E08, is the fact that the numerator of (3.2) increases faster than the denominator with increasing tropospheric temperatures. Assuming constant relative humidity (Soden and Held, 2006), the numerator increases exponentially with increasing midtropospheric temperatures due to its dependence on the saturation mixing ratio. On the other hand, the denominator is proportional to surface evaporation and thus should not increase as quickly, due to energy balance constraints at the sea surface. Consequently, χ_m should increase nearly everywhere and this is supported by the six GCMs, which show an increase of 0-20% through most of the tropics except in central and eastern portions of the equatorial Pacific where there is a decrease. This decrease is associated with a weakening of the Walker circulation and a subsequent moistening in this region due to less large scale descent (Vecchi and Soden, 2007a). In the Southern Hemisphere, there is a poleward increase in χ_m, implying greater midlevel drying relative to the local air-sea disequilibrium. The GFDL model is a notable outlier, showing decreases in χ_m through most of the North Atlantic, near Hawaii, and in the Southern Hemisphere between 20°S and 40°S. However, the large VI increase in the GFDL over the Northeast Pacific mentioned previously can be mostly explained by a $> 50\%$ increase in χ_m. Where the vertical wind shear and midlevel entropy deficit both increase, such as in the MIROC in the Northeast Pacific and North Atlantic, the percent change in the VI can be quite a bit larger than the change in either component, making such regions potentially much more unfavorable to TCs in the seasonal mean.

Changes in potential intensity must also be taken into account since increases in the potential intensity will mitigate any increase in vertical wind shear and midlevel entropy deficit. The largest percent increases and decreases in potential intensity occur just off the western side of continents in both hemispheres, mostly between 20° and 40° due to the low present day potential intensities. However, these are regions rarely, if at all, visited by TCs and the seasonal VI would likely still be too large to allow anything but an isolated TC to enter these regions. Elsewhere in the tropics, the potential intensity increases modestly by about 0-10%. An exception to this is in the Arabian Sea where the models that decrease the VI by up to 40% show an increase in the potential intensity by up to the same percentage. On the flip side, the sharp increase in the VI in the MRI southwest of Baja California in the Northeast Pacific is due to a decrease of up to 40% in the potential intensity there. Curiously, there is also a large and broad decrease in potential intensity south of 20°S in the CNRM and ECHAM, which dominates the spatial structure of VI changes in the Southern Hemisphere between 20°S and 40°S. This, coupled with a broad increase in χ_m, is largely responsible for the large increase in the ventilation over the same area. Since vertical wind shear is already climatologically high in this region, one might speculate that the TC activity will be confined further equatorward in the Southern Hemisphere if these even more hostile conditions come to fruition.

Figure 3-11 shows the distributions of seasonal VI for 1981-2000 and 2181-2200 in the MGR. Five of the models shift the median of the seasonal VI distributions to larger values, while the MRI is the only hold out with a decrease. An increase in the median of the seasonal VI over the MGR implies that conditions that are most conducive to tropical cyclogenesis or normalized intensification would be observed a smaller percentage of the time and/or over a smaller region than what exists in today's climate. This would imply a global decrease in tropical cyclogenesis events over the peak seasons in each hemisphere, since genesis appears especially sensitive to the VI. An increase in the VI would also shift more TCs to the right in Fig. 3-5, making conditions less conducive for TCs to strengthen on average. On the other hand, the MRI would imply the opposite given that more locations will experience a lower seasonal VI and more hospitable conditions for tropical cyclogenesis and strengthening.

A summary of the change in the seasonal VI and the three components that comprise it for individual TC basins (listed in Tab. 3.1) is shown in Fig. 3-12. The percent change in the median over each basin is shown instead of the mean because it is less sensitive to outliers that disproportionately influence changes in the mean. Regionally, there is quite a bit of spread, as expected from previous figures. In the

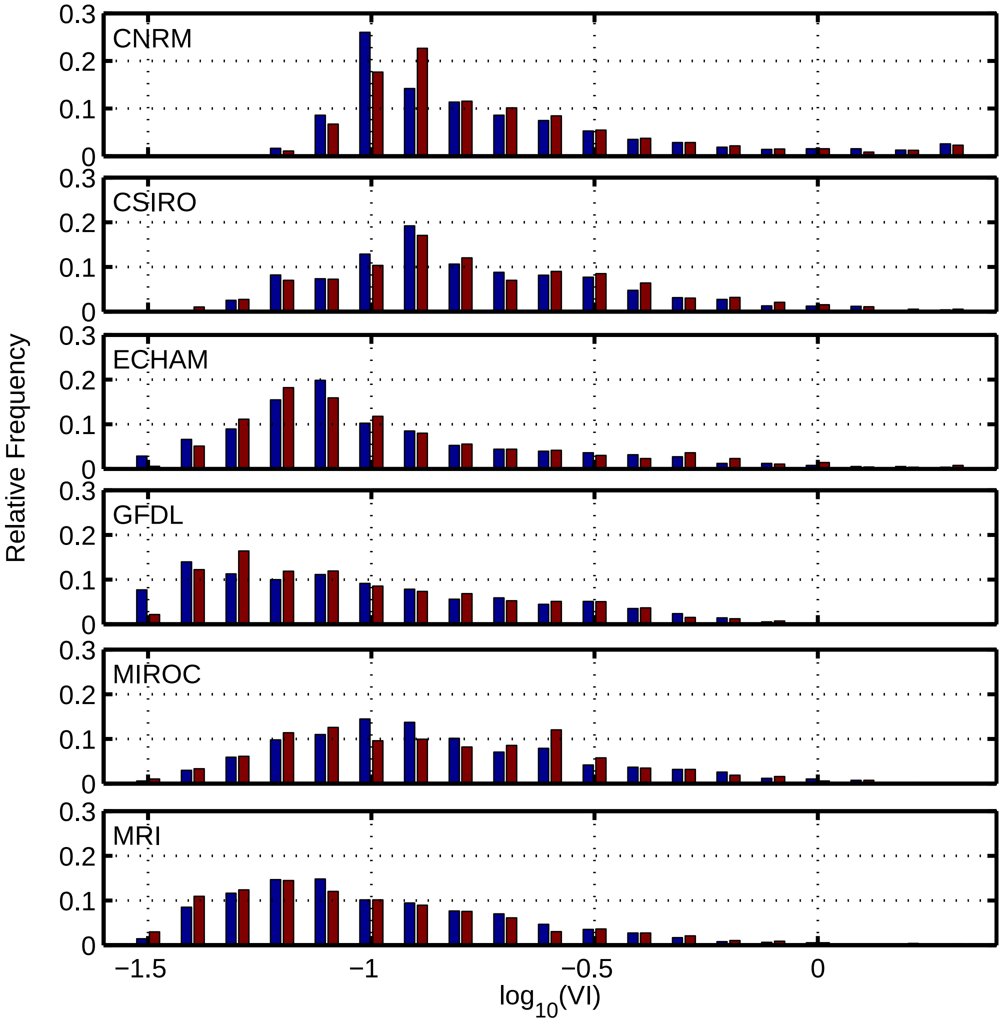

Figure 3-11: Normalized histograms of the seasonal VI over the MGR for all six GCMs for 1981-2000 (blue bars) and 2181-2200 (red bars).

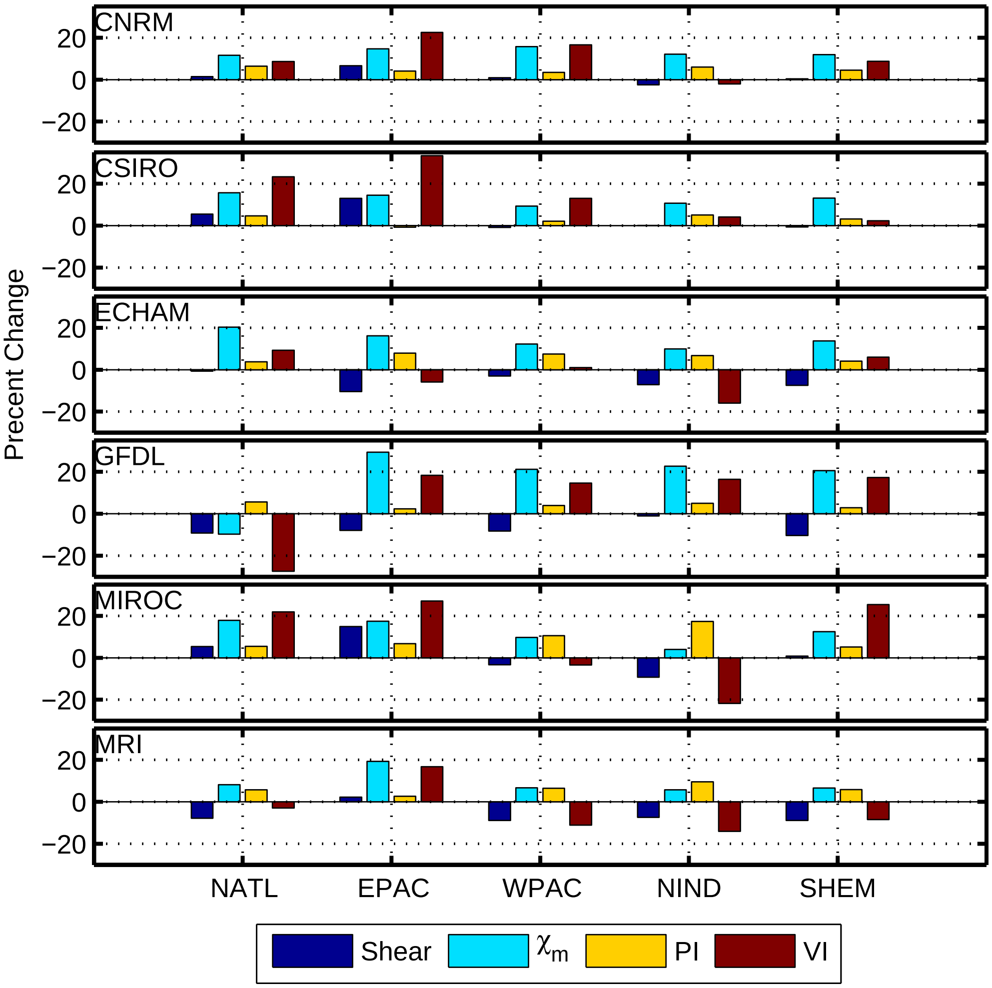

Figure 3-12: Percent change in the median of the seasonal vertical wind shear, nondimensional midlevel entropy deficit, potential intensity, and VI from 1981-2000 to 2181-2200 for each of the main TC basins listed in Tab. 3.1.

North Atlantic, the percent change in seasonal VI varies from approximately −30% in the GFDL to a little over 20% in the CSIRO. In the Northeast Pacific, the ECHAM shows slight decreases in the median VI while the remainder of the models show increases from 15% – 40%. A similar medley of changes is seen in the remainder of the basins. In fact, there is not a single basin where all six models even agree on the sign of the change in the median of the seasonal VI!

The change in basin VI in each model is not dominated by any one of its components. The largest changes in the seasonal VI clearly occur where the change in vertical wind shear and χ_m are the same sign and the change in potential intensity is the opposite sign, such as the Northeast Pacific in the CSIRO and the North Atlantic in the GFDL. Also noteworthy is the near universal agreement that χ_m will increase in each basin, with the exception of the GFDL in the North Atlantic. There is also near unanimity that the potential intensity increases by a small amount in every TC basin, which acts to decrease the VI. Given that the percent increase in χ_m tends to be larger than the percent increase in the potential intensity, changes in χ_m have more influence on changes in basin VI. In some cases, the increase in χ_m causes the VI to increase despite a decrease in the vertical wind shear such as in the GFDL for every basin except the North Atlantic. Thus, once again it is emphasized that solely looking at changes in vertical wind shear is an imperfect metric for understanding changes in ventilation and potential TC activity.

3.4.3 Comparison with Emanuel et al. (2008) (E08)

A comparison of the percent changes in seasonal VI with the change in genesis density in E08's Fig. 9 reveals quite a few similarities. In general, where the VI increases, the genesis density decreases and vice versa. The decrease in genesis density is most pronounced in the Southern Hemisphere, especially in the GFDL and MIROC, where the VI is projected to increase by a significant percentage. As noted in E08, the regional variability of the genesis density amongst the models is quite large, which is expected because of the variability of VI in the GCMs.

Is is harder to discern whether changes in intensity are correlated with changes in the VI in each TC basin. There are plenty of examples of basins and models where the mean intensity[4] or power dissipation in E08's Fig. 8 increases, and yet the VI also increases. However, the appropriate variable to consider in this framework is the normalized intensity. The sign of the change in the normalized intensity depends on whether the potential intensity change outpaces the mean intensity change. Nonetheless, the largest increases in basin-mean intensity in E08 tend to be associated with decreases in the VI, such as in the North Atlantic in the GFDL, the Northwest Pacific

---

[4] The mean intensity in E08 is defined as the cube of the maximum wind speed integrated over all synthetic TC tracks divided by the number of TCs and their duration.

in the MRI, and the North Indian in the MIROC. One complication is that the VI may be going opposite ways in different parts of the basin, such as is seen in the Arabian Sea and Bay of Bengal in some of the GCMs, and therefore the intrabasin distribution of TC activity becomes an important factor to consider.

3.5 Conclusions

Vertical wind shear is generally thought to be unfavorable for both tropical cyclogenesis and TC intensification. One hypothesized way vertical wind shear affects TCs is by ventilating the TC with low-entropy air from the environment. Based on an idealized ventilation framework, a ventilation index is derived that scales with the nondimensional ventilation. Advantages of the VI are that it can be calculated from large scale gridded fields and that it scales with the nondimensional ventilation from Ch. 2, which absorbs the dependence on the background thermodynamic state. Both of these qualities make it useful for evaluating whether ventilation plays a detectable role in current TC climatology and for evaluating possible changes in TC statistics in different climates.

The seasonal distribution of tropical cyclogenesis is confined to regions of low seasonal VI. Furthermore, the VI is shown to explain a portion of the variance in empirical seasonal genesis indices such as the GPI. On shorter timescales, it is shown that tropical cyclogenesis is most favored when the VI is in the lower half of the climatological daily VI distribution in the global main genesis regions. Approximately 30% of TCs form when the daily VI is below 0.01, and 95% of TCs form when the daily VI is below 0.1.

Ventilation also constrains a TC's normalized intensity. The maximum normalized intensity for TCs in the MGR decreases with ventilation. Moreover, there appears to be an equilibrium boundary in VI and normalized intensity space to which TCs tend to strengthen or weaken toward, especially for TCs with normalized intensities greater than 0.4. Away from the equilibrium boundary, TCs at small ventilation (< 0.1) and intermediate normalized intensities (0.3-0.5) tend to have the greatest strengthening, while TCs at higher ventilation (> 0.2) and high normalized intensities (> 0.5) tend to have the greatest weakening. Lastly, approximately 95% of strengthening TCs have a VI less than 0.17. All of these results support the findings of Ch. 2, with the exception of weak storms at moderate ventilation, which show a more varied response. This may be due to transient, asymmetric features playing a greater role in determining the intensification in these type of systems.

Next, the VI is examined in GCM output from 1981-2000 to assess the ability of GCMs to reproduce the current climatological seasonal VI. While all the GCMs show the same broad pattern of low seasonal VI in the MGR as the ERA-40, there are substantial relative differences between the GCMs and ERA-40 VI. The causes of these differences vary from model to model but generally can be pinpointed to potential intensity errors poleward of 20° and nondimensional midlevel entropy deficit and vertical wind shear errors equatorward of 20°.

Projected changes in the seasonal VI due to climate change are examined in GCM output from 2181-2200. Regionally, there is quite a bit of variability among the GCM projections. The large variability causes the consensus of the six GCMs to predominately lack any statistically significant changes in regions that are frequented by TCs in today's climate, and one cannot conclude with any high confidence that the seasonal VI will change at any given location. However, individual models do show large VI changes and any single realization indicates potential regional shifts in preferred locations of tropical cyclogenesis and changes in TC intensity statistics. It is possible that some of the variability in the GCMs may be caused by natural variability, such as the Atlantic Multidecadal Mode (Delworth and Mann, 2000; Goldenberg et al., 2001). To see whether natural variability is influencing the GCMs, one would need to examine the seasonal VI over a longer period of time or over different twenty year intervals.

It is evident that vertical wind shear changes only play a portion of the role in ventilation changes. The nondimensional midlevel entropy deficit and potential intensity increase nearly everywhere in the tropics. The former acts to augment increases in vertical wind shear while the latter serves to mitigate the effects of vertical wind shear. Since the GCMs tend to show χ_m increasing faster than the potential intensity in most of the TC basins, the former alone will increase the ventilation even in the absence of any changes in vertical wind shear.

A range of of GCM and downscaling experiments shows global TC frequency either decreasing or remaining approximately the same by 2100 under the A1B scenario (Knutson et al., 2010). Since tropical cyclogenesis appears to be quite sensitive to the VI in today's climate, the VI is a good candidate for an environmental factor by itself or as part of a genesis index that can be used to attribute changes in TC frequency in GCMs. A decrease in global TC frequency is consistent with an upward shift in the distribution of the seasonal VI in all but one of the GCMs examined in this study. However, the large variability in VI changes among different TC basins implies the possibility of larger regional shifts, albeit with a much higher degree of uncertainty.

Likewise, the VI can be used to infer potential changes in the normalized intensity. However, TC climate change studies have mostly looked at changes in intensity or integrated measures of it. Since the GCMs project on average small increases in both intensity and potential intensity, it is hard to say without further analysis whether the GCMs show a change in the distribution of normalized intensities. Increasing seasonal ventilation would tend to cause the upper percentiles of the normalized intensity distribution to decrease, but wouldn't necessary preclude a higher mean raw intensity upon redimensionalizing since the entire distribution would be "stretched" out to a higher upper limit. As is the case with genesis, larger but uncertain regional changes in the VI suggest the possibility of more complex changes in the normalized intensity distribution in individual TC basins.

In addition to the seasonal VI, the change in the daily VI distribution from the GCMs should be examined, since changes in the variance of the distribution are at least as, if not more, important for TC genesis and intensity. This is especially true for genesis, given the threshold-like behavior that occurs as the daily VI increases to around 0.1. Any curtailing of the extent of the left side of the distribution below a VI of 0.1 may be especially detrimental to TC genesis and would reduce the probability that any given TC encounters conditions favorable for rapid normalized strengthening.

Chapter 4

Ventilation in an Axisymmetric Tropical Cyclone Model

4.1 Introduction

Tropical cyclones (TCs) are often approximated as axisymmetric phenomena to first order, but asymmetric features are undoubtedly a fundamental part of a TC's structure. Although there is good understanding the types of waves a TC supports, there is high uncertainty how these convectively coupled waves interact dynamically and thermodynamically with the mean vortex to affect the intensity. This part of my thesis seeks to understand a possible thermodynamic pathway by which asymmetries can modulate a TC's intensity.

A particular subset of waves, called vortex Rossby waves, comprise much of the low-wavenumber power in the inner core of the TC, particularly along the sharp radial gradient of potential vorticity just outside the radius of maximum winds. Vortex Rossby waves are hypothesized to be excited by internal mechanisms, such as the breakdown of a high potential vorticity ring (Schubert et al., 1999), and external mechanisms, such as environmental vertical wind shear (Reasor et al., 2000; Corbosiero et al., 2006). Differential advection by environmental vertical wind shear tilts the high potential vorticity column of the vortex inducing a "quasi-mode," which is a wavenumber one discrete mode describing the precession of the vortex (Reasor and Montgomery, 2001; Schecter et al., 2002; Reasor et al., 2004). Another source of excitation of vortex Rossby waves is asymmetric diabatic heating (Wang, 2002a), which is prominent in sheared TCs due to large convective asymmetries.

The effect of vortex Rossby waves on the intensity of TCs has mainly been studied through eddy momentum fluxes. Montgomery and Kallenbach (1997) first proposed that sheared vortex Rossby waves could accelerate the mean tangential winds of the TC. This finding was confirmed in a barotropic and baroclinic models for initially prescribed positive potential vorticity perturbations near the radius of maximum wind. These perturbations project onto sheared vortex Rossby waves, and their axisymmetrization causes the TC's winds to be accelerated inside the critical radius and decelerated further outward (Moller and Montgomery, 1999, 2000). In a nonhydrostatic mesoscale model, Eliassen-Palm flux diagnostics for a strengthening TC also show that eddy momentum and heat fluxes accelerate and contract the maximum tangential winds in the lower troposphere (Chen et al., 2003). On the contrary, growing discrete vortex Rossby wave modes, such as induced by barotropic instability, will extract energy from the mean state weakening the intensity (Kwon and Frank, 2005).

In addition to eddy momentum fluxes, eddies affect the entropy distribution and budget of the inner core. Peng et al. (1999) proposed that large wavenumber one asymmetries in the inner core can lead to the maximum moisture convergence being out of phase with the maximum surface flux, limiting intensification. Riemer et al. (2010) proposed that a standing wavenumber one vortex Rossby wave, caused by the tilt of outer portions of the vortex, forces vertical velocity and convective asymmetries. These asymmetries, particularly convective downdrafts, lead to a pronounced wavenumber one asymmetry in the entropy field.

Eddy entropy fluxes are important to consider because fluxes of low-entropy air into the TC's inner core can frustrate the heat engine and constrain the intensity (Simpson and Riehl, 1958). In Ch. 2, an axisymmetric, steady-state, and slantwise neutral framework is used to show that ventilation acts to decrease the mechanical energy generation available to drive the TC's winds. The main findings from Ch. 2 are: (1) increasing ventilation nonlinearly reduces the steady-state intensity below the potential intensity, (2) ventilation acts to increase the initial intensity needed for a TC to intensify, and (3) there is a ventilation threshold beyond which only weakening TCs are possible. Additionally, ventilation acts to increase the outflow temperature, or equivalently, decrease the thermodynamic efficiency.

A handful of 3D, moist numerical simulations have looked at ventilation in sheared TCs, but the studies vary with the proposed "flavor" of the ventilation pathway. The first flavor is the upper-level pathway. Frank and Ritchie (2001) and Kwon and Frank (2008) found that vertical wind shear acts to excite asymmetries through both barotropic and baroclinic processes in the upper part of the vortex. They hypothesized that the asymmetries descend with time, weakening the vortex from the top down. Weakening occurs as the upper-level warm core is eroded by positive eddy heat fluxes resulting in a hydrostatic increase in central minimum pressure. The second flavor is the midlevel pathway. Lagrangian back trajectory analysis of a sheared TC reveals that the eyewall is ventilated by parcels originating at midlevels. The midlevel ventilation results in a reduction of the eyewall equivalent potential temperature by about 1 K (Cram et al., 2007). The third flavor is the low-level pathway. Downdrafts from convection outside the eyewall may provide a way for low-entropy air to access the inner-core of the TC via the secondary circulation (Riemer et al., 2010), albeit boundary layer processes may modify the low-entropy air substantially by the time it reaches the eyewall (Powell, 1990). It is unclear which pathways are most detrimental to the TC. Eddy kinetic energy may be higher at upper-levels, but the entropy gradient is weak and eddy motions may lie along isentropes. On the contrary, eddy kinetic energy may not be as large at midlevels, but the entropy gradient is much more pronounced.

To address this conundrum, the sensitivity of TC intensity to the amplitude and location of the ventilation and to downdraft activity is assessed in an axisymmetric, nonhydrostatic, and finite volume TC model, which is described in section 4.2. After a control run is presented in section 4.3, a suite of experiments and intensity diagnostics are used to assess the sensitivity of TC intensity to spatially fixed ventilation in section 4.4. Spatially varying ventilation is then used to evaluate the findings of Ch. 2 in section 4.5. Conclusions follow in section 4.6.

4.2 Model Description

The initial motivation for the design of the current TC model arises from diagnosing a large residual in the mass budget of the Rotunno and Emanuel (1987), hereafter RE87, model. This problem is detailed in Appendix C. Since entropy and energy budgets are powerful diagnostic tools for analyzing TCs, it is ideal that the model be designed such that mass, energy, and entropy are rigorously conserved in the absence of sources or sinks. Another aim is to retain the simple nature of the RE87 model, which makes it useful for studying axisymmetric TC processes.

4.2.1 Governing Equations

Like the RE87 model, the current model is phrased in cylindrical coordinates (r,ϕ,z) on an f-plane, is nonhydrostatic, compressible, and axisymmetric. The prognostic variables chosen in this model are the radial, tangential, and vertical momentum per unit volume ($U = \rho_d u$, $V = \rho_d v$, $W = \rho_d w$); the psuedoadiabatic entropy per unit volume ($S_p = \rho_d s_p$); and the densities of dry air, water vapor, and liquid water (ρ_d, $\rho_v = \rho_d q_v$, $\rho_l = \rho_d q_l$), where q_v is the water vapor mixing ratio and q_l is the liquid water mixing ratio. The governing equations for these variables in flux form are:

$$\frac{\partial U}{\partial t} = -\nabla\cdot(\mathbf{u}U) + \rho_d\left[v\left(f+\frac{v}{r}\right) - c_{pd}\theta_v\frac{\partial \Pi}{\partial r}\right] + D_U, \tag{4.1}$$

$$\frac{\partial V}{\partial t} = -\nabla\cdot(\mathbf{u}V) + \rho_d\left[-u\left(f+\frac{v}{r}\right)\right] + D_V, \tag{4.2}$$

$$\frac{\partial W}{\partial t} = -\nabla\cdot(\mathbf{u}W) + \rho_d\left[-g(1+q_l) - c_{pd}\theta_v\frac{\partial \Pi}{\partial z}\right] + D_W, \tag{4.3}$$

$$\frac{\partial S_p}{\partial t} = -\nabla\cdot(\mathbf{u}S_p) + \rho_d\left[\frac{c_{pd}}{\theta}\left(R+\mathcal{H}\right)\right] + D_{S_p}, \tag{4.4}$$

$$\frac{\partial \rho_d}{\partial t} = -\nabla\cdot(\mathbf{u}\rho_d), \tag{4.5}$$

$$\frac{\partial \rho_v}{\partial t} = -\nabla\cdot(\mathbf{u}\rho_v) - \rho_d M_{q_l} + D_{\rho_v}, \tag{4.6}$$

$$\frac{\partial \rho_l}{\partial t} = -\nabla\cdot(\mathbf{u}\rho_l) - \frac{\partial}{\partial z}\left(v_T\rho_l\right) + \rho_d M_{q_l} + D_{\rho_l}. \tag{4.7}$$

The remaining variables are the Coriolis parameter (f), gravitational acceleration (g), specific heat of dry air at constant pressure (c_{pd}), Exner function (Π), potential temperature (θ), virtual potential temperature (θ_v), and terminal velocity of raindrops (v_T). D, R, $\mathcal{H}$, and M refer to turbulent, radiative, dissipative heating, and microphysics terms, respectively.

The virtual potential temperature is defined as

$$\theta_v = \theta\frac{1+(R_v q_v)/R_d}{1+q_v} \approx \theta(1+0.608q_v), \tag{4.8}$$

where R_v is the gas constant of water vapor and R_d is the gas constant of dry air. Additionally, the Exner function is now a diagnostic variable. Upon using the ideal gas law ($p = \rho_d(1+q_v)R_d\theta_v\Pi$),

$$\Pi = \left(\frac{p}{p_o}\right)^{R_d/c_{pd}} = \left(\frac{R_d}{p_o}\rho_d(1+q_v)\theta_v\right)^{R_d/c_{vd}}, \tag{4.9}$$

where p is the pressure, p_o is the base state pressure at the surface, and c_{vd} is the specific heat of dry air at constant volume.

Summing (4.5)-(4.7) yields a conservation equation for the total mass:

$$\frac{\partial \rho_t}{\partial t} = -\nabla \cdot (\mathbf{u}\rho_t) - \frac{\partial}{\partial z}(v_T \rho_l) + D_{\rho_v} + D_{\rho_l}, \tag{4.10}$$

where $\rho_t = \rho_d + \rho_v + \rho_l$ is the total density. The second term on the right hand side of (4.10) reflects the the effect of falling precipitation on the mass budget. As studied in Qiu et al. (1993) and Lackmann and Yablonsky (2004), this effect is not negligible in heavily precipitating systems, such as tropical cyclones. The latter study found that including the precipitation term leads to higher intensities in TC simulations.

Entropy Equation

A number of cloud models have used moist entropy as a prognostic variable in order to take advantage of the fact that it is conserved for reversible moist adiabatic processes and absolves one from having to explicitly compute diabatic heating due to phase changes. For example, Ooyama (1990) and Ooyama (2001) proposed a dual state entropy formulation for moist numerical models depending on the presence of condensate, and Zeng et al. (2005) developed a model with a comprehensive moist entropy equation to study the interaction between clouds and large-scale circulations.

Commonly, approximations to the full entropy equation are made in order to arrive at a more tractable expression and to save computational costs. Such expressions can be generated by ignoring the effects of liquid water and ice on the total entropy and/or the dependence of the latent heat of vaporization on temperature (Lipps and Hemler, 1980). The RE87 model neglects the change in condensation temperature[1] to form an entropy expression. Similarly, Tripoli and Cotton (1981) and Bryan and Fritsch (2004) developed various approximations of the ice-liquid water potential temperature, which is also conserved for reversible moist-adiabatic processes, for use in atmospheric models simulating deep convection.

Precipitation and evaporation lead to sources of moist entropy or ice-liquid water potential temperature necessitating a unwieldy amount of accounting of microphysical processes. To avoid this, the pseudoadiabatic entropy (s_p) is derived by neglecting

---

[1] The condensation temperature is the temperature at the lifting condensation level for an unsaturated parcel and is equal to the temperature for a saturated parcel.

the heat capacity of liquid water and ice or removing all condensate upon formation. However, the full form of the pseudoadiabatic entropy is not useful in that it contains a term that must be numerically integrated (cf. Emanuel (1994) pg. 132). As a result, empirical and analytical approximations have been developed approximating the pseudoadiabatic entropy (Bolton, 1980; Bryan, 2008; Davies-Jones, 2009). Of course, reality lies somewhere between the pseudoadiabatic and reversible extremes.

In arriving at an entropy equation for this TC model, the goal is to keep it as simple as possible so that budgets may be calculated both easily and accurately. Simplicity can be achieved through the psuedoadibatic approach, which will be used to derive the model's entropy conservation equation. It should be emphasized that the model's handling of moist entropy doesn't apply strictly to reality, but is close enough to be able to tractably study TC processes and probably other heavily precipitating phenomena.

The model's entropy equation, given by (4.4), is now derived. Upon ignoring the contribution of liquid water, the first law of thermodynamics for moist air can be expressed as

$$ds_p = \left(c_{pd} + q_v c_l\right) d\ln(T) + d\left(\frac{L_v q_v}{T}\right) - R_d d\ln(p_d) - R_v d\left(q_v \ln H\right), \tag{4.11}$$

where c_l is the specific heat of liquid water, L_v is the latent heat of vaporization, T is the temperature, p_d is the dry pressure, and H is the relative humidity. Bryan (2008) noted that the $q_v c_l d\ln T$ term can be ignored for a wide range of atmospheric conditions by compensating it with a fixed, inflated value of $L_v = L_{vo}$. Following this approach, (4.11) becomes

$$ds_p = c_{pd} d\ln(T) + L_{vo} d\left(\frac{q_v}{T}\right) - R_d d\ln(p_d) - R_v d\left(q_v \ln H\right), \tag{4.12}$$

which results in an integrable expression. For convenience, the reference state is defined to be at a temperature of 1 K, a water vapor mixing ratio of 0 kg kg^{-1}, and a dry pressure of 1 Pa. Integrating (4.12) from a reference state to saturation (lifting condensation level), as done in Bolton (1980), results in

$$s_p = c_{pd}\ln(T_L) + \frac{L_{vo}q_{vL}}{T_L} - R_d\ln(p_{dL}), \tag{4.13}$$

where variables with subscripts of "L" are evaluated at the saturation level. Expressing (4.13) in terms of a dry potential temperature at the saturation level (θ_{dL}),

$$s_p = c_{pd}\ln(\theta_{dL}) + \frac{L_{vo}q_{vL}}{T_L} - R_d\ln(p_o), \tag{4.14}$$

where θ_{dL} can be related to θ by (Davies-Jones, 2009)

$$\theta_{dL} = \theta\left[\left(\frac{\theta}{T_L}\right)^{0.28q_v}\left(1+\frac{R_v q_v}{R_d}\right)^{R_d/c_{pd}}\right] \approx \theta. \tag{4.15}$$

Since q_v is small, the term in brackets is nearly one and θ usually differs from θ_{dL} by less than 1%. As a result, θ is subsitutued in place of θ_{dL} to simplify (4.14).

The final simplification to (4.14) is to substitute in an empirical relationship for T_L, since a simple analytical formula for T_L does not exist. T_L is a function of both θ and q_v but is most sensitive to q_v for the range of atmospheric conditions of interest, namely the mean tropics. To demonstrate this, Fig. 4-1 shows T_L curves as a function of q_v. Each curve is for a different pair of approximate temperatures and pressures from the Jordan mean hurricane season sounding (Jordan, 1958), but with the relative humidity varying from 10% to 100%. T_L is calculated using the empirical formula from Bolton (1980):

$$T_L = \frac{2840}{3.5\ln(T) - \ln(e) - 4.805} + 55, \tag{4.16}$$

where e is the vapor pressure. To a reasonable degree, the curves fall on top of one another indicating little sensitivity of T_L to combinations of mean temperature and pressure found in the tropics. Therefore, T_L can be approximated solely by q_v. Applying a logarithmic fit to the data in a least squares sense results in the following empirical parameterization for T_L, which is defined as $\hat{T_L}$:

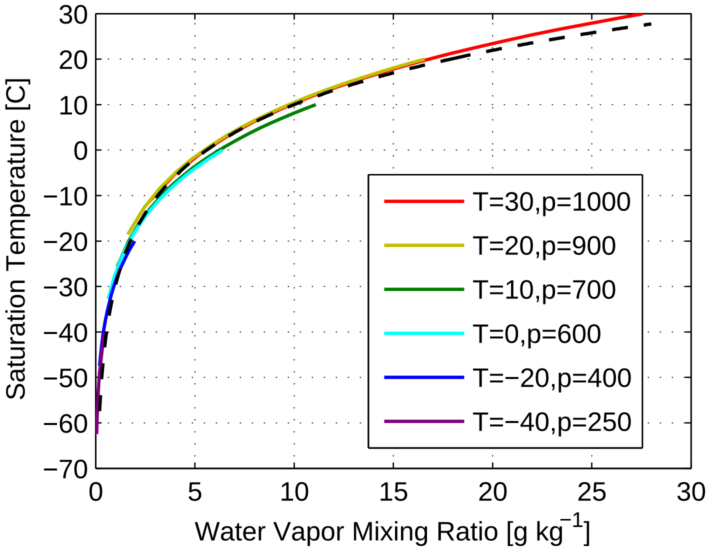

Figure 4-1: The saturation temperature, T_L, as a function of the water vapor mixing ratio, q_v, where each curve is for a fixed combination of temperature and pressure. The endpoints of each curve are at 10% and 100% relative humidity. The empirical fit for T_L is given by the dashed, black line.

$$\hat{T}_L = \mathrm{MAX}(A\ln(q_v) + B, A), \tag{4.17}$$

where $A = 17.23$ and $B = 362.48$. The empirical curve representing $\hat{T}_L$ is plotted in Fig. 4-1 as the dashed, black line. It will be clear later why $\hat{T}_L$ cannot be allowed drop below A. Additionally, it should be emphasized that (4.17) is calibrated for a mean tropical environment and would need to be recalibrated for other purposes.

Using (4.15) and (4.17) results in a simplified expression for s_p:

$$s_p = c_{pd}\ln(\theta) + \frac{L_{vo}q_v}{\hat{T}_L} - R_d\ln(p_o), \tag{4.18}$$

or in terms of an pseudoequivalent potential temperature (θ_{ep}),

$$\theta_{ep} = \theta\exp\left(\frac{L_{vo}q_v}{c_{pd}\hat{T}_L}\right), \tag{4.19}$$

such that $s_p = c_{pd}\ln(\theta_{ep}) - R_d\ln(p_o)$. Solving for θ in (4.18) results in a diagnostic equation for the potential temperature:

$$\theta = \exp\left[\frac{1}{c_{pd}}\left(s_p + R_d \ln(p_o) - \frac{L_{vo} q_v}{\hat{T_L}}\right)\right]. \tag{4.20}$$

There is a clear advantage in expressing T_L only in terms of q_v, as it makes the second term on the right hand side of (4.18) or the exponent in (4.19) only a function of q_v. This simple dependence on q_v allows for an equally simple conservation equation for s_p that can be derived by taking the total derivative of (4.18):

$$\frac{ds_p}{dt} = \frac{c_{pd}}{\theta}\frac{d\theta}{dt} + \frac{L_{vo}(\hat{T_L} - A)}{\hat{T_L}^2}\frac{dq_v}{dt}. \tag{4.21}$$

Clearly, $\hat{T_L}$ cannot be allowed to be less than A, as this would correspond to a negative latent energy. For unsaturated adiabatic displacements, both θ and q_v are conserved resulting in the desired property that s_p is also conserved. For saturated adiabatic displacements, condensation (evaporation) and latent heating (cooling) are constrained to conserve s_p. The procedure for satisfying this is elaborated upon the microphysics section.

The fixed value of the latent heat of vaporization is the remaining parameter that must be calibrated. Bryan (2008) and Davies-Jones (2009) both optimized approximations of s_p using inflated values of L_{vo} in order minimize the error in s_p. A similar approach is taken here by comparing (4.19) with a highly accurate formula devised by Davies-Jones (2009)[2]. Similar to T_L, the optimization is performed for temperature profiles that are ±5 K around the Jordan mean hurricane season sounding along with the full range of relative humidity. The root mean square error (RMSE) for different values of L_{vo} are shown in Fig. 4-2. The optimal value of L_{vo} is 2.678×10^6 J kg^{-1} with a minimum RMSE of 0.24, which is comparable to other approximations of θ_{ep}. Note that the optimal value of L_{vo} will differ slightly when considering different atmospheric states other than a mean tropical sounding.

Using the optimized value of L_{vo}, the difference in temperature and water vapor mixing ratio profiles between two initially identical parcels (T = 28°C, H = 75%,

---

[2] See equation (6.5) in Davies-Jones (2009) for a θ_{ep} formula that is accurate to within 0.095 K for wet-bulb potential temperatures less than 40°C.

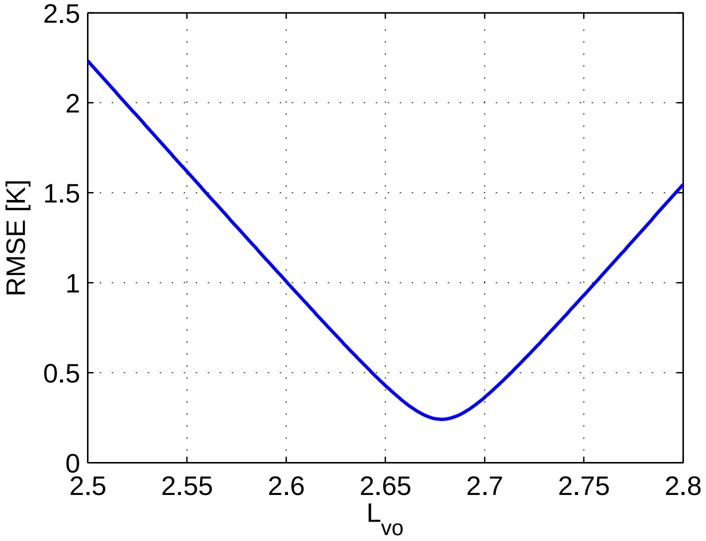

Figure 4-2: The root mean squared error of the pseudoequivalent potential temperature, θ_{ep}, as a function of fixed values of the latent heat of vaporization, L_{vo}.

and $p = 1015$ hPa) lifted using (4.21) and (4.11) is shown in Fig. 4-3. Errors are small below the lifting condensation level. Above the lifting condensation level, the parcel tends to be slightly too warm and moist. The temperature error is largest in the middle to upper troposphere, while the water vapor mixing ratio error is largest at midlevels.

Although effort is taken to make the current formulation of pseudoadiabatic entropy behave as closely as possible to the numerical equivalent, the exact value of L_{vo} is not imperative to the formulation of the model itself as long as it does not differ wildly from the reasonable range of L_v. What is imperative is that the microphysics, radiation, and turbulence parameterizations, along with the initial conditions, are consistent with the entropy formulation.

4.2.2 Microphysics

As done in the RE87 model, cloud water and rain water are not considered separately. When $q_l \leq 1\text{g kg}^{-1}$, all liquid water is in the form of cloud droplets with a terminal velocity of zero. On the other hand, when $q_l > 1\text{g kg}^{-1}$, all liquid water is converted

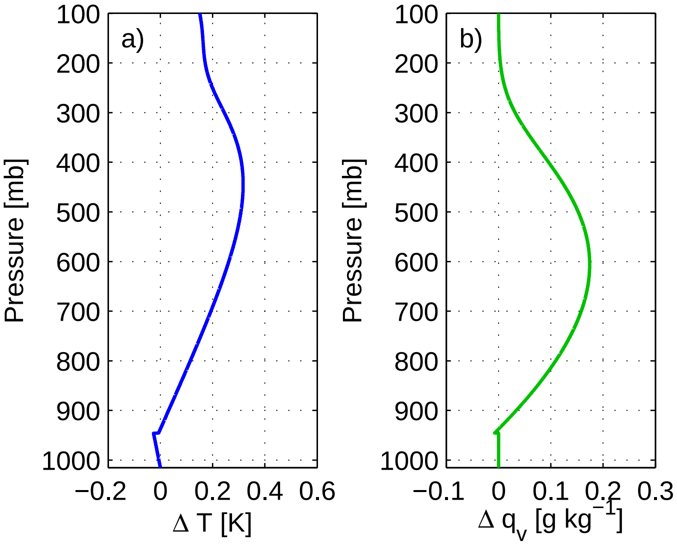

Figure 4-3: The difference in (a) temperature and (b) water vapor mixing ratio between two initially identical parcels lifted pseudoadiabatically using the current formulation (4.21) and the full formulation (4.11).

to rainwater and falls at a terminal velocity of -7 m s^{-1}. Although this is a drastic simplification, it eliminates a prognostic variable and the need to include a microphysics parameterization that converts cloud to rain water and vice versa. Thus, all condensation and evaporation occurs at the grid scale. The condensation algorithm is similar to that outlined in Klemp and Wilhelmson (1978), with the requirement that s_p be conserved.

The saturation vapor pressure (e^*) is approximated using Tetens' formula, given by

$$e^* = 6.112\exp\left[\frac{17.67(T-273.15)}{T-29.65}\right]. \tag{4.22}$$

Equation (4.22) is linearized about the initial temperature, T^i, before any phase change takes place. Upon keeping the first two terms in the Taylor expansion and evaluating at the final state after the phase change, given by the superscript “f”,

$$e^{*f} = e^{*i}\left[1+\frac{4302.645}{(T^i-29.65)^2}\left(T^f-T^i\right)\right]. \tag{4.23}$$

Assuming the phase change occurs isobarically, $\delta T = \Pi \delta\theta$. Additionally, q_v^* can be substituted wherever e^* appears:

$$q_v^{*f} = q_v^{*i} \left[1 + \frac{4302.645}{(\theta^i \Pi - 29.65)^2} \Pi \left(\theta^f - \theta^i \right) \right] . \tag{4.24}$$

Next, the change in potential temperature can be related to the change in water vapor mixing ratio by using (4.21) for constant s_p:

$$\theta^f - \theta^i = \frac{-L_{vo} \theta (\hat{T}_L - A)}{c_{pd} \hat{T}_L^{\,2}} \left(q_v^{*f} - q_v^i \right) . \tag{4.25}$$

Substituting (4.25) into (4.24) and rearranging results in an expression for the condensation/evaporation, $M_{q_l} \Delta t = q_v^i - q_v^{*f}$:

$$M_{q_l} \Delta t = \begin{cases} \frac{q_v^i - q_v^{*i}}{(1 + \chi q_v^{*i})} & \text{if } H > 1 \\ \mathrm{MAX} \left(\frac{q_v^i - q_v^{*i}}{(1 + \chi q_v^{*i})}, -q_l^i \right) & \text{if } H < 1 \text{ and } 0 < q_l \leq 1 \times 10^{-3} \\ \frac{\Delta t}{\hat{\tau}_{\mathrm{evap}}} \mathrm{MAX} \left(\frac{q_v^i - q_v^{*i}}{(1 + \chi q_v^{*i})}, -q_l^i \right) & \text{if } H < 1 \text{ and } q_l > 1 \times 10^{-3} \end{cases} , \tag{4.26}$$

where

$$\chi = \frac{4302.645 \theta \Pi L_{vo} (\hat{T}_L - A)}{c_{pd} \hat{T}_L^{\,2} (\theta \Pi - 29.65)^2} \tag{4.27}$$

and Δt is the model time step. The physical effect of (4.26) is to form liquid water at supersaturated locations and evaporate rain in unsaturated air. In doing so, sensible heat is added to or subtracted from the local environment in order to conserve s_p. In the RE87 model, evaporation is assumed to occur just as rapidly as condensation and is limited only by the amount of liquid water present, i.e. the relative humidity is constrained to be 100% in the presence of liquid water. While this assumption is good for cloud droplets, it overestimates the rate of evaporation of raindrops falling through unsaturated air, which can have an evaporation timescale on the order of tens of minutes.

As a correction to the evaporation overestimation, an evaporation limiter ($\Delta t / \hat{\tau}_{\mathrm{evap}}$)

is included when q_l exceeds 1 g kg^{-1}. The evaporation limiter can be derived by considering the change in mass of a raindrop falling freely through the air, which is governed by the equation

$$\frac{1}{m}\frac{dm}{dt} = -\frac{3c_v D\Delta\rho_v}{a^2\rho_w}, \tag{4.28}$$

where m is the mass of the droplet, c_v is the "ventilation coefficient" that takes into account air moving around the drop[3], D is the diffusion coefficient, $\Delta\rho_v$ is the change in water vapor density from the surface of the drop to the surrounding environment, a is the radius of the drop, and ρ_w is the density of liquid water (Kinzer and Gunn, 1951). By assuming a homogeneous number of drops per unit volume and constant dry density of the local environment during the evaporation process, m can be replaced by q_l. Moreover, if one assumes the right hand side of (4.28) is constant, then its inverse represents an e-folding timescale for the change in q_l due to evaporation:

$$\tau_{\text{evap}} = \frac{a^2\rho_w}{3c_v D\Delta\rho_v}. \tag{4.29}$$

The parameters in (4.29) are empirically estimated in Tab. 1 and Tab. 2 of Kinzer and Gunn (1951). Assuming a rain drop diameter of 2.2 mm, corresponding roughly to a terminal velocity of -7 m s^{-1} (Gunn and Kinzer, 1949), and a temperature of 20°C, τ_{evap} becomes only a function of the relative humidity, as shown in Fig. 4-4 by the crosses. The evaporation timescale increases with relative humidity, especially as the environment approaches saturation. For a relative humidity of 10%, the timescale is about 6 minutes and increases to about an hour when the relative humidity is 90%. Hence, it becomes progressively harder to saturate the atmosphere solely from the evaporation of rain unless it is raining in the same location for a long period of time.

Since the data from Kinzer and Gunn (1951) is discrete, it is fitted to a tangent curve, as shown by the blue line in Fig. 4-4, with the equation of the tangent curve being

---

[3] This is not to be confused with the ventilation ($\mathcal{V}$) defined in previous chapters.

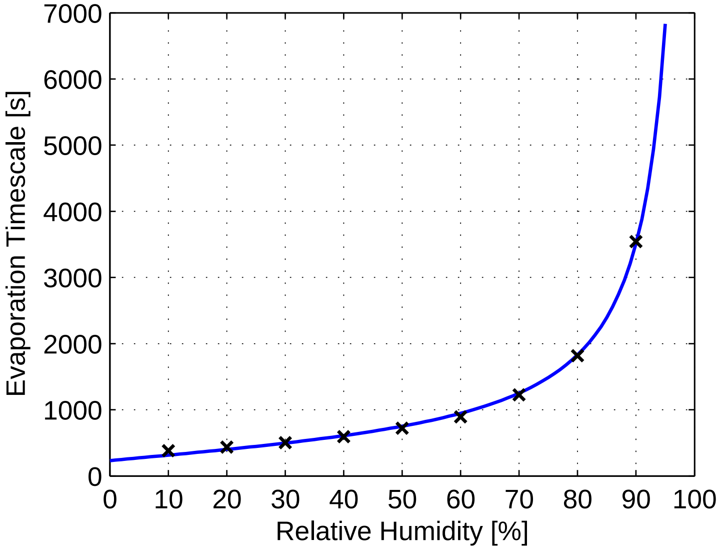

Figure 4-4: The evaporation timescale, τ_{evap}, as a function of the relative humidity. The timescale is derived from Kinzer and Gunn (1951) data for a drop diameter of 22 mm and a temperature of 20°C (crosses). The least squares tangent curve fit to the data is given by the blue line.

$$\hat{\tau}_{\text{evap}} = 519.59 \tan\left(\frac{\pi H}{2}\right) + 231.83. \tag{4.30}$$

This timescale is used to reduce the evaporation rate to more reasonable levels in (4.26) when rain falls through unsaturated air. The main effect of the evaporation limiter is to reduce the evaporation in the boundary layer below the eyewall, thereby increasing rain rates and decreasing relative humidities, as inflow is not instantaneously saturated as it crosses into the heavily precipitating eyewall annulus.

In practice, the condensation/evaporation algorithm should be iterated because (4.27) is modified by phase changes. Condensation, for instance, results in an increase in the temperature and a corresponding small decrease in χ. However, only a few iterations are needed to achieve convergence. The evaporation limiter should only be applied once after the iteration is complete.

Rain falling and evaporating in to unsaturated air is an irreversible process, and in reality, there should be a slight increase in entropy. If evaporation is required to conserve enthalpy, instead of entropy, it can be shown that the change in entropy due to evaporation is

$$ds_p\big|_{\text{evap}} \approx L_{vo}\left(\frac{T-\hat{T}_L}{T\hat{T}_L}\right) dq_v\big|_{\text{evap}}\,, \tag{4.31}$$

as long as $\hat{T}_L >> A$. Since $T \geq \hat{T}_L$, the right hand side of (4.31) must be ≥ 0 resulting in a gain of entropy as evaporation takes place. The model ignores the contribution of this irreversible source of entropy (along with other irreversible sources) in order to be consistent with the complimenting theoretical framework. The effect of irreversible sources of entropy on TC evolution in this model will be looked at in the future.

4.2.3 Turbulence

TCs contain a full spectrum of nonaxisymmetric phenomena that an axisymmetric model cannot represent. Consequently, their effects must be parameterized. The turbulence parameterization follows RE87's parameterization closely, but must be adjusted so that saturated mixing conserves s_p. Moreover, the dry, compressible equations are used instead of the incompressible equations to formulate the turbulence parameterization. This allows the resulting turbulence terms to fit in more neatly with the numerical scheme presented below. The resulting turbulent terms in (4.1)-(4.7) are

$$D_U = \frac{1}{r}\frac{\partial r\tau_{rr}}{\partial r} + \frac{\partial \tau_{rz}}{\partial z} - \frac{\tau_{\phi\phi}}{r} \tag{4.32}$$

$$D_V = \frac{1}{r^2}\frac{\partial r^2\tau_{r\phi}}{\partial r} + \frac{\partial \tau_{\phi z}}{\partial z} \tag{4.33}$$

$$D_W = \frac{1}{r}\frac{\partial r\tau_{rz}}{\partial r} + \frac{\partial \tau_{zz}}{\partial z} \tag{4.34}$$

$$D_X = -\frac{1}{r}\frac{\partial rF_r^x}{\partial r} - \frac{\partial F_z^x}{\partial z}, \tag{4.35}$$

where $X \in \{S_p, \rho_v, \rho_l\}$ and $x \in \{s_p, q_v, q_l\}$. The components of the stress tensor are

$$\begin{pmatrix} \tau_{rr} & \tau_{r\phi} & \tau_{rz} \\ & \tau_{\phi\phi} & \tau_{\phi z} \\ & & \tau_{zz} \end{pmatrix} = \begin{pmatrix} 2\mu_h \left(\frac{\partial u}{\partial r} - \frac{1}{3}\nabla\cdot\mathbf{u}\right) & \mu_h r \frac{\partial}{\partial r}\left(\frac{v}{r}\right) & \mu\left(\frac{\partial u}{\partial z} + \frac{\partial w}{\partial r}\right) \\ & 2\mu_h\left(\frac{u}{r} - \frac{1}{3}\nabla\cdot\mathbf{u}\right) & \mu\left(\frac{\partial v}{\partial z}\right) \\ & & 2\mu\left(\frac{\partial w}{\partial z} - \frac{1}{3}\nabla\cdot\mathbf{u}\right) \end{pmatrix}, \tag{4.36}$$

where only the upper right part of the tensor is shown because it is symmetric. These equations are similar to those used in the RE87 and Bryan and Rotunno (2009b) models, with the exception of the added divergence in the diagonal terms of the stress tensor and the replacement of the kinematic viscosity with the dynamic viscosity. The turbulent fluxes of the remaining scalar variables are

$$(F_r^x, F_z^x) = -\left(\mu_h \frac{\partial x}{\partial r}, \mu \frac{\partial x}{\partial z}\right). \tag{4.37}$$

At the lower boundary, the tangential stress and turbulent fluxes are given by the bulk aerodynamic formulas:

$$\tau_{rz}(z=0) = C_D \rho_d u \sqrt{u^2+v^2} \tag{4.38}$$

$$\tau_{r\phi}(z=0) = C_D \rho_d v \sqrt{u^2+v^2} \tag{4.39}$$

$$F_z^{s_p}(z=0) = C_k \rho_d \sqrt{u^2+v^2}(s_p^*|_{\text{SST}} - s_p) \tag{4.40}$$

$$F_z^{q_v}(z=0) = C_k \rho_d \sqrt{u^2+v^2}(q_v^*|_{\text{SST}} - q_v), \tag{4.41}$$

where C_D is the drag coefficient, C_k is the enthalpy exchange coefficient, and the variables are evaluated at the lowest model level. C_D is given by a modified Deacon's formula:

$$C_D = \text{MIN}\left(1.1\times10^{-3} + 4\times10^{-5}\sqrt{u^2+v^2},\ 3.0\times10^{-3}\right), \tag{4.42}$$

which assumes a linear increase in C_D with wind speed. C_D is capped at a maximum value of 3.0×10^{-3}, which is simple way of taking in to account that C_D flattens and decreases at high wind speeds (Powell et al., 2003). The value of the cap is chosen to be quite high given uncertainties in the exact values of C_D at high wind speeds. For the intensity, the ratio of the enthalpy exchange coefficient to the drag coefficient is much more critical. Coupled Boundary Layer Air-Sea Transfer (CBLAST) data indicates that the ratio of C_k to C_D tends to decrease from a value of 1 at low winds speeds to about 0.7 for wind speeds just shy of hurricane strength (Edson et al., 2007; Black et al., 2007). For winds stronger than hurricane force, there is little knowledge of how the ratio behaves. Setting the ratio to the lowest values of the CBLAST data prevents storms from intensifying in the RE87 model (Emanuel, 1995). On the contrary, the intensity in 3D simulations appears to show little sensitivity to the ratio of C_k to C_D (Montgomery et al., 2010). For the purposes of this study, C_k is set equal to C_D to prevent the introduction of another degree of freedom that would make it harder to compare the model results to the steady-state theory.

The viscosity is derived in a same manner as in Lilly (1962) and Klemp and Wilhelmson (1978), but care must be taken to ensure that the buoyancy flux satisfies entropy conservation. In equilibrium conditions, the turbulent kinetic energy satisfies the relationship:

$$\nu\sigma^2 + F_z^b = \epsilon, \tag{4.43}$$

where ν is the kinematic viscosity, σ is the deformation, F_z^b is the buoyancy flux, and ϵ is the dissipation. The contribution of the horizontal deformation (σ_h) and dissipation (ϵ_h) is isolated and solved separately to reflect the anisotropic nature of the mixing due to the model having a much larger radial grid spacing compared to vertical grid spacing (Mason and Sykes, 1982; Bryan and Rotunno, 2009b):

$$\nu_h\sigma_h^2 = \epsilon_h, \tag{4.44}$$

The deformation is defined as

$$\sigma_h^2 = 2\left(\frac{\partial u}{\partial r}\right)^2 + 2\left(\frac{u}{r}\right)^2 + \left(\frac{\partial v}{\partial r} - \frac{v}{r}\right)^2,$$

$$\sigma^2 = \sigma_h^2 + 2\left(\frac{\partial w}{\partial z}\right)^2 + \left(\frac{\partial u}{\partial z} + \frac{\partial w}{\partial r}\right)^2 + \left(\frac{\partial v}{\partial z}\right)^2. \tag{4.45}$$

The buoyancy flux is defined as

$$F_z^b = g\left(\frac{\overline{w'\theta_v'}}{\theta_v} - \overline{w'q_l'}\right), \tag{4.46}$$

where the contribution of liquid water is included because it exists in both saturated and unsaturated conditions. For saturated conditions, (4.46) must be reexpressed in order to conserve entropy. Using the approximation that

$$\frac{\theta_v'}{\theta_v} \approx \frac{\theta'}{\theta} + 0.608 q_v' \tag{4.47}$$

and a relationship between turbulent vertical fluxes of water vapor and temperature with the help of the Clausius-Clapeyron equation:

$$\overline{w'q_v'} \approx \frac{L_{vo} q_v}{R_v \theta T} \overline{w'\theta'}, \tag{4.48}$$

(4.46) becomes

$$F_z^b = g\left[\left(\frac{1}{\theta} + 0.608 \frac{L_{vo} q_v}{R_v \theta T}\right) \overline{w'\theta'} - \overline{w'q_l'}\right]. \tag{4.49}$$

Conservation of entropy requires

$$\overline{w's_p'} = \frac{c_{pd}}{\theta} \overline{w'\theta'} + L_{vo}\left(\frac{\hat{T}_L - A}{\hat{T_L}^2}\right) \overline{w'q_v'}. \tag{4.50}$$

Upon using (4.48) and solving for $\overline{w'\theta'}$,

$$\overline{w'\theta'} = \frac{\overline{w's_p'}}{\frac{c_{pd}}{\theta} + \frac{L_{vo}^2 q_v}{R_v \theta T} \frac{\hat{T}_L - A}{\hat{T_L}^2}}. \tag{4.51}$$

Substituting (4.51) into (4.49) results in an expression for the buoyancy flux in saturated air:

$$F_z^b = g\left(\gamma\overline{w's_p'} - \overline{w'q_l'}\right) \tag{4.52}$$

where

$$\gamma = \frac{\left(1 + 0.608\frac{L_{vo}q_v}{R_vT}\right)}{c_{pd} + \frac{L_{vo}^2 q_v}{R_vT}\frac{\hat{T_L}-A}{\hat{T_L}^2}} \tag{4.53}$$

Lastly, the Reynold's fluxes are eliminated using a first order closure:

$$F_z^b = \begin{cases} -\nu g\left(\frac{1}{\theta_v}\frac{\partial\theta_v}{\partial z} - \frac{\partial q_l}{\partial z}\right) & \text{if unsaturated} \\ -\nu g\left(\gamma\frac{\partial s_p}{\partial z} - \frac{\partial q_l}{\partial z}\right) & \text{if saturated} \end{cases}, \tag{4.54}$$

In order to combine the two expressions for buoyancy flux in to a single expression, a weighting function is used in order to shift between the two expressions in (4.54) quickly when saturation is approached:

$$F_z^b = -\nu\,\underbrace{g\left[(1-\omega)\left(\frac{1}{\theta_v}\frac{\partial\theta_v}{\partial z} - \frac{\partial q_l}{\partial z}\right) + \omega\left(\gamma\frac{\partial s_p}{\partial z} - \frac{\partial q_l}{\partial z}\right)\right]}_{b_z}, \tag{4.55}$$

where

$$\omega = 0.5\tanh\left[50(H - 0.95)\right] + 0.5. \tag{4.56}$$

A transition between unsaturated and saturated states is more natural than a switch-like effect implied by strictly using (4.54). As the average relative humidity within a grid box gets close to saturation, it becomes increasingly likely that a growing proportion of the grid box is already saturated. Hence, (4.55) attempts to account for possible inhomogeneities through a weighted average of unsaturated and saturated buoyancy fluxes.

Based on dimensional grounds,

$$\epsilon = \frac{\nu^3}{l^4}, \; \epsilon_h = \frac{\nu_h^3}{l_h^4} \tag{4.57}$$

where $l_{(h)}$ is the length scale of the most energetic eddies. Using (4.45), (4.55), and (4.57) in (4.43) and (4.44) and multiplying by ρ_d results in expressions for μ and μ_h:

$$\mu = \rho_d l^2 \sqrt{\sigma^2 - b_z} = \rho_d l^2 \sigma \sqrt{1 - \mathrm{Ri}} \tag{4.58}$$

$$\mu_h = \rho_d l_h^2 \sigma_h, \tag{4.59}$$

where Ri is the (flux) Richardson number. If Ri>1, then the flow is dynamically stable and μ is set to zero. For locations where μ exceeds μ_h, μ_h is set to the value of μ, such that the mixing is isotropic.

TC intensity in numerical models is sensitive to the values of l and particularly l_h (Bryan and Rotunno, 2009b). In the limit of vanishing l_h, frontogenesis collapses the eyewall entropy front to the radial resolution of the model yielding extremely intense storms at high resolution. On the other hand, setting l_h to a value greater than 3000 km causes the entropy gradient at the eyewall to become quite diffuse resulting in weak intensities. Based on the findings in the Bryan and Rotunno (2009b) study, l is set to 100 m and l_h is set to 1500 m. These eddy length scales seem to yield reasonable representations of the intensity evolution in the current model.

4.2.4 Dissipative Heating

Dissipative heating has been shown to be an important component of the TC's energy budget. Dissipative heating in the surface layer recycles heat into the warm reservoir of the TC heat engine leading to an increase in wind speed and a decrease in pressure (Bister and Emanuel, 1998). Jin et al. (2007) also found that the heating caused by internal dissipation of turbulent kinetic energy is important for TC intensity.

Following the approach of Bister and Emanuel (1998), the dissipation is calculated by collecting terms of the form $\mu \left(\nabla u_i\right)^2$ from the kinetic energy equation. The dissipative heating is then calculated by dividing the sum of the terms by $c_{pd}\Pi\rho_d$. In the interior,

$$\begin{aligned}\mathcal{H} =& \frac{1}{c_{pd}\Pi\rho_d}\left\{\mu_h\left[\frac{4}{3}\left(\frac{\partial u}{\partial r}\right)^2+\left(\frac{\partial v}{\partial r}\right)^2\right]\right.\\ &\left.+\mu\left[\left(\frac{\partial u}{\partial z}\right)^2+\left(\frac{\partial v}{\partial z}\right)^2+\left(\frac{\partial w}{\partial r}\right)^2+\frac{4}{3}\left(\frac{\partial w}{\partial z}\right)^2\right]\right\}, \end{aligned}\tag{4.60}$$

and at the lowest model level,

$$\begin{aligned}\mathcal{H}(z=\Delta z/2) =& \frac{1}{c_{pd}\Pi\rho_d}\left\{\mu_h\left[\frac{4}{3}\left(\frac{\partial u}{\partial r}\right)^2+\left(\frac{\partial v}{\partial r}\right)^2\right]\right.\\ &\left.+\mu\left[\left(\frac{\partial w}{\partial r}\right)^2+\frac{4}{3}\left(\frac{\partial w}{\partial z}\right)^2\right]+\frac{2C_D\rho_d}{\Delta z}(u^2+v^2)^{3/2}\right\}, \end{aligned}\tag{4.61}$$

where Δz is the vertical grid size. The dissipative heating is dominated by (4.61) due to the large surface stress term proportional to the cube of the wind speed.

4.2.5 Radiation

Radiation is a necessary part of a TC's thermodynamic cycle. Radiation balances subsidence due to the secondary circulation and also helps maintain a reservoir of available potential energy to power the TC. The radiation is prescribed through Newtonian cooling,

$$R = -\frac{\theta-\overline{\theta}}{\tau_R}. \tag{4.62}$$

where $\overline{\theta}$ is the initial potential temperature profile and τ_R is a relaxation time scale. The effect of the parameterization is to maintain the far field away from the inner core of the TC at some initial, neutral thermal profile. The relaxation time scale is chosen to be 12 hours, which is the same value used in RE87. To prevent excessive cooling of the TC's warm core, it is required that $|R| < 2$ K day^{-1}, which is an approximate upper bound on the radiative cooling in clear-sky conditions in the tropics (Hartmann et al., 2001). The effect of clouds on the radiation budget is not considered.

4.2.6 Numerical Methods

The prognostic variables are staggered using an Arakawa-C grid (Arakawa and Lamb, 1977) with a radial grid spacing of 2 km and a vertical grid spacing of 300 m. For each grid box, U is located at the radial faces, W is located at the vertical faces, and the remainder of the variables are located at the center of the grid box. This structured grid lends itself readily to the governing equations discretized using a finite volume method. The basic principal of finite volume methods is to apply a volume average to a partial differential equation and then use the divergence theorem to express flux and diffusion terms as fluxes through the sides of each grid cell. As a consequence, conservation of momentum, mass, and entropy is guaranteed to numerical precision when there are neither fluxes at the boundaries of the computational domain nor internal sources.

The flux terms are calculated using a high resolution corner transport method, which accounts for fluxes between boxes that share faces or corners (LeVeque, 2002). This allows better accuracy especially if flow occurs along diagonals of grid cells, such as what might occur in the slantwise flow of a TC. High resolution schemes are hybrid first-order upwind and second-order centered (Lax-Wendroff) schemes. The second-order part of the scheme has more weight near large gradients such as fronts in order to prevent excessive diffusion inherent in the upwind scheme. However, the second-order scheme produces spurious oscillations since it is not “total variation diminishing.” To prevent this, a monotonized central flux limiter is used, which makes the scheme total variation diminishing and conservative. Details of finite volume schemes, flux limiters, and an algorithm for application of the high resolution corner transport method in curvilinear coordinates are given in Ch. 5 of Durran (1999).

Time stepping is performed using an explicit third-order Runge-Kutta (RK3) method with a split time-step (Wicker and Skamarock, 2002; Klemp et al., 2007). The method splits the time integration into short time steps (Δt_s) and long time steps (Δt_l). At the beginning of each long time step, the forcings for the prognostic variables are calculated except for terms that support acoustic and gravity waves. Terms that support acoustic and gravity waves - the pressure gradient, the buoyancy, and dry density flux terms - are integrated on the short time step using the forward-backward scheme of Mesinger (1977), with the long time step forcing terms held constant. For each iteration of the RK3 method, the small time step integration is carried out to a successively increasing fraction of the long time step ($\Delta t_l/3$, $\Delta t_l/2$, Δt_l). After each iteration, the long time step forcing terms are recalculated using the intermediate values of the prognostic variables, and the state is reset back to the beginning of the long time step for the next iteration. The main advantage of the RK3 method is its generous Courant numbers, which allows a larger time step than other explicit schemes. Further details on the scheme can be found in Wicker and Skamarock (2002).

The model is still somewhat unstable to acoustic modes. In order to preferentially damp acoustic modes, the Exner function is modified to be

$$\Pi^{\star} = \Pi(t_o) + \beta \left(\Pi(t_o) - \Pi(t_o - \Delta t_s)\right) \tag{4.63}$$

where β is the acoustic damping coefficient and the second term is the change in Π over the previous small time step. Following Klemp et al. (2007), β is set to 0.1. The effect of (4.63) can be seen by forming a divergence equation from the momentum equations. Substituting $\Pi^{\star}$ into the divergence equation yields a term that effectively damps the divergence of high frequency modes. Furthermore, using $\Pi^{\star}$ in the pressure gradient terms in lieu of adding divergence damping terms to each of the momentum equations (Skamarock and Klemp, 1992) is much more computationally efficient.

Reflection of gravity waves at the outer boundary (r=1000 km) is prevented by specifying an "outflow" boundary condition, following Klemp and Wilhelmson (1978) and RE87 modified for the finite volume framework. The radial momentum in the outermost grid box is fluxed out of the domain with a radial velocity of $u + c$, where c is an intrinsic gravity wave phase velocity (30 m s^{-1}). If $u + c < 0$, then the flux of radial momentum out of the domain is set to zero. The vertical momentum in the outermost grid box is also fluxed out of the domain if $u > 0$ and set to zero if $u < 0$. It appears that applying the boundary condition to these two variables is sufficient to allow gravity wave energy to exit. For the remainder of the prognostic variables, a Dirichlet condition is used for the radial flux terms, as an outflow boundary condition causes the mass and pressure in the computational domain to slowly drift.

At the top of the domain (z=24 km), a sponge layer is used with implicit Rayleigh damping (Klemp et al., 2008). After the vertical momentum is integrated forward in the small time step, W is adjusted by

$$W \to \frac{W}{1 + \lambda \Delta t_s}, \tag{4.64}$$

where

$$\lambda = \begin{cases} \alpha_d \sin^2\left[\frac{\pi}{2}\left(1 - \frac{z_{top} - z}{z_{sponge}}\right)\right] & \text{if } z \geq (z_{top} - z_{sponge}) \\ 0 & \text{if } z < (z_{top} - z_{sponge}) \end{cases}, \tag{4.65}$$

where α_d is the implicit damping coefficient, z_{top} is the height of the computational domain, and z_{sponge} is the height of the sponge layer. Implicit Rayleigh damping effectively absorbs gravity waves without the requirement of an initial state to relax back to, as done in traditional sponge layers. This is advantageous because it allows upper portions of the domain to evolve more freely. Setting α_d to 0.2 appears to be sufficient for preventing gravity waves from reflecting back down. The sponge layer is well above the tropopause, with a thickness that is approximately 20% the height of the computational domain. Additionally, W is set to zero at the upper boundary.

4.3 Initialization and Spin Up

The model is initialized with a sounding, shown in Fig. 4-5, that is neutral to undilute ascent of subcloud layer parcels. In this study, the sounding is derived from a surface parcel with an initial pressure of 1015 mb, an initial temperature of 28°C, and an initial relative humidity of 75%. The parcel is lifted such that it conserves s_p. In order

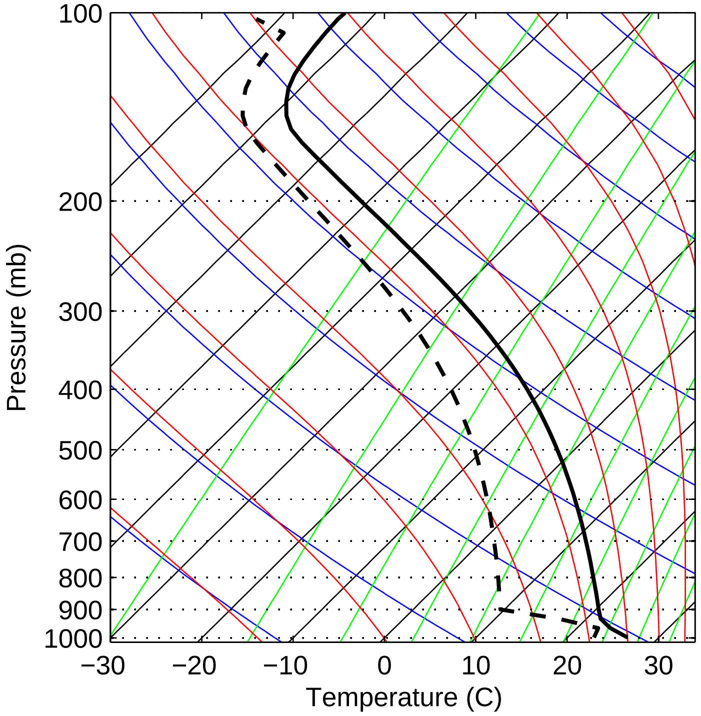

Figure 4-5: An initial, neutral sounding derived from a surface temperature of 28°C and surface relative humidity of 75%. The pseudoadiabats (red lines) are calculated using (4.19).

to have a tropopause and stratosphere, the Jordan mean hurricane season temperature profile is used above the height where the lifted parcel first becomes cooler than the Jordan sounding. The water vapor mixing ratio below the parcel's lifting condensation level is retained. Above the lifting condensation level, the relative humidity is set at 50% so that evaporation and downdrafts can occur.

A tropical-storm strength vortex is inserted into the domain, with a radial tangential wind profile from the parametric formula of Emanuel (2004). A maximum tangential wind of 20 m s^{-1} at a radius of 100 km is used, and the constants in the parametric formula are the default ones given in App. B of Emanuel et al. (2006). The vortex is assumed to decay with height as the square root of a quarter-cosine profile, such that the maximum tangential wind is initially at the surface and decays to zero at the tropopause.

The temperature and mass fields are then adjusted to be in thermal wind balance with the initial vortex following the anelastic approximation from Smith (2006). The anelastic form of the equation for gradient wind balance, given by

$$\frac{\partial \Pi}{\partial r} = \frac{1}{c_{pd}\overline{\theta_v}}\left(fv + \frac{v^2}{r}\right), \tag{4.66}$$

is integrated inward from the outer boundary in order to initialize the Exner function. $\overline{\theta_v}$ is the virtual potential temperature of the initial sounding and is only a function of height. Subsequently, θ_v is initialized to be in hydrostatic balance with the pressure field:

$$\theta_v = -\frac{g}{c_{pd}\frac{\partial \Pi}{\partial z}}. \tag{4.67}$$

The potential temperature and water vapor mixing ratio are then calculated such that the relative humidity and θ_v remain constant. Thereafter, s_p can be calculated from (4.18), and ρ_d can be calculated from the ideal gas law.

The TC is spun up from its initial state until it reaches a steady state, as shown in Fig. 4-6 at seven days. The maximum tangential winds are 67 m s^{-1} at a height of 1 km, with the radius of maximum winds sloping outward with height. In comparison, the theoretical potential intensity, which is calculated from an algorithm using the initial sounding and the model's surface exchange coefficients, is 85-93 m s^{-1}. It is important to emphasize that the *model's* potential intensity and the *theoretical* potential intensity are like two different species of the same genus. Differences between the two may arise due to differences in the model's definition of entropy with the exact pseudoadiabatic or reversible form. Additionally, the model intensity's sensitivity to resolution and the turbulence parameterization, particularly the horizontal mixing length (l_h), plays a role. One could possibly tune l_h in order to match the theoretical potential intensity more closely, but this would be ad-hoc. In lieu of any tuning, the model's potential intensity is treated as the baseline that will be used to compare to additional experiments.

The secondary circulation, outlined by the mass streamfunction in Fig. 4-6a, consists of 20-25 m s^{-1} inflow in the boundary layer just radially outward from the radius of maximum wind, 3-5 m s^{-1} vertical motion through the eyewall, and 15-20 m s^{-1} outflow around a height of 15 km. The waviness of the flow as it rises up the eyewall is indicative of an inertial oscillation caused by unbalanced flow. Additionally, the eyewall is characterized by slantwise neutrality, as indicated by the congruence of angular momentum, streamfunction, and entropy contours (not shown). At low levels, the entropy increases with decreasing radius. In the eyewall, there exists a column of high, nearly constant entropy. Much lower values of entropy are found at midlevels outside the eyewall, with the lowest values occurring at a height of 2-3 km. At this level, relatively dry air from aloft has subsided and cooled radiatively. Low-entropy air at midlevels does impinge a bit on the eyewall, especially as it begins to flare out above 5 km, causing evaporation and a downdraft of approximately 0.5-1 m s^{-1}. This downdraft is hinted at by the closed contour in the mass streamfunction just inside a radius of 50 km. However, the downdraft is too spatially limited and weak to have much of an effect on the TC energy budget. Elsewhere, there is shallow convection occurring outside the eyewall, but the general subsidence from the secondary circulation and lack of convective available potential energy inhibits deep convection from forming.

4.4 Spatially Fixed Ventilation Experiments

After the TC reaches a steady state, ventilation is introduced by adding a term to the turbulent entropy flux parameterization to reflect a fixed area of enhanced mixing:

$$F_r^{s_p} = \ldots - \mathcal{L}(r,z)\rho_d \nu_e \frac{\partial s_p}{\partial r}, \tag{4.68}$$

where $\mathcal{L}(r,z)$ is a localization function that limits the areal extent of the ventilation and ν_e is a fixed effective eddy viscosity. The localization function is chosen to be a piecewise linear function in radius, such that the enhanced mixing vanishes inside a radius of 20 km and outside a radius of 60 km and obtains a maximum value of unity at 30 km, just outside the initial radius of maximum wind. In the vertical direction, the localization function is a top hat function, such that the mixing is limited to a 2 km

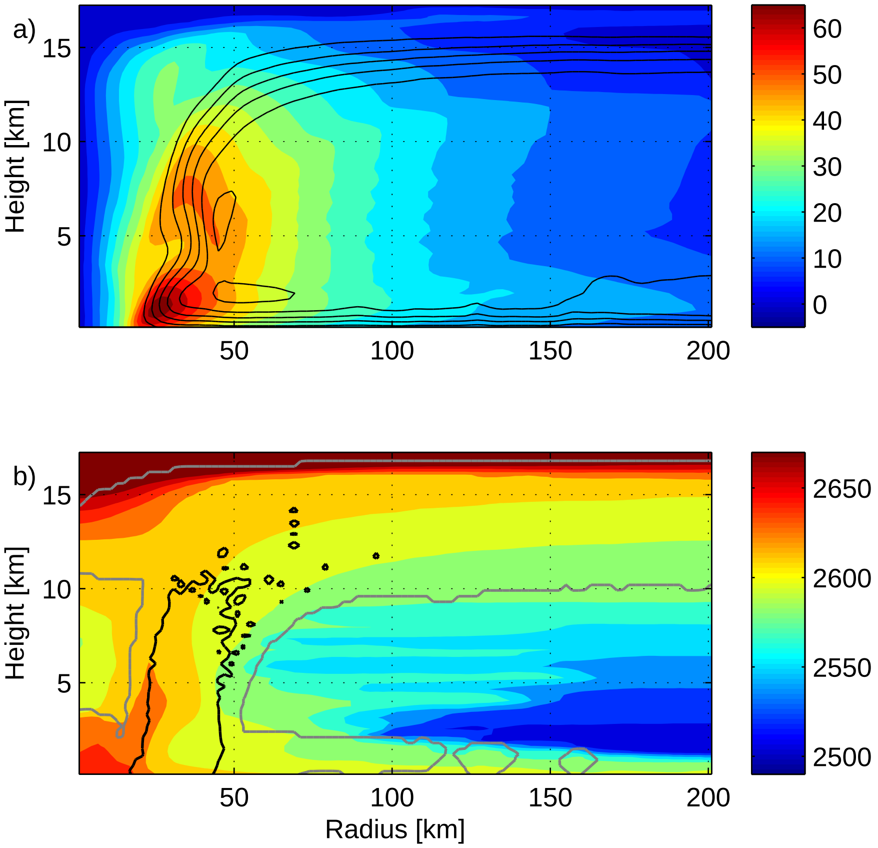

Figure 4-6: Radius-height section of (a) the tangential velocity (shaded in $\mathrm{m\,s^{-1}}$) and mass streamfunction (contoured in $\mathrm{kg\ s^{-1}}$) and (b) the pseudoadiabatic entropy (shaded in $\mathrm{J\ kg^{-1}\ K^{-1}}$) and liquid water mixing ratio (contoured) seven days after initialization. For the liquid water mixing ratio, the gray contour is $0\ \mathrm{g\ kg^{-1}}$ and the black contour is $1\ \mathrm{g\ kg^{-1}}$, which is the threshold for rain. Only the inner 200 km and the lowest 17 km are shown.

Table 4.1: Tropical cyclone ventilation experiments.

Experiment	ν_e (m^2 s^{-1})	Height (km)
Ctrl	0	NA
A01	1.0×10^4	3.0
A05	5.0×10^4	3.0
A10	1.0×10^5	3.0
A30	3.0×10^5	3.0
A50	5.0×10^5	3.0
H01	5.0×10^5	1.0
H03	5.0×10^5	3.0
H06	5.0×10^5	6.0
H09	5.0×10^5	9.0
H12	5.0×10^5	12.0
H15	5.0×10^5	15.0

vertical layer. The effective eddy viscosity accounts for the ability of mesoscale eddies, such as vortex Rossby waves, to transport tracers finite distances before diffusive effects cause irreversible mixing. Hendricks and Schubert (2009) found that breaking vortex Rossby waves are capable of mixing tracers across large horizontal distances, with effective eddy viscosities upwards of $O(10^4)$ m^2 s^{-1} for barotropic breakdown of vorticity rings.

A suite of experiments, listed in Tab. 4.1, is used to assess the TC's sensitivity to both the amplitude of the effective eddy viscosity and height of the ventilation.

4.4.1 Ventilation Amplitude

In the first set of experiments, the amplitude of the eddy viscosity is varied from 1.0×10^4 m^2 s^{-1} to 5.0×10^5 m^2 s^{-1}. The mixing occurs between a height of 2-4 km and is initially concentrated along the large radial entropy gradient of the eyewall's outer edge. Subsequently, the TC undergoes substantial intensity and structural changes if the ventilation is sufficiently strong.

Differences in the 24-48 hour averaged entropy and secondary circulation fields between the A50 and control experiments are shown in Fig. 4-7. The direct effect of the ventilation is to redistribute entropy within the bounds of the localization

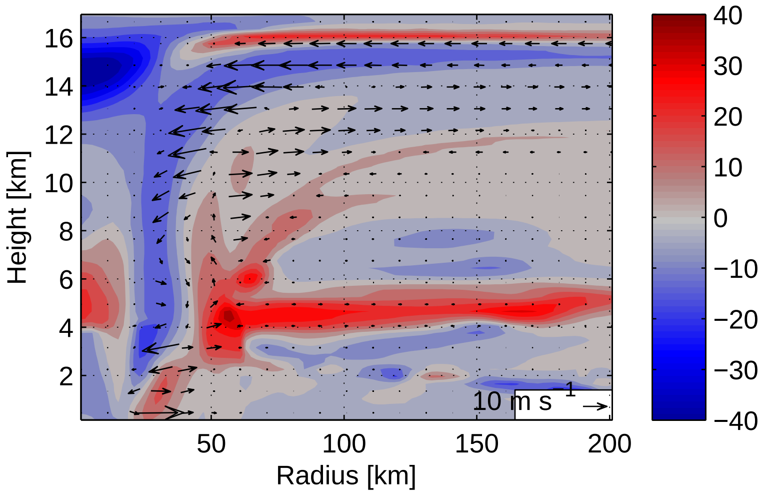

Figure 4-7: Differences in entropy (shaded in J kg^{-1} K^{-1}) and the secondary circulation (vectors in m s^{-1}) between the A50 and control experiments averaged over 24-48 hours.

function, such that there is a decrease in entropy in the eyewall and an increase in the near-inner core region at midlevels. Additionally, there are differences in entropy elsewhere including a decrease in entropy through a deep layer in the eyewall, a large decrease in entropy in the eye at upper levels associated with a degradation of the upper-level warm core, and an increase in entropy in a thin strip at a height of 16 km associated with a warming of the convective cold top (Holloway and Neelin, 2007). The vectors in Fig. 4-7 indicate differences in the secondary circulation of the TC between the A50 and control experiments. Flow in a counterclockwise direction indicates where the A50 experiment has a weaker secondary circulation, as seen in the boundary layer, through much of the original eyewall, and in the outflow layer above 14 km. On the contrary, flow in a clockwise direction indicates where the secondary circulation is stronger in the A50 experiment, as seen around a radius of 50 km flaring out to a height of 12-14 km. This pattern indicates a shift in the secondary circulation radially outward and vertically downward aloft. Difference plots for the other experiments show similar patterns, albeit to a lesser degree. Hence, strong localized mixing over a small region across the eyewall can induce system-wide changes in the TC's thermodynamic and kinematic structure.

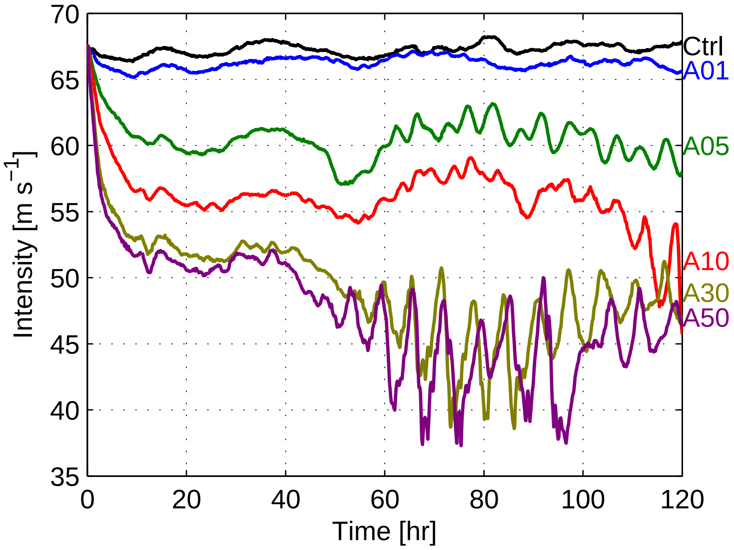

Figure 4-8: The maximum tangential winds ($\mathrm{m\,s^{-1}}$) in the 'A' ventilation experiments listed in Tab. 4.1.

As may be inferred from the structural changes, there is a corresponding decrease in TC intensity to increasing ventilation amplitude, as shown in Fig. 4-8. For the A01 experiment, the weakening of the maximum tangential winds compared to the control run is barely discernible, whereas the TCs in the A30 and A50 experiments weaken approximately 15 $\mathrm{m\,s^{-1}}$ in the first ten hours. Thereafter, there are two starkly different intensity regimes: a quasi-steady regime and an oscillatory regime. All the experiments are quasi-steady through about 40 hours. The A30 and A50 experiment then abruptly transition to a high frequency oscillatory regime, where the intensity rapidly changes by 5-12 $\mathrm{m\,s^{-1}}$ in a few hours. Furthermore, the mean intensity during the oscillatory regime is lower than the intensity during the quasi-steady regime.

Differences in the quasi-steady intensity can be explained by examining the fractional Carnot efficiency (η) of the inner core, defined by

$$\eta = \frac{\int \mathcal{D} \rho_d dV}{\int \frac{T - T_{ref}}{T} \left(F^{s_p}_{z=0} + \mathcal{D} \right) \rho_d dV}, \tag{4.69}$$

where $\mathcal{D}$ is the dissipation rate, T_{ref} is the state dependent reference temperature, and $F^{s_p}_{z=0}$ is the surface flux of entropy. The reference temperature for each point in the domain can be estimated by calculating each parcel's temperature at the level of neutral buoyancy in the sounding used to initialize the model. By construction, the neutral sounding has zero available potential energy and is thus the model's reference state. If considering only the fractional Carnot efficiency of the surface layer, the reference temperature becomes the outflow temperature, and the integrals in (4.69) are only calculated in the radial direction (cf. Emanuel (1997)). However, since interior dissipation and dissipative heating are not negligible when integrated over the entire free troposphere of the inner core, they are included for completeness.

For a perfect Carnot engine, η would be equal to one. This is approximately true in the eyewall of a TC at its potential intensity. However, when considering the fractional Carnot efficiency over the entire TC, the efficiency is much less than one. Surface fluxes and dissipative heating outside the inner core predominately go toward moistening and heating the environment. Hence, it is reasonable to expect that ventilation will cause a similar reduction in efficiency as available potential energy is used to moisten the inner core instead of powering the TC's winds.

The fractional Carnot efficiency of the innermost 60 km and lowermost 17 km averaged over 24-48 hours is shown in Fig. 4-9a for the 'A' ventilation experiments. For increasing ventilation amplitude, the efficiency monotonically decreases from 73% in the control run to 56% in the A50 experiment. Hence, an increasing fraction of the available potential energy generation goes in to moistening or heating the atmosphere in order to counter the effects of turbulent mixing due to ventilation. Fig. 4-9b shows the power lost due to entropy mixing, normalized by the control run's value, in the inner core above a height of 2 km. The power lost is composed of the direct contribution of ventilation via (4.68) and the model's turbulence parameterization. Both represent a sink of available potential energy, which can be estimated by integrating the product of the divergence of the turbulent entropy flux and the difference between the parcels' temperature and reference temperature (Pauluis, 2007):

$$\int (T - T_{ref}) D_{S_p} dV. \tag{4.70}$$

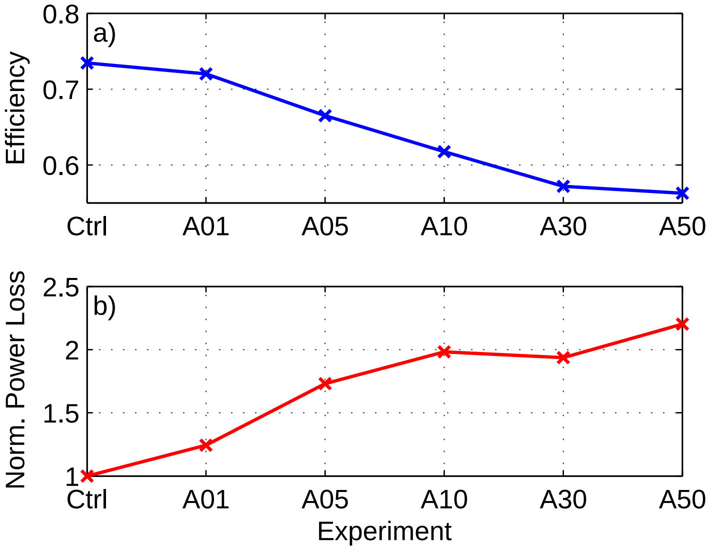

Figure 4-9: (a) Fractional Carnot efficiency for the 'A' ventilation experiments and (b) the normalized power loss due to turbulent entropy mixing above a height of 2 km. Both quantities are calculated for the innermost 60 km and averaged over 24-48 hours.

As the ventilation increases, the power loss due to diffusion of entropy increases steadily and becomes comparable to the power dissipated by friction. In the A10 experiment, the power loss due to turbulent entropy mixing is about twice that of the control experiment. In the A50 experiment, the power dissipated due to entropy mixing is about half the magnitude of the power dissipated by friction, which implies that a large percentage of the available potential energy generation from surface fluxes and dissipative heating in the inner core is being destroyed by turbulent entropy mixing above the boundary layer. This necessitates a lower fractional Carnot efficiency.

The fractional Carnot efficiency is related to the mechanical efficiency described by Pauluis and Held (2002). Tropical cyclones differ from other moist tropical circulations in that they are characterized by uncharacteristically high mechanical efficiencies that make the strong TC's winds possible. These high mechanical efficiencies are made possible by the TC's saturated inner core and resistance to radial intrusions of dry air (in the absence of asymmetric processes). Ventilation can be viewed as a hindrance to high mechanical efficiencies as an irreversible diffusion of water vapor leads to a reduction in the maximum work that can be achieved by the TC heat

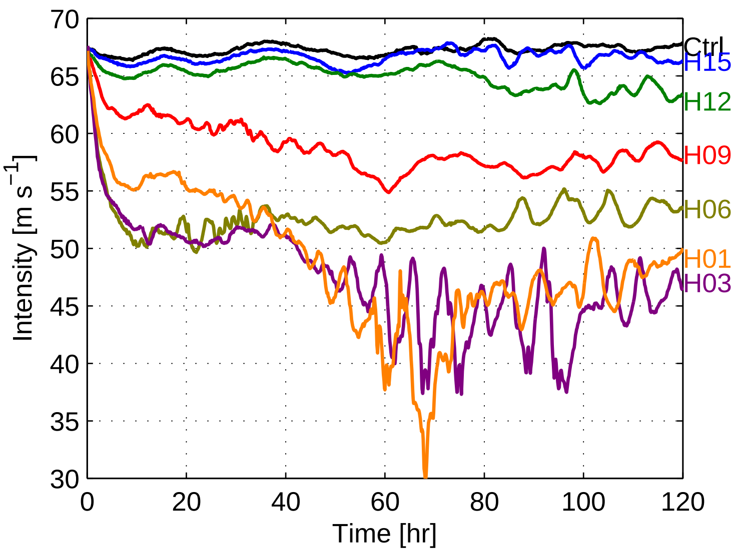

Figure 4-10: Maximum tangential winds (m s^{-1}) in the 'H' ventilation experiments listed in Tab. 4.1.

engine (Goody, 2003).

4.4.2 Ventilation Height

In the second set of experiments, the ventilation height is varied from 1 km to 15 km, while the amplitude is held at 5.0×10^5 m^2 s^{-1}. This set of experiments tests the weakening efficacy of ventilation located at various heights in the inner core. The TC intensity time series for these experiments are shown in Fig. 4-10.

Ventilation is most effective when it occurs at middle to low levels. Initially, the greatest weakening occurs for the H03 and H06 experiments, with notably less weakening occurring as the ventilation layer is moved upward. The H01 experiment weakens less in the first 24 hours compared to the H03 and H06 experiments, but continues to weaken and becomes approximately as weak as the H03 experiment after 40 hours. For upper-level ventilation (H12 and H15 experiments), the TC intensity shows very little difference from the control run. Hence, upper-level ventilation does not appear to be a mechanism that can substantially weaken a TC in this idealized setting.

The degree to which ventilation affects the TC is largely determined by the degree to which eddy mixing induces frontolysis in the eyewall entropy front. At midlevels, this potential is maximized because there exists a large low-entropy reservoir of relatively dry air in the near-inner core region that eddies can access. At upper-levels, the radial gradient of entropy is very weak reducing the ventilation potential. Moreover, ventilating the upper-level warm core does not result in a large hydrostatic pressure response due to compensating warming above the tropopause, which appears to be a balanced response to the eddy forcing. Thus, eddy kinetic energy can be very large at upper-levels, but has little to no avail in thermodynamically inducing weakening.

Thermal wind balance provides a simple way of explaining how changing the ventilation height affects the quasi-steady intensity. Combining the expressions for hydrostatic balance and gradient wind balance by cross differentiating and using the definition of the angular momentum, $M = rv + 0.5fr^2$, the thermal wind relationship is (Emanuel, 1986)

$$\frac{1}{r^3}\frac{\partial M^2}{\partial p}\bigg|_r = -\frac{\partial \alpha}{\partial r}\bigg|_p, \tag{4.71}$$

where α is the specific volume. Since α can be expressed as a function of s_p^* and p, using the Maxwell relationship,

$$\frac{\partial T}{\partial p}\bigg|_{s_p^*} = \frac{\partial \alpha}{\partial s_p^*}\bigg|_p, \tag{4.72}$$

results in (4.71) becoming

$$\frac{2M}{r^3}\frac{\partial r}{\partial p}\bigg|_M = \frac{\partial T}{\partial p}\bigg|_{s_p^*}\frac{\partial s_p^*}{\partial M}\bigg|_p. \tag{4.73}$$

An expression for the maximum tangential wind speed can be derived by integrating (4.73) down the angular momentum surface passing through the radius of maximum wind, r_m, at the top of the boundary layer, z_h. In order to arrive at a simple expression, the two layer system sketched in Fig. 4-11 is used. Assume the ventilation only occurs at a single level, z_e. Parcels rising through the eyewall from region I to region II are instantaneously mixed as they cross the ventilation

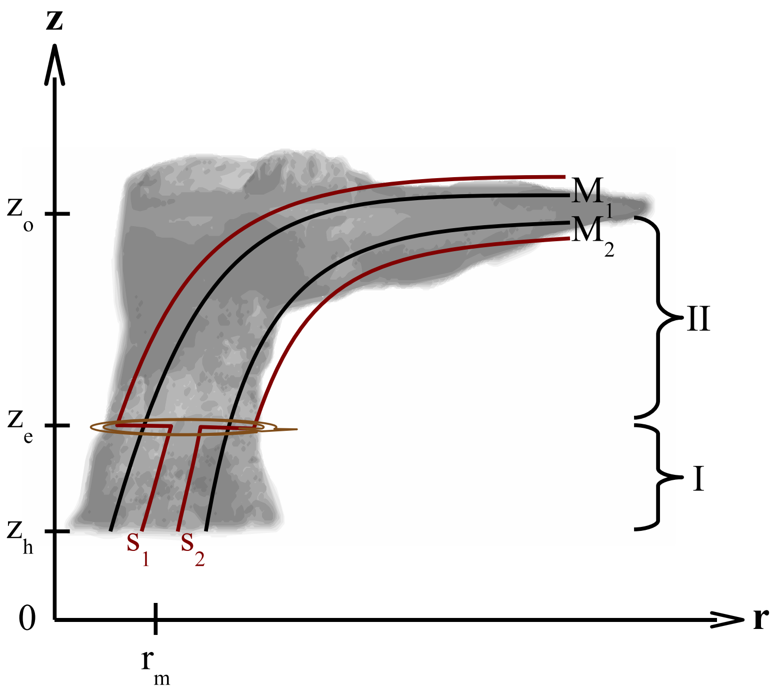

Figure 4-11: Schematic of the simplified model that is used to derive the ventilation modified thermal wind equation. The ventilation occurs at a single level, z_e. Region I, the layer below the ventilation, lies between the top of the boundary layer, z_h, and z_e. Region II, the layer above the ventilation, lies between z_e and the outflow layer, z_o. Two angular momentum surfaces ($M_1 < M_2$) and two saturation entropy surfaces ($s_1 > s_2$) are shown, where there is a jump in the entropy gradient across the ventilation level.

level resulting in an instantaneous reduction in the magnitude of the entropy gradient across the eyewall. Additionally, assume that neutrality holds above and below the ventilation level, such that angular momentum and saturation entropy surfaces are congruent to one another in each separate region. As a result, the gradient of saturation entropy with respect to angular momentum can be expressed as

$$\frac{\partial s_p^*}{\partial M} = c_I + \mathsf{H}(p_e - p)\underbrace{(c_{II} - c_I)}_{\Delta c}, \tag{4.74}$$

where c_I and c_{II} are the (constant) entropy gradients across the eyewall in region I and region II, $\mathsf{H}(p_e - p)$ is the Heaviside step function centered at the pressure of the ventilation level, p_e.

Under this set of assumptions, (4.73) can be integrated down the angular momentum surface passing through the radius of maximum wind in a piecewise manner:

$$M\left(-\frac{1}{r_m^2}+\frac{1}{r_o^2}\right)=\lim_{\delta\to 0}\int_{p_o}^{p_e-\delta}\left.\frac{\partial T}{\partial p}\right|_{s_p^*}\left(c_I+\Delta c\right)dp+\lim_{\delta\to 0}\int_{p_e+\delta}^{p_h}\left.\frac{\partial T}{\partial p}\right|_{s_p^*}c_I dp, \qquad (4.75)$$

where r_o is the outer radius, p_o is the pressure of the outflow level, and p_h is the pressure at the top of the boundary layer. Upon evaluating the integrals and assuming $r_o >> r_m$,

$$-\frac{M}{r_m^2}=\lim_{\delta\to 0}\left[\left(c_I+\Delta c\right)\left(T_{e-\delta}-T_o\right)+c_I\left(T_h-T_{e+\delta}\right)\right]. \qquad (4.76)$$

Furthermore, since $T_{e-\delta}\approx T_{e+\delta}$, (4.76) can be further simplified to

$$-\frac{M}{r_m^2}=c_I\left(T_h-T_o\right)+\Delta c\left(T_e-T_o\right). \qquad (4.77)$$

However, (4.77) does not take into account unbalanced effects that cause the tangential winds to be supergradient at the top of the boundary layer. Bryan and Rotunno (2009a) introduced a modification to the thermal wind relationship to account for unbalanced effects. Applying their modification and letting $M\approx rv$, (4.77) becomes

$$v_m^2=-M_m\left[c_I\left(T_h-T_o\right)+\Delta c\left(T_e-T_o\right)\right]+r_m\zeta_m w_m, \qquad (4.78)$$

where ζ is the relative vorticity. Any variable with a subscript 'm' is evaluated at the radius of maximum wind at the top of the boundary layer. The first term on the right hand side is the classical expression from Emanuel (1986), where the maximum tangential wind speed is proportional to the constant entropy gradient in the eyewall. The second term represents a correction due to ventilation. Increasing Δc, i.e. pulling entropy contours apart across the ventilation level, acts to decrease the magnitude of the term in brackets resulting in a decrease in v_m. Increasing the temperature at

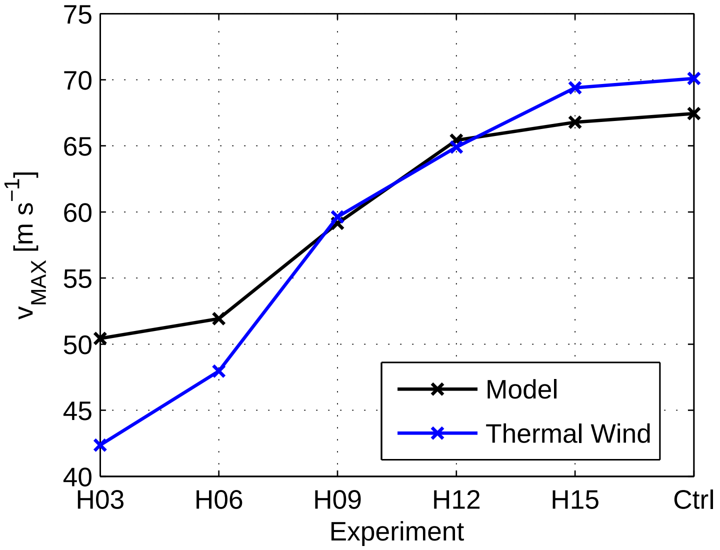

Figure 4-12: The maximum tangential wind speed (m s^{-1}) at a height of 1 km for the 'H' experiments (black) and the theoretical maximum tangential wind speed using a modified thermal wind equation in the eyewall (blue) averaged over 24-48 hours.

which ventilation occurs weights the second term more and also results in a decrease in v_m. Lastly, the final term on the right hand side is the contribution of unbalanced effects.

The theoretical maximum tangential wind speed at the top of the boundary layer in the 'H' ventilation experiments, save the H01 experiment since c_I is undefined, is calculated using (4.78). c_I and Δc are computed using the vertically averaged saturation entropy gradients evaluated along M_m above and below the ventilation layer. It should be kept in mind that M_m is a dynamic surface, such that the thermal wind calculation varies in both space and time. The theoretical maximum tangential wind along with the actual value at a height of 1 km both averaged over 24-48 hours is shown in Fig. 4-12. The modified thermal wind equation does quite well at estimating the model's maximum tangential wind speed, with a slight overestimation for the H15 and control experiments and a slight underestimation for the H03 and H06 experiments.

Due to the good agreement between the theoretical and actual v_m in Fig. 4-12, (4.78) can be used to explain the behavior of the 'H' experiments. Placing the ventilation at midlevels results in a large Δc, as very low entropy air is mixed into the eyewall resulting in a sharp jump in the entropy gradient across the ventilation layer. Moreover, $T_e - T_o$ is larger when the ventilation occurs lower in the eyewall, which increases the effect of the ventilation. The combination of these two effects results in a substantial decrease in the maximum tangential wind speed at the top of the boundary layer. As the storm weakens, a positive feedback results as c_I also decreases in magnitude due to weaker boundary layer inflow and surface fluxes both reducing the frontogenesis at lower levels. On the other hand, when the ventilation is moved upwards, the background radial entropy gradient weakens resulting in less of a jump in the entropy gradient across the ventilation layer. This is especially true when the ventilation is placed above 10 km, which explains why the H12 and H15 experiments differ little from the control experiment. Additionally, as T_e approaches T_o, the second term in (4.78) vanishes, and thus ventilation in the outflow layer has no bearing on the maximum tangential winds.

It should be noted that the fractional Carnot efficiency and thermal wind diagnostics lead to the same conclusions for both sets of sensitivity experiments. Increasing the amplitude of the effective eddy viscosity leads to a greater jump in Δc, which by the modified thermal wind equation corresponds to a decrease in the intensity. Moving the ventilation to upper levels results in a higher fractional Carnot efficiency because the power lost to entropy diffusion at upper levels is insignificant.

4.4.3 Oscillatory Intensity Regime

The quasi-steady intensity regime is described by the two diagnostics above fairly well since there aren't large time tendencies in the entropy or energy budget. Additionally, the eyewall remains predominately slantwise neutral. This is not true during the oscillatory regime in the A30 and A50 experiments, which is characterized by rapid shifts in the axisymmetric structure of the storm. Each oscillation in the intensity is governed by the life cycle of a convective burst. At first, strong mixing deposits high-entropy air into the near-inner core environment resulting in potential slantwise instability. Subsequently, elevated slantwise convection occurs, and precipitation falling from the convective burst evaporates in to the dry air below inducing an intense downdraft of 2-3 $\mathrm{m\,s^{-1}}$. The downdrafts transport a pocket of low-entropy air down into the boundary layer and induce compensating inflow through the middle troposphere resulting in an additional inward flux of low-entropy environmental air. The low-entropy air in the boundary layer is then swept inwards by the radial inflow, stabilizing the atmospheric column, and causing convection to temporarily cease until surface fluxes restore the boundary layer entropy. The process repeats itself with a period of about 5-8 hours.

The life cycle of several of these convective bursts from the A50 experiment is shown in the Hovmoller plot in Fig. 4-13a. The gray shading is the entropy at the lowest model level (z=150 m), while the cyan outlines denote significant downdraft entropy fluxes at a height of 1.5 km. Each downdraft transports a large amount low entropy into the boundary layer, which is then advected inward. Surface fluxes act to restore the entropy, but not completely before the downdraft modified air reaches the radius of maximum wind around 30 km. The result is a decrease in the radial entropy gradient through a deep layer in the eyewall. In response, the intensity decreases sharply, as seen by the dips in tangential wind speed after each downdraft event in Fig. 4-13b.

The cumulative effect of the downdrafts also decreases the mean intensity of the storm. Compared to a parallel A50 experiment, in which evaporation is turned off precluding downdraft formation, the A50 experiment is about 5-10 $\mathrm{m\,s^{-1}}$ weaker on average during the oscillatory regime. The downdrafts occur frequently enough to significantly affect the entropy budget of the inner core boundary layer and intensity of the storm, as hypothesized in Ch. 2 and by Riemer et al. (2010). Only after these large downdraft events cease after 100 hours does the TC begin to recover to a higher mean intensity.

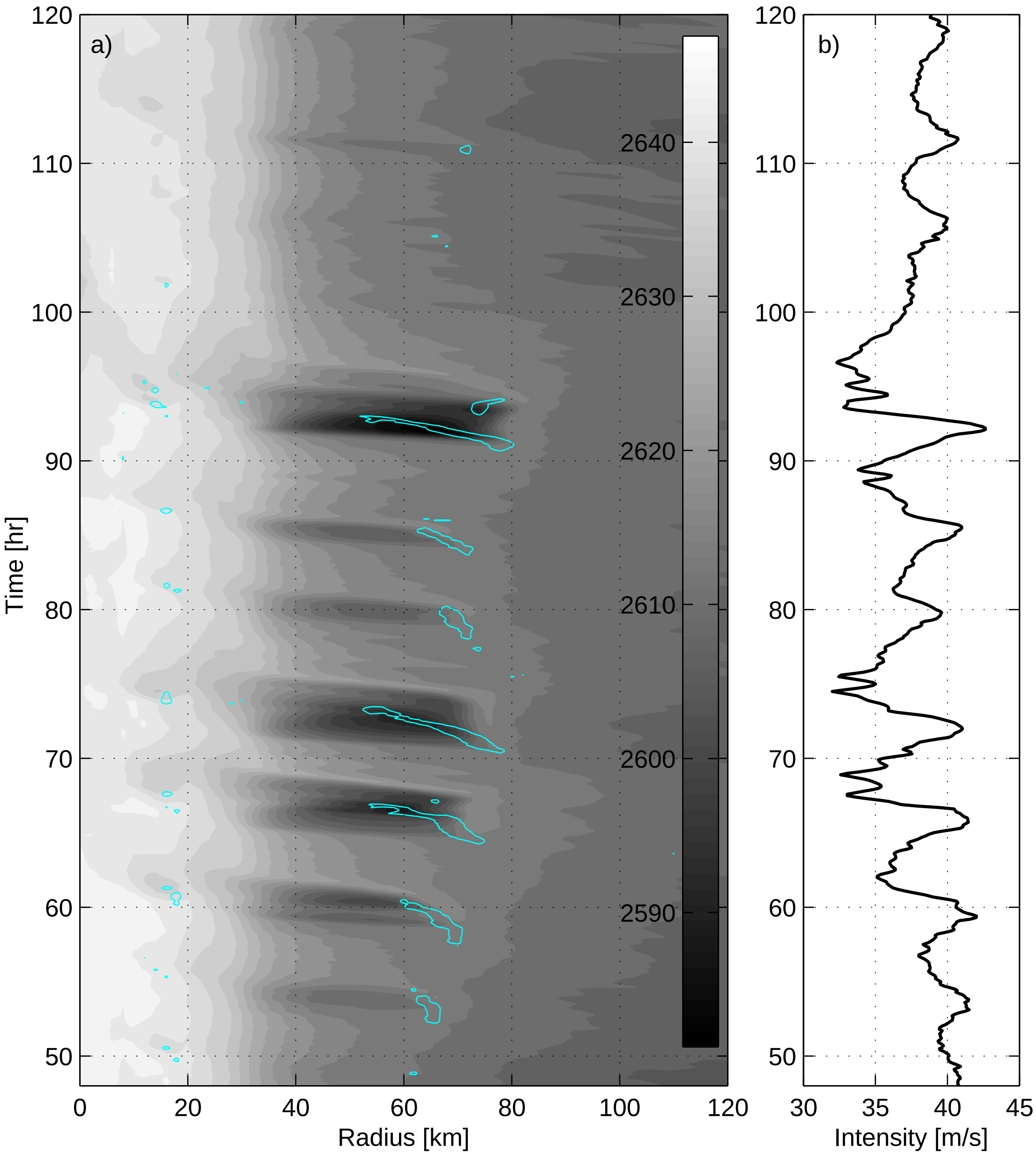

Figure 4-13: (a) Hovmoller plot of the entropy at the lowest model level (shaded in J kg^{-1} K^{-1}) and significant downdraft entropy fluxes at 1.5 km (cyan outline at -2 m s^{-1} J kg^{-1} K^{-1}), and (b) the time series of maximum tangential wind speed (m s^{-1}) at the lowest model level from the A50 experiment.

4.5 Spatially Varying Ventilation Experiments

In the previous experiments, the enhanced eddy entropy fluxes are fixed in space but vary in time. In the following experiments, the enhanced eddy entropy fluxes move with the radius of maximum wind but are constant in time. The maximum eddy entropy flux is specified to occur through the angular momentum surface (M_o) 10 km radially outward from the radius of maximum wind between height of 2 km to 6km. This angular momentum surface roughly demarcates the outer edge of the eyewall initially. The magnitude of the entropy flux at M_o is held constant between a value of 0 to 30 $\mathrm{J\,K^{-1}\,s^{-1}\,m^{-2}}$ and decreases linearly on either side, such that it vanishes at the radius of maximum wind and at the outer boundary of the domain. Although the entropy mixing is highly idealized and can even cause up gradient transport, this setup allows a much more controlled set of experiments that can be used to test the findings of Ch. 2.

The ventilation ($\mathcal{V}$) is calculated using the following formula from Ch. 2:

$$\mathcal{V} = \frac{1}{2\pi\rho_m r_m \delta r}\int_{M_o} \mathbf{F}^{s_p}\cdot \mathbf{n} d\xi \approx \frac{1}{\rho_m r_m \delta r}\int_{2\text{ km}}^{6\text{ km}} F_r^{s_p}\, r|_{M_o}\, dz, \tag{4.79}$$

where ρ_m is the density at the top of the boundary layer and radius of maximum wind, δr is a characteristic width of the eyewall, $\mathbf{n}$ is the unit normal vector along M_o, and $d\xi$ is a surface area element. The last step in (4.79) approximates the integral in cylindrical coordinates. δr is set to 20 km, which is the approximate width of the 1 $\mathrm{m\,s^{-1}}$ updraft region of the eyewall initially. An accurate estimate of (4.79) requires there to be a well defined r_m and M_o, which can be problematic if the storm becomes weak and disorganized. For those experiments in which the storm weakens rapidly, (4.79) is calculated in the 12 hours before rapid weakening commences.

The experiments are run out 10 days, and Fig. 4-14 shows the final 12 hour averaged maximum tangential winds and maximum gradient wind as a function of the ventilation. Additionally, the steady-state intensity curves from the theoretical framework are also plotted using the maximum gradient wind speed in the control experiment as the potential intensity and a ventilation threshold of 9.6 $\mathrm{m\,s^{-1}\,J\,(kg\,K)^{-1}}$.

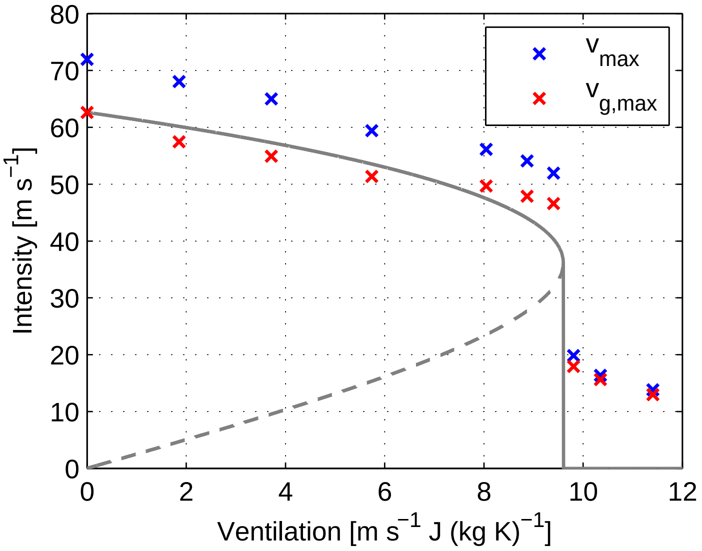

Figure 4-14: The maximum tangential wind (blue x's) and the maximum gradient wind (red x's) as a function of the ventilation for the spatially varying ventilation experiments. The theoretical steady-state intensity (see Ch. 2) most closely fitting the maximum gradient wind data is shown by the gray lines. The solid gray line denotes the stable equilibrium intensity, and the dashed gray line denotes the unstable equilibrium intensity.

The solid line is the stable equilibrium intensity and the dashed line is the unstable equilibrium intensity. In order to simplify the comparison with the theory, the ventilation threshold is held fixed for all experiments, although it should be remembered that the ventilation threshold is a function of the potential intensity and state-dependent storm structure.

The first postulate from the ventilation theory is that increasing ventilation causes a monotonic decrease in steady-state intensity. Clearly, this is also the case in the experiments for both the maximum tangential wind and gradient wind. The lowest four ventilation experiments appear to be quasi-steady. However, the three experiments between a ventilation of 8 and 9.5 m s^{-1} J (kg K)$^{-1}$ are still weakening at the end of the 10 day simulation, so it is likely that the intensities for these three experiments in Fig. 4-14 have not yet converged.

The second postulate is that there is a ventilation threshold beyond which only a weakening solution is possible. Once the ventilation exceeds 9.6 m s^{-1} J (kg K)$^{-1}$, the experiments have a precipitous drop in intensity indicating that a threshold has been crossed. The experiments above the ventilation threshold are very weak, and their structures are highly disorganized with no well defined radius of maximum wind and no coherent secondary circulation.

Absolute decay of the TC intensity is reasoned to be caused by downdrafts fluxing overwhelming quantities of low-entropy air into the boundary layer, such that the generation of available mechanical energy by surface fluxes is unable to sustain the TC's winds against both dissipation and downdrafts. To see whether this applies in the model, the surface entropy flux is compared to the downdraft entropy flux in the near-inner core region for the run with the largest ventilation around the time of rapid weakening. The downdraft entropy flux is defined as

$$\int W' \mathsf{H}(-W) s_p' r dr, \tag{4.80}$$

where the Heaviside function, $\mathsf{H}(-W)$, ensures only downdrafts are included in the integrand. The primes refer to perturbations from a slowly varying mean, which is determined by running a low-pass filter through W and s_p at each point in the domain. This is necessarily because the mean structure of the TC is changing during the period of interest and deriving the perturbation quantities form a strict time average would cause there to be an undesirable trend in the perturbations.

Fig. 4-15 shows the integrated downdraft entropy flux at a height of 1.5 km and the integrated surface entropy flux, where both quantities are evaluated over an annulus between 20 to 60 km. Before 140 hours, there is little downdraft activity and consequently little weakening due to the ventilation. After 140 hours, there is a slight increase in downdraft entropy fluxes before a very large downdraft event occurs around 150 hours. The downdraft entropy flux exceeds the surface entropy flux for a brief period of time, and concurrently, the intensity precipitously drops. Note that there is a temporary increase in surface fluxes despite the decrease in wind speed. This increase is a consequence of greater air-sea disequilibrium enhancing the surface fluxes, which mitigates the effects of downdrafts to a small degree. Another

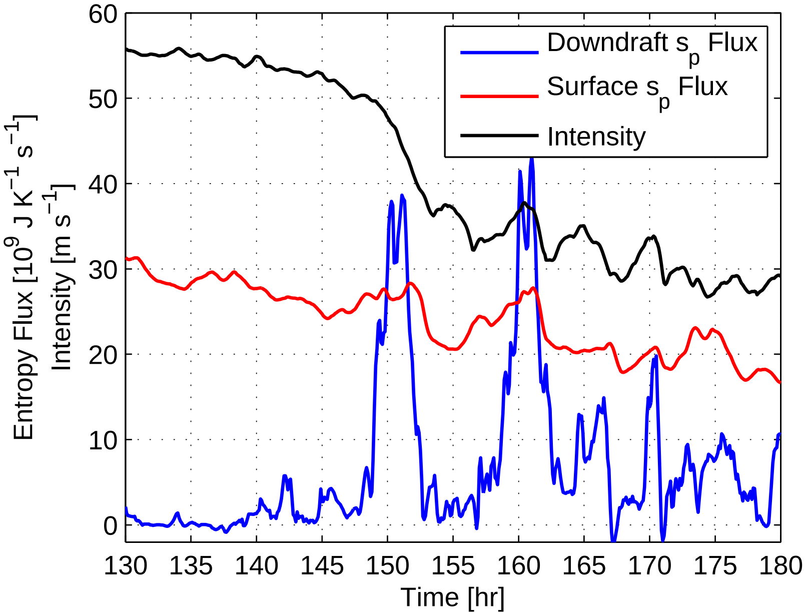

Figure 4-15: The downdraft entropy flux at a height of 1.5 km (blue line) and the surface entropy flux (red line) integrated over an annulus between 20 and 60 km over a period of rapid weakening for the experiment with the largest ventilation. Entropy fluxes are multiplied by 10^{-9}. The black line is the maximum tangential wind speed.

large downdraft event occurs around 160 hours followed by a succession of moderate downdraft events, with the greatest weakening lagging the downdraft events by a few hours. The elevated mean downdraft entropy flux through the period, coupled with a significant drop in surface fluxes, causes the TC to continuously decay.

Despite constant ventilation occurring above the boundary layer, the TC does not weaken until the ventilation is communicated down to the boundary layer via downdrafts, which can take a substantial amount of time to materialize in the idealized experiments. There is some diffusion of entropy across the eyewall in the spatially varying ventilation experiments, but since the ventilation is always radially outward of the radius of maximum wind, there is not nearly as much entropy mixing across the eyewall as in the spatially fixed ventilation experiments. Therefore, an important finding arises concerning the ability of ventilation to weaken the TC. If ventilation is not communicated across the entire eyewall, as to affect the radial entropy gradient over a deep layer, or communicated down to the boundary layer, where it can affect the energy budget in the TC's boundary layer, then ventilation only has a minor effect on the intensity. Additionally, a parallel simulation where evaporation is turned off shows no significant change in intensity from the control run, which illustrates the important role of downdraft modification of the boundary layer (Riemer et al., 2010).

The third postulate from the ventilation theory is that ventilation will affect TCs of varying initial intensities differently. This is due to the unstable equilibrium intensity branch, as illustrated in Fig. 4-14. TCs with initial intensities below the unstable branch will decay, while TCs with initial intensities above it will grow to the stable equilibrium intensity. In this set of experiments, the ventilation is initiated at different times during the intensification stage of the control run. The ventilation is set to a value of approximately 8 m s^{-1} J $(\text{kg K})^{-1}$ for all experiments, which corresponds to an unstable equilibrium intensity of 23 m s^{-1}. Fig. 4-16 shows the intensity time series from this suite of experiments. As predicted from the theory, the storm with an initial intensity of 20 m s^{-1} fails to strengthen. Downdrafts continuously plague the inner-core preventing the TC from spinning up. For all other initial intensities, the TC strengthens and converges to approximately the same intensity. However, the ventilation does increase the time it takes for the TC to strengthen, which is also a behavior noted in the theoretical framework. For example, the TC with an initial intensity of 30 m s^{-1} doesn't begin to rapidly strengthen until after 80 hours and takes about twice as long to reach its peak intensity compared to the control run.

4.6 Conclusions

One possible pathway by which environmental vertical wind shear constraints a TC's intensity is by ventilating the inner core of a TC with low-entropy environmental air. A few flavors of the ventilation hypothesis include: upper-level ventilation of the warm core (Frank and Ritchie, 2001; Kwon and Frank, 2008), midlevel ventilation of the eyewall (Simpson and Riehl, 1958; Cram et al., 2007), and downdraft modification of the boundary layer due to the ventilation of near-inner core convection (Powell, 1990; Riemer et al., 2010). A simple model is devised in order to assess the sensitivity

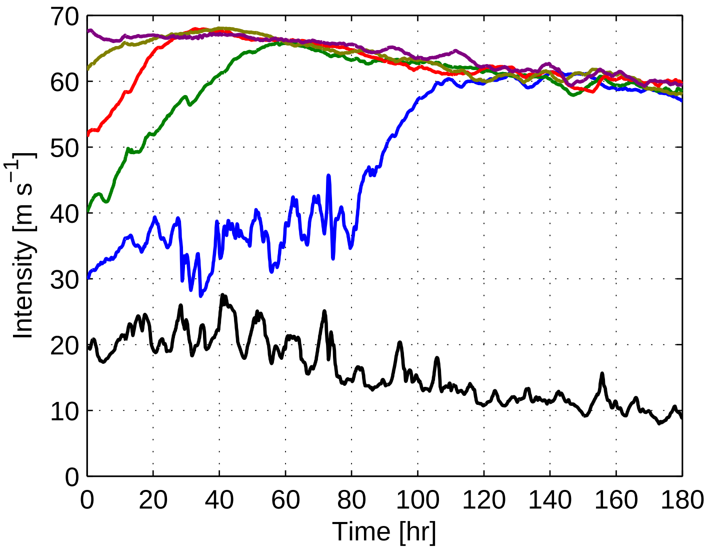

Figure 4-16: The maximum tangential winds for the set of experiments where the ventilation is initiated at different intensities.

of TC intensity to these possible ventilation pathways.

The model is based off the Rotunno and Emanuel (1987) model, but has some notable differences and improvements. Some of these differences include: a much more rigorously conserved mass budget, the use of pseudoadiabatic entropy as a prognostic variable, the use of an evaporation limiter that prevents excessive evaporation of rainwater, the inclusion of internal dissipative heating, and improved numerical methods.

Ventilation is prescribed in the model using a simple, down-gradient diffusive flux of entropy. Starting from a mature TC, ventilation is applied over a fixed area at midlevels across the eyewall with varying strength. For strong ventilation, there is significant cooling of the upper-level warm core and a shift in the secondary circulation radially outward. Additionally, strong ventilation quickly weakens the TC leading to a lower quasi-steady intensity, as the fractional Carnot efficiency is reduced in the inner core due to diffusion of entropy above the boundary layer. The weakening can also be viewed as a consequence of a reduction in mechanical efficiency due to irreversible mixing of entropy (Pauluis and Held, 2002; Goody, 2003). After a period of time, the simulations with strong ventilation transition into a oscillatory regime characterized by rapid swings in the intensity of up to 12 $\mathrm{m\,s^{-1}}$ with a period of 5-8 hours. These swings are shown to be associated with bursts of slantwise convection followed by a flux of low-entropy air down into the boundary layer by downdrafts. The cumulative effect of the downdrafts lowers the mean intensity further.

The sensitivity of the TC intensity to the ventilation height is also assessed. As the ventilation is moved upwards along the eyewall, the TC intensity decreases less. This behavior is explained using a modified thermal wind relationship. As the ventilation is moved upward, the jump in the radial entropy gradient across the ventilation layer decreases in magnitude resulting in less of an effect on the tangential wind speed at the top of the boundary layer. Furthermore, as the temperature difference between the ventilation layer and the outflow layer decreases, ventilation becomes less effective at inducing weakening. The greatest weakening occurs when the ventilation occurs at midlevels, where the entropy difference between the eyewall and environment is greatest and the temperature difference between the ventilation layer and outflow layer is also relatively large.

Based on these findings, ventilation at midlevels appears to be an efficient mechanism by which a reduction in maximum intensity can occur. Additionally, downdraft modification of the boundary layer is also effective at reducing the efficiency of the hurricane heat engine and weakening the storm. However, upper-level ventilation does not appear to be an effective weakening mechanism.

The key aspects of the theoretical formulation from Ch. 2 are also tested using the axisymmetric model with spatially varying, but constant entropy flux magnitude. Three components of the ventilation theory are supported: a monotonic reduction in intensity with increasing ventilation; the presence of a ventilation threshold, beyond which a TC cannot exist; and a bifurcation of TC intensity based on the strength of the initial vortex. An analysis of the entropy budget of the near-inner core region indicates that the TC rapidly weakens when the downdraft entropy flux becomes comparable to surface entropy fluxes, such that the mechanical energy generation by surface fluxes cannot maintain the TC's winds against both dissipation and downdrafts.

The setup of these experiments is highly idealized, as the complicated details of how eddy entropy mixing actually occurs have been avoided in this study. First, the ventilation parameterization does not reflect the possibility of non-local mixing, where entropy can be carried large distances before being irreversibly mixed at smaller scales. Second, the values of the eddy viscosities used are much higher than the effective viscosities determined by Hendricks and Schubert (2009). Third, the region that is ventilated is only loosely based on the stagnation radius for vortex Rossby waves, which is roughly 2-3 times the radius of maximum wind (Montgomery and Kallenbach, 1997; Corbosiero et al., 2006), versus some interactive calculation. Finally, the handling of microphysics in this model is quite simplified, and the details of evaporation and the melting of ice influence downdraft characteristics critically (Srivastava, 1987). Thus, there is uncertainty as to how much of the results carry over to 3D simulations or reality. At the very least, the results from these idealized experiments show the need to evaluate the upper-level ventilation hypothesis more carefully and provide a basis for investigations of ventilation in more complex models.

The efficacy to which shear-excited vortex Rossby waves are able to bring in low-entropy air into the inner core of the TC also needs to be studied in 3D models. The idealized experiments in this study show that having the low-entropy air simply get close to the inner core has little effect. To affect the energy budget of the TC and significantly weaken the storm, there must be substantial irreversible mixing of low-entropy environmental air with the high-entropy highway of the secondary circulation by either formation of downdrafts or direct mixing across the entire eyewall. Additional investigations of the behavior of vortex Rossby waves in moist, 3D models of vertically sheared TCs is critical to addressing this issue.

Chapter 5

Conclusions and Future Work

5.1 Summary of Work

Environmental vertical wind shear is observed to reduce the maximum intensity of tropical cyclones below the potential intensity, but the physical pathway by which this occurs is uncertain. One hypothesized pathway is midlevel ventilation - the flux of low-entropy air into the inner core of a tropical cyclone. The low-entropy air acts as “anti-fuel” disrupting the hurricane heat engine.

Two possible pathways are hypothesized by which ventilation occurs. The first pathway is direct injection of the low-entropy air into the TC’s eyewall leading to a decrease in the eyewall entropy through deep layer. The second pathway is convective downdraft fluxes of low-entropy air into the boundary layer by shear-induced asymmetric convection in the near-inner core region. Once the TC begins to weaken, a positive feedback can then occur where reduced surface fluxes allows ventilation to depress the entropy even further causing more weakening. The hypothesis is evaluated theoretically, observationally, and numerically.

The two ventilation pathways are investigated by modifying the axisymmetric, slantwise neutral, steady-state theory of Emanuel (1986) to account for ventilation. In this framework, eddy fluxes of entropy in the free troposphere are instantaneously communicated down to the boundary layer through convective downdrafts. Ventilation is noted to constrain the intensity in several ways. The difference between the potential intensity and the ventilation modified steady-state intensity is a monotonic increasing, nonlinear function of the ventilation. Furthermore, there exists minimum steady-state intensity of approximately 58% of the potential intensity at the ventilation threshold. Beyond the ventilation threshold, a steady tropical cyclone cannot be maintained, and only a trivial solution is possible (i.e. one with no tropical cyclone at all). For nonprohibitive magnitudes of ventilation, there is a dividing intensity separating growing and decaying TCs, implying that ventilation kills off weaker initial vortices. Experiments using an axisymmetric model with prescribed ventilation confirm these theoretical findings.

A secondary effect on intensity is caused by an increase in the outflow temperature. As ventilation increases, the buoyancy of the TC's eyewall relative to the background environment is reduced resulting in a shallowing of the storm structure, in agreement with composited analyses of vertically sheared TCs. This results in a reduction in the thermodynamic efficiency, which serves to compound the effects of ventilation.

The effect of ventilation on the TC's energy generation budget in the boundary layer is also examined. As ventilation increases, the net energy generation decreases quickly as downdrafts flush the boundary layer with greater amounts of low-entropy air. If the ventilation is strong enough, the net energy generation becomes negative in the downdraft region overwhelming surface fluxes, which have already been weakened due to a decrease in surface wind speed. This process represents the feedback responsible for the nonlinear behavior noted in the steady-state equilibrium solution. Once ventilation passes the threshold value, sources of mechanical energy cannot balance the sink due to dissipation and downdrafts. Additionally, the threshold value is lower for the first ventilation pathway compared to the second pathway. In the latter case, downdraft air is modified by surface fluxes along its trajectory in toward the radius of maximum wind.

Normalizing the steady-state intensity by the potential intensity and the ventilation by the ventilation threshold for each respective thermodynamic environment collapses the framework into a single curve that is invariant across all thermodynamic states. Thus, the normalized ventilation serves as a powerful metric for assessing whether ventilation plays a detectable role in current TC climatology and for evaluating possible changes in TC statistics in different climates. Based on the normalized ventilation, a ventilation index is defined as the product of the vertical wind shear and the nondimensional entropy deficit divided by the potential intensity. The ventilation index can be calculated from large-scale gridded analyses after a suitable filter is applied to remove TCs from the data.

The spatial and temporal distribution of the ventilation index is shown to be tied closely with global tropical cyclogenesis and normalized intensification statistics. The spatial distribution of tropical cyclogenesis is confined to regions of low seasonal ventilation index, which shares substantial overlap with the genesis potential index (Emanuel, 2010). On daily timescales, tropical cyclogenesis is most favored when the ventilation index is in the lower half of its climatological daily distribution in the global main genesis regions during the peak months of the hurricane season. Additionally, the maximum normalized intensity for TCs decreases with ventilation. The distribution of normalized intensification as a function of normalized ventilation indicates the possibility of a steady-state equilibrium intensity separating decaying and strengthening TCs. TCs located far from equilibrium tend to show greater normalized intensity changes. These findings provide observational evidence for the stable equilibrium solution from the theoretical framework.

The ventilation index can be used as a proxy to assess potential changes in TC climatology in GCM simulations between the late 20th and 22nd centuries. Overall, it is hard to draw any robust conclusions, as there is large variance among the GCMs, especially regionally. However, individual models do show large ventilation index changes, and any single realization indicates potential regional shifts in the preferred locations of tropical cyclogenesis and changes in TC intensity statistics. In every GCM examined, vertical wind shear changes only contribute to a portion of the ventilation changes. The nondimensional midlevel entropy deficit and potential intensity increase nearly everywhere in the tropics. Since the GCMs tend to show the nondimensional midlevel entropy deficit increasing faster than the potential intensity in most TC basins, the former alone will increase the mean ventilation even in the absence of any changes in the vertical wind shear.

Finally, the sensitivity of TC intensity to parameterized ventilation in an axisymmetric model is examined. The primary differences between the Rotunno and Emanuel (1987) model and the current model is that it uses pseudoadiabatic entropy as its prognostic variable and has much more rigorously conserved mass and entropy budgets, which make using integrated entropy diagnostics to evaluate intensity changes less prone to large residuals. Ventilation is imposed using a first order, down-gradient diffusive flux of entropy (and water vapor mixing ratio).

The TC generally weakens much more for larger ventilation amplitude and when the ventilation is located at midlevels near the largest radial entropy difference between the eyewall and environment. This behavior can be examined by diagnosing either the fractional Carnot efficiency of the inner core or thermal wind balance in the eyewall. The fractional Carnot efficiency decreases with increasing diffusion of entropy above the boundary layer. A modified thermal wind relationship shows that the greater the decrease in entropy gradient across the ventilation layer and/or the higher temperature at which ventilation occurs in the eyewall, the greater the decrease in the tangential wind speed at the top of the boundary layer. Both of these diagnostics indicate that midlevel ventilation has much more potential to weaken a TC than upper-level ventilation.

Additionally, downdraft modification of the boundary layer occurs in some of the experiments. Strong convective bursts lead to large downdrafts that flush the boundary layer with low-entropy air. As the low-entropy air is advected inwards by the radial inflow, convection quickly dies and the storm weakens dramatically. Energetically, the reason for this weakening can be seen by calculating the downdraft entropy flux at the top of the boundary layer and surface fluxes in the inner core. In agreement with the theoretical framework, when the downdraft entropy flux becomes comparable in magnitude to surface fluxes, the mechanical energy generation by surface fluxes in the inner core cannot maintain the TC's winds against dissipation. This results in rapid weakening of the storm.

In summary, the findings of the three chapters presented within this thesis support the ventilation hypothesis. Midlevel ventilation and downdraft modification of the boundary layer both appear to be viable ways by which environmental vertical wind shear can significantly affect TC intensity. This work lays the foundation for more detailed studies of the ventilation hypothesis in 3D numerical models of sheared TCs and upcoming field campaigns. Some ideas are proposed in the next section.

5.2 Future Work

5.2.1 Case Study: Hurricane Bill (2009)

A precise calculation of ventilation requires high resolution spatial and temporal data. An observational dataset does not exist to the author's knowledge that would allow such a calculation. However, there are some case studies that indicate the possibility that ventilation may be taking place. Once such example is Hurricane Claudette, which weakened from a hurricane to a weak tropical storm in about six hours (Shelton and Molinari, 2009). Inflow of dry air on the northwest side of the storm is hypothesized to have ventilated the eyewall leading to the hurricane's quick demise.

Another more recent case study is Hurricane Bill (2009). Hurricane Bill was studied as part of the Saharan Air Layer Experiment. The Saharan air layer is characterized as an elevated mixed layer with an associated midlevel jet and is hypothesized to inhibit tropical cyclogenesis and TC intensification, as it periodically sweeps across large portions of the tropical Atlantic (Dunion and Velden, 2004). The combination of dry air (low entropy) at midlevels along with increased shear makes TCs affected by the Saharan air layer prime candidates for collecting data to study the ventilation hypothesis.

Multiple missions were flown into Hurricane Bill on 8/20/09. From 8/20/09 at 03Z to 8/20/09 at 15Z, Bill weakened from 115 knots to 105 knots as the storm began to take on a more asymmetric appearance, and the eye began to look somewhat ragged. Thereafter, Bill held a quasi-steady intensity until more rapid weakening began later the following day. Total precipitable water analysis indicates that Bill was surrounding by two Saharan air layer masses to the east and west. A tongue of drier air can be seen wrapping in toward the center of the storm on 8/20/09 right around the time weakening begins (Jason Dunion, pers. communication). The deep layer vertical wind shear on 8/20/09, as estimated from the Cooperative Institute for Meteorological Satellite Studies, was from the SE at 6-7 $\mathrm{m\,s^{-1}}$ and increased to 8 $\mathrm{m\,s^{-1}}$ as the day progressed. Is it possible that the combination of vertical shear and dry air at midlevels halted the strengthening of Hurricane Bill and subsequently led to weakening thereafter?

Preliminary analysis from the Gulfstream-IV dropsonde data from 8/20/09 09Z to 14Z provides possible evidence for ventilation. Figure 5-1 shows the θ_e and radial wind in a frame of reference moving with the TC. The TC center and motion is deduced from a combination of vortex center fixes from a concurrent reconnaissance mission supplemented with best-track positions. Only data at and below 500 mb is shown in order to search for possible ventilation signals, namely, inflow coupled with negative entropy anomalies relative to the azimuthal mean. The azimuthal mean is a bit hard to deduce given the sparse data, but there does appear to be an area to the northeast of the center of anomalously low θ_e along with 7.5-10 $\mathrm{m\,s^{-1}}$ of relative inflow between 700-800 mb. At 700mb, the θ_e is especially low with values between 325-330 K. Total precipitable water analysis at 12Z indicates that the dropsondes likely sampled a piece of the Saharan air layer getting wrapped into the storm. Granted, these observations are about 200-300 km from the storm center and closer to an outer rainband than the inner core. It would interesting to see if this inflow of low-θ_e air extends closer into the inner core, possibly by examining the flight-level data from the other reconnaissance mission.

Shortly after the flight, a large band of arc clouds was observed to emanate from a rainband on the west and north sides of the circulation. The arc clouds are the visual manifestation of a large cold pool that had been generated by downdrafts along the rainband. The outflow from these cold pools appears to have been captured in Fig. 5-1 at 800 mb and below to the northwest of Bill's center. At 800 mb, there is one observation of 15 $\mathrm{m\,s^{-1}}$ radial outflow with a θ_e of 330-335 K. Lower down,

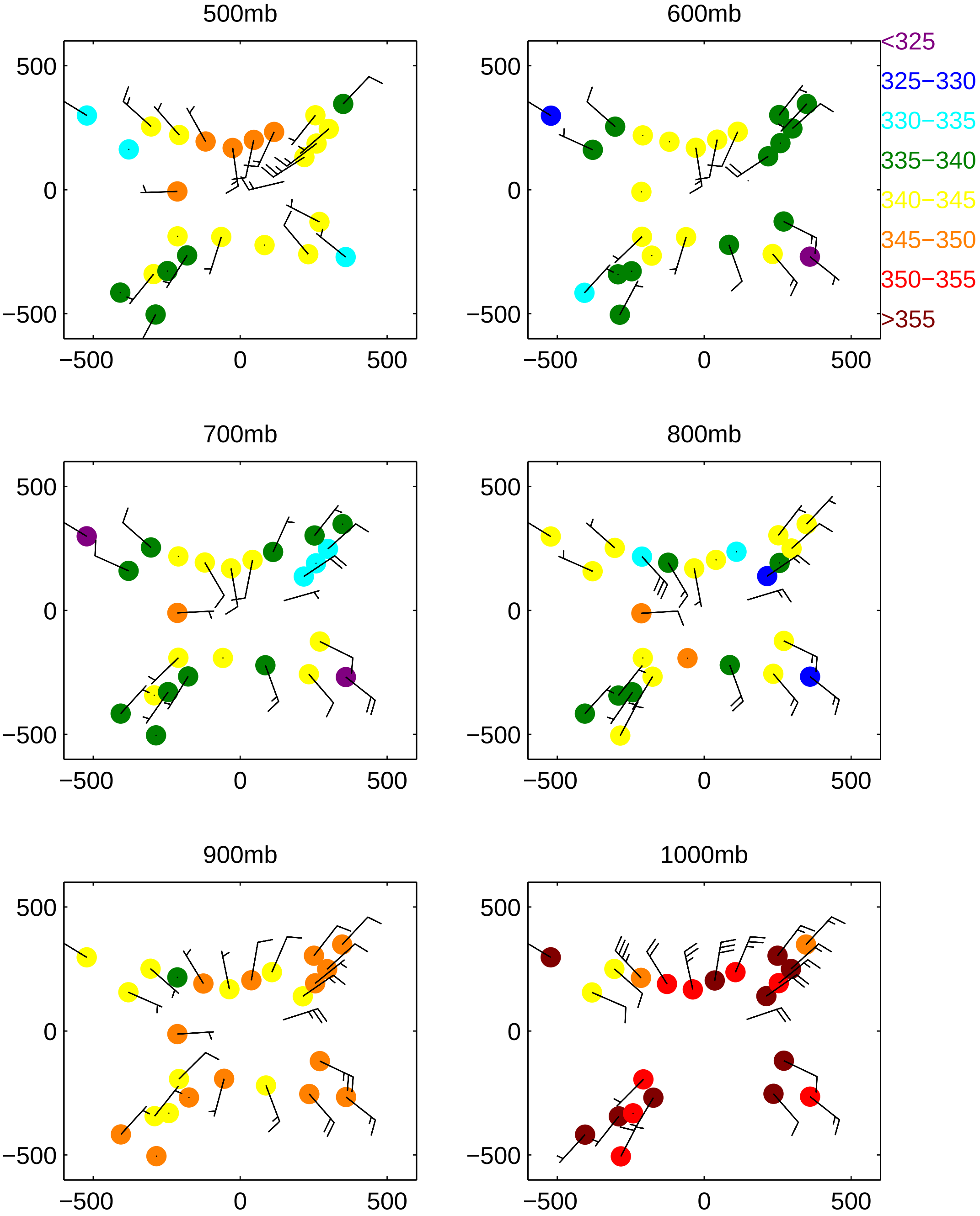

Figure 5-1: Dropsonde observations at 500, 600, 700, 800, 900, and 1000 mb from Hurricane Bill taken on 8/20/09 from 09-14Z. Colored dots indicate the value of θ_e (K), and wind barbs are the relative radial flow (m s^{-1}). The axes are the zonal and meridional distances (km) from the TC center.

there is weaker outflow coinciding with anomalously low θ_e values in the same region associated with a low-level cold pool propagating outward.

A vertical profile of the relative radial and tangential wind, the vertical wind, and the θ_e are given in Fig. 5-2 for the dropsonde that is about 170 km north of the TC's center. There are clearly strong downdrafts below 800 mb, which would flux the low-θ_e air observed above 950 mb downward. The profile of relative radial flow consists of inflow below 820 mb and weak outflow above. Hence, this dropsonde snapshot indicates at least the possibility of low-θ_e air being transported down into inflow layer of the storm, where it can then be advected toward the radius of maximum wind. However, the large downdraft in the northwest region of the storm appears to be dominated by outflow at low-levels, so it is unclear how much low-θ_e air is getting drawn in toward the center.

Obviously, there are many gaps in the data that would allow one to get a better sense of what's going on, but there are pieces of interesting evidence that appear to point to the possibility that midlevel ventilation and downdraft modification of the boundary layer affected the intensity of Hurricane Bill. It may be that the current observational platform is too limited to yield a more thorough dataset, but perhaps that will change in the near future with unmanned aerial vehicles and advances in dropsonde technology that will allow data to be collected in regions that are too risky to sample with conventional aircraft. Until then, there are probably a number of datasets that can be examined from past reconnaissance missions that may yield better evidence for ventilation.

5.2.2 Ventilation of Mature Tropical Cyclones in 3D Models

A set of 3D simulations for TCs embedded in varying amounts of vertical wind shear used by Riemer et al. (2010) serves as a good dataset for evaluating the assumptions and findings of the theoretical and axisymmetric modeling portions in this study. The first assumption used implicitly throughout this study is that a large low-entropy reservoir of air located at midlevels can be efficiently drawn close enough to the center of the TC to ventilate the inner core. First, the source of the low-entropy air

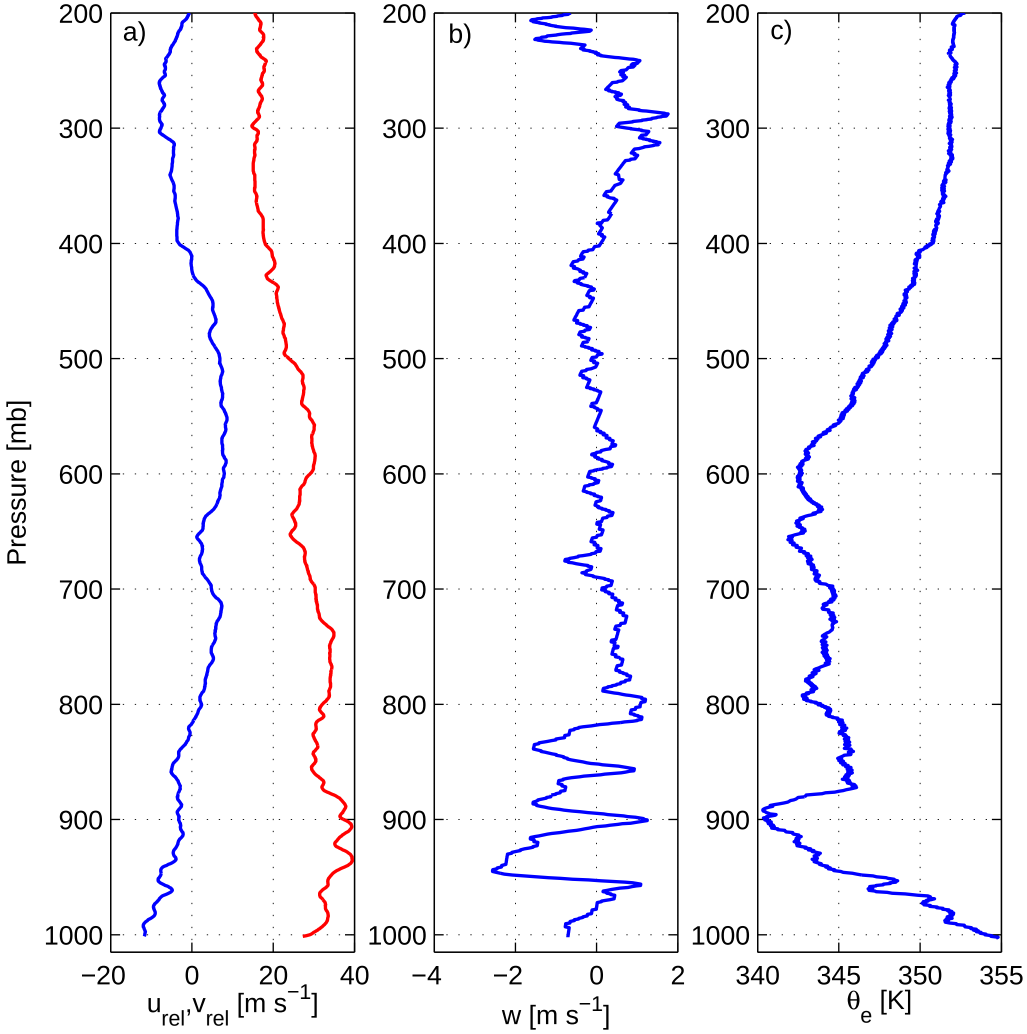

Figure 5-2: (a) A vertical sounding of the relative radial winds (blue line) and tangential winds (red line), (b) vertical velocity, (c) and equivalent potential temperature for a dropsonde released approximately 170 km north of the Hurricane Bill's center at 8/29/09 11:25Z.

must be determined. Cram et al. (2007) made progress on this front by looking at Lagrangian back trajectories of eyewall parcels. A back-of-the-envelope calculation performed in Ch. 2 using properties of their "class-IV" trajectories showed that the ventilation could indeed be responsible for limiting the intensity of the simulated storm. By performing a more careful calculation, examining additional cases for varying magnitudes of vertical wind shear, and also extending the trajectories further back in time, further insights in to the sources and effects of the low-entropy air will hopefully be obtained. Additionally, it would also be interesting to see the same back trajectory analysis performed for downdraft parcels to see if the air originating from cold pools originates from a different source than those parcels entering the eyewall directly. Second, the mechanism that is drawing in the low-entropy air must be identified. The standing hypothesis is that vortex Rossby waves are acting as the ventilation intermediary. It should be straightforward to evaluate the covariance of relative radial inflow and entropy, perhaps through an azimuthal wavenumber decomposition, to see if there are discernible patterns that emerge that would link vortex Rossby waves to the ventilation. Additionally, this would allow one to assess which sector(s) of the TC are preferentially ventilated.

Another major assumption in the theoretical framework is that there is an instantaneous communication between the lateral entropy flux in the free troposphere and convective flux through the top of the boundary layer in order to maintain strict equilibrium and steadiness in convectively active regions. However, the time tendency of entropy can be important, and there is likely a short lag between ventilation and the appearance of downdrafts. Moreover, the downdrafts may not extend down to the surface if the negative buoyancy generated by evaporation of rain is small. Using the 3D simulations, entropy budgets for select control volumes above the boundary layer (e.g. a half-annulus encompassing the upshear side of the eyewall) would be useful to assess the lag along with how efficiently low-entropy air is carried down into the boundary layer. However, a major challenge would be calculating such a budget with fidelity in a frame of reference moving with the TC. Additionally, it would be interesting to see if there is a feedback where acceleration of downdrafts into the boundary layer cause an unbalanced response that leads to even more low (or lower) entropy air being drawn inward to take its place.

The two diagnostics - modified thermal wind balance and fractional Carnot efficiency - that proved very useful in assessing the sensitivity of TC intensity to ventilation in the axisymmetric framework can also be applied in 3D simulations to see the extent to which they carry over. The azimuthal average of the gradient of entropy in the eyewall of the storm should scale with the azimuthally averaged tangential winds at the top of the boundary layer. Ventilation at midlevels should lead to a reduction in the entropy gradient with height, thereby affecting the intensity. The fractional Carnot efficiency or mechanical efficiency should be straightforward to apply since it can be easily calculated over the inner core of the storm. Diffusion of entropy (water vapor) due to ventilation should cause a decrease in the efficiency (Pauluis and Held, 2002) and reduce the rate of mechanical energy generation available to power the TC's winds.

Strong downdrafts are noted in the simulations in Riemer et al. (2010) and are hypothesized to have weakened the storm temporarily. Fig. 5-3 is a snapshot at 4.8 hours of the θ_e averaged through the lowest 1 km of the domain for the simulation with 15 $\mathrm{m\ s^{-1}}$ of easterly vertical wind shear. The large banded area of low entropy to the south is the product of a widespread area of persistent convective downdrafts. The streamlines indicate that the broad area of low-entropy air has to spiral about three-quarters of the way around before entering the eyewall. By the time this happens, enough time has passed to allow surface fluxes to substantially modify the downdraft air. This could be the reason why the TC's intensity does not weaken drastically even though there is a large area of low-entropy air lurking just outside the inner core. Of potentially greater significance are hints of undulations in the θ_e field in the eyewall from what appear to be pockets of low-entropy air produced by downdrafts very near the radius of maximum wind. One such downdraft is seen in Fig. 5-3 along the northeast edge of the eyewall. These downdraft parcels almost immediately enter the eyewall and, thus, have little time for modification by surface fluxes. Trajectories of inflowing parcels of air are needed to better assess how much of the low-θ_e downdraft

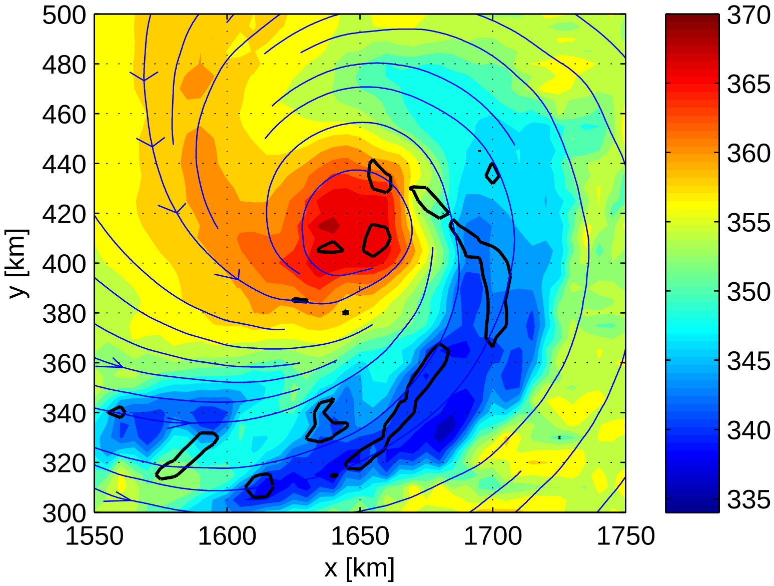

Figure 5-3: A 4.8 hour snapshot of the equivalent potential temperature (K) averaged over the lowest 1 km (shaded), streamlines of the average flow in the lowest 1 km (blue contours), and downdrafts at a height of 1 km with a magnitude greater than 1 m s^{-1} (black contour) for a 3D simulation of a TC embedded in 15 m s^{-1} of vertical wind shear. The data is courtesy Michael Riemer, Mike Montgomery, and Mel Nicholls.

air reaches the eyewall. An analysis of the θ_e along the trajectories would also give an indication of how quickly the θ_e recovers as it spirals inward.

The evolution of the downdraft convective available potential energy (DCAPE) (Emanuel, 1994) may be useful for determining the downdraft potential in sheared TCs. Dry air intrusions at midlevels would locally decrease the wet-bulb potential temperature and possibly increase the DCAPE. Although the DCAPE is not a conserved tracer, it may be useful for identifying the source region of the ventilation, much like CAPE is used to identify source regions of potential instability.

A secondary item of interest noted in the axisymmetric simulations is that downdrafts tend to follow slantwise paths. It would be interesting to see if this also applies in 3D models. This may be important because it would cause the cold pool to form slightly radially inward of the downdraft initiation radius and would thereby reduce the time it takes the low-entropy air to reach the eyewall, but it is unknown whether this effect is trivial. Perhaps "slantwise downdrafts" play a more important role when initiated very close to the radius of maximum wind where the surface fluxes are largest.

5.2.3 Ventilation Effects on Tropical Cyclogenesis

The role of environmental controls on tropical cyclogenesis is especially uncertain. Although there are a handful of large-scale conditions that serve as necessary conditions for tropical cyclogenesis, the role of mesoscale processes is much less understood. How a large-scale control, such as vertical wind shear, interacts with the mesoscale convective features of a nascent tropical disturbance and influences upscale growth is an interesting problem. In the context of the work presented here, how does ventilation affect tropical cyclogenesis? Even though the assumptions used to derive the ventilation framework do not apply well to the genesis phase, it was shown in Ch. 3 that ventilation still controls the spatial and temporal distribution of tropical cyclogenesis to a significant degree.

The Dunkerton et al. (2009) "marsupial paradigm" for tropical cyclogenesis postulates that the tropical wave's critical layer provides a protective pouch for convection to continuously moisten the troposphere, which has been hypothesized to be imperative for tropical cyclogenesis. However, the formation of a deep moist column is retarded by a preexisting dry airmass, vertical wind shear, or a combination of both.

The axisymmetric spinup of a TC in the axisymmetric model developed in Ch. 4 is delayed significantly if the relative humidity above the boundary layer is reduced to 25%. There are numerous bursts of convection, but each produces a convective downdraft that is followed by a quiescent period as the boundary layer "reloads." This occurs for approximately seven days until the inner core becomes moist enough to consolidate convection in to an eyewall. The storm then rapidly intensifies as the eyewall contracts inward. In contrast, if the relative humidity is set to 75% in the entire domain, the TC begins to rapidly intensify in about half the time.

A useful approach to assess the ventilation hypothesis is to calculate the moist entropy or moist static energy budget of the pouch using flight level and dropsonde data from the upcoming PRE-Depression Investigation of Cloud-systems in the Tropics field campaign. For instance, consider a hypothetical disturbance embedded in a dry Saharan air layer and vertical wind shear. Similar to the simulation using a dry initial sounding, evaporative cooling due to precipitation falling into the dry air leads to the formation of convective downdrafts that depress the entropy in the low levels of the critical layer, which suppresses further convection and delays genesis. The addition of vertical wind shear implies the existence of non-zero relative flow above and below the steering level of the tropical wave, which allows a continuous replenishment of relatively low-entropy air into the column to prime further downdrafts. As a result, there exists a periodic but significant entropy sink in the critical layer. However, vertical wind shear may not be completely inimical to tropical cyclogenesis since upward motion is enhanced on the downshear side of the vortex preferentially increasing convection and column moistening there. If the resulting increase in convection remains contained in the original pouch or there is a temporal shift in the pouch itself toward the convection, tropical cyclogenesis may be accelerated (Molinari et al., 2004; Musgrave et al., 2008).

In addition to the field campaign observations, high resolution model output can also be used to calculate the moist entropy budget. One approach is to assimilate the data gathered from the field into a mesoscale model using an ensemble Kalman filter or three-dimensional variational scheme. This would allow more careful diagnosis of the critical layer and entropy fluxes through the lateral boundaries. Another approach is to compare entropy budgets from a set of simulations using idealized initial environments, preferably for combinations of low, medium, or high vertical shear along with a dry or moist free troposphere.

It can be shown upon integrating the entropy equation over a control volume around the storm that the divergence of the entropy flux is related to a form of the gross moist stability, summarized in Raymond et al. (2009). A normalized form of the gross moist stability is used to assess the large-scale forcing of precipitation and spin up of tropical depressions (Raymond et al., 2007). As convection in a developing disturbance saturates the atmosphere and reduces the negative vertical gradient of entropy in the lower atmosphere, the normalized gross moist stability decreases. A lower gross moist stability allows surface fluxes to have a correspondingly larger influence on increasing precipitation and spinning up the TC. Ventilation would cause the opposite to happen by increasing the normalized gross moist stability.

Instead of normalizing the gross moist stability by the moisture flux, it may also be enlightening to normalize the gross moist stability by the surface entropy flux. This would yield a ratio of the large-scale entropy forcing to the in situ entropy generation, and would be very similar to the normalized ventilation derived in Ch. 2. Assessing changes in this form of the gross moist stability may be a convenient diagnostic for both TC intensity and tropical cyclogenesis studies.

An important operational implication of the proposed research is the degree to which a proper initialization of the environment around TCs is imperative for tropical cyclogenesis and TC intensity predictions. Thus far, the predominate focus of TC initialization or bogussing for numerical weather prediction has been on getting the kinematics of the vortex correct. However, if there are significant differences in simulated TC evolution due to changes in the near-TC environment in an idealized setting, then better observations and initialization of environmental vertical wind shear and moisture profiles will likely need to be a part of a comprehensive approach to improving tropical cyclone prediction.

Appendix A

Tropical Cyclone Filter

In order to diagnose the environmental flow in large-scale analyses or reanalyses, the flow associated with the TCs must first be removed. This is not a straightforward process since the TC is oftentimes poorly resolved and not in the same location as the best-track position.

TC bogusing schemes require the analyzed vortex to be extracted from the analysis in numerical weather prediction models. Some methods include an iterative three-point smoothing algorithm (Kurihara et al., 1993), inversion of Laplace's equation over the circle (DeMaria and Kaplan, 1999), and piecewise potential vorticity inversion (Wu and Emanuel, 1995). However, these methods all require the outer radius of the filter to be specified *a priori*. Additionally, Kurihara et al.'s method is applied barotropically despite the decay of the vortex with height. The goal is to develop a filter with variable outer radius that can be applied quickly to a large sample size of TCs. The first step is to objectively diagnose the outer radius of the TC as a function of height.

A.1 Filtering Function

In natural coordinates, the vertical component of the relative vorticity is defined as

$$\zeta = \frac{|\mathbf{u}|}{R_{curv}} + \frac{\partial \mathbf{u}}{\partial n} \qquad \text{(A.1)}$$

where $\mathbf{u}$ is the wind velocity, R_{curv} is the local radius of curvature of the streamfunction, and n is the direction normal to the flow. R_{curv} is positive for cyclonic flow and negative for anticyclonic flow. The radius of curvature in geocentric (longitude, latitude) coordinates is given by

$$R_{curv} = \frac{a\cos(\phi)(u_\psi^2 + v_\psi^2)^{3/2}}{u_\psi^2 \frac{\partial v_\psi}{\partial \lambda} - 2u_\psi v_\psi \frac{\partial u_\psi}{\partial \lambda} - \cos(\phi) v_\psi^2 \frac{\partial u_\psi}{\partial \phi}}, \tag{A.2}$$

where

$$u_\psi = -\frac{1}{a}\frac{\partial \psi}{\partial \phi}, \tag{A.3}$$

$$v_\psi = \frac{1}{a\cos(\phi)}\frac{\partial \psi}{\partial \lambda}, \tag{A.4}$$

and a is the radius of the Earth, ϕ is the latitude, λ is the longitude, and ψ is the streamfunction.

The basis of the filter is the first term on the right hand side of (A.1), which is simply the local angular velocity or curvature vorticity, ζ_{curv}. The curvature vorticity is positive definite wherever the flow is cyclonic, so it can be used to delineate the area of influence of the TC. However, to simply filter the winds based on some threshold of ζ_{curv} would be too broad, since other portions of the domain not associated with the TC's circulation can have positive ζ_{curv}. Examples of such scenarios include other nearby TCs and upper-level troughs, which contribute to the environmental vertical wind shear, and thus, should not to be filtered. To partially remedy this, ζ_{curv} is multiplied by a Gaussian localization factor in order to arrive at a filtering function, F:

$$F = \zeta_{curv} \exp\left[-\left(\frac{|\mathbf{x} - \mathbf{x}_{TC}|}{\sigma}\right)^2\right], \tag{A.5}$$

where the numerator of the exponent is the distance from the reanalysis TC center, $\mathbf{x}_{TC}$, and σ is the characteristic e-folding ζ_{curv} scale. After some experimentation, σ is set at a value of 675 km below 500 mb. Higher up, σ decreases linearly by 50 km per 100 mb above 500mb to reflect the baroclinicity of the TC. Although the radial extent of positive ζ_{curv} for most TCs decreases much faster with height, σ must be conservatively decreased to account for the small subset of intense TCs that have broad cyclonic circulations extending to upper levels. Small and ill-defined TCs in the reanalysis are mainly limited by ζ_{curv}.

The filtering function is calculated separately at each level in the reanalysis under the constraint that $\mathbf{x}_{TC}$ doesn't deviate by more than the 800 km from the 850 mb TC center. When this condition is violated, no filtering at that level occurs. The large tolerance is not meant to represent the possible range of the tilt of the vertical structure of the TC, but is rather chosen to prevent the algorithm from wandering to an unrelated local relative vorticity maximum.

Any u and v value at a grid point where F has a value greater than 5×10^{-7} is removed. This threshold value for F is arbitrary, but represents a reasonable value arrived at by trial and error. The filtering of the actual winds proceeds in a manner similar to the method used by DeMaria and Kaplan (1999). The process is summarized by the following set of equations:

$$u(\lambda, \phi) = \begin{cases} u & \text{where } F < 5 \times 10^{-7} \\ u_f & \text{where } F > 5 \times 10^{-7}, \end{cases} \tag{A.6}$$

where u_f, the filtered zonal winds, are found by inverting Laplace's equation,

$$\nabla^2 u_f = 0, \tag{A.7}$$

with Dirichlet boundary conditions,

$$u_f = u \quad \text{where } F = 5 \times 10^{-7} \ , \tag{A.8}$$

and similarly for v to get the complete filtered wind field. Note that the domain in which Laplace's equation is solved is almost always irregular.

A.2 Examples

Figures A-1 and A-2 illustrate two examples of the filter applied to the NCEP-NCAR reanalysis (Kalnay et al., 1996) 850 mb and 200 mb winds, respectively. The left columns represent Super Typhoon Chaba (2004), which is well defined in the reanalysis, and the right columns represent Hurricane Darby, which is much less well defined. The dashed line represents the boundary of the TC's area of influence as determined by the threshold value of F. The unfiltered fields are given in the top row, the filtered fields in the middle row, and the difference between the unfiltered and filtered winds in the bottom row. Chaba's cyclonic circulation at 850 mb is fairly well extracted, and even the weakly represented circulation associated with Darby is identified by the filter. At upper levels, the filter adjusts the filtering area to account for the decreased extent of the area of positive ζ_{curv}. For Darby, the filter doesn't alter the winds appreciably at 200 mb. In essence, the filter only removes what the reanalysis represents, whether it reflects reality or not.

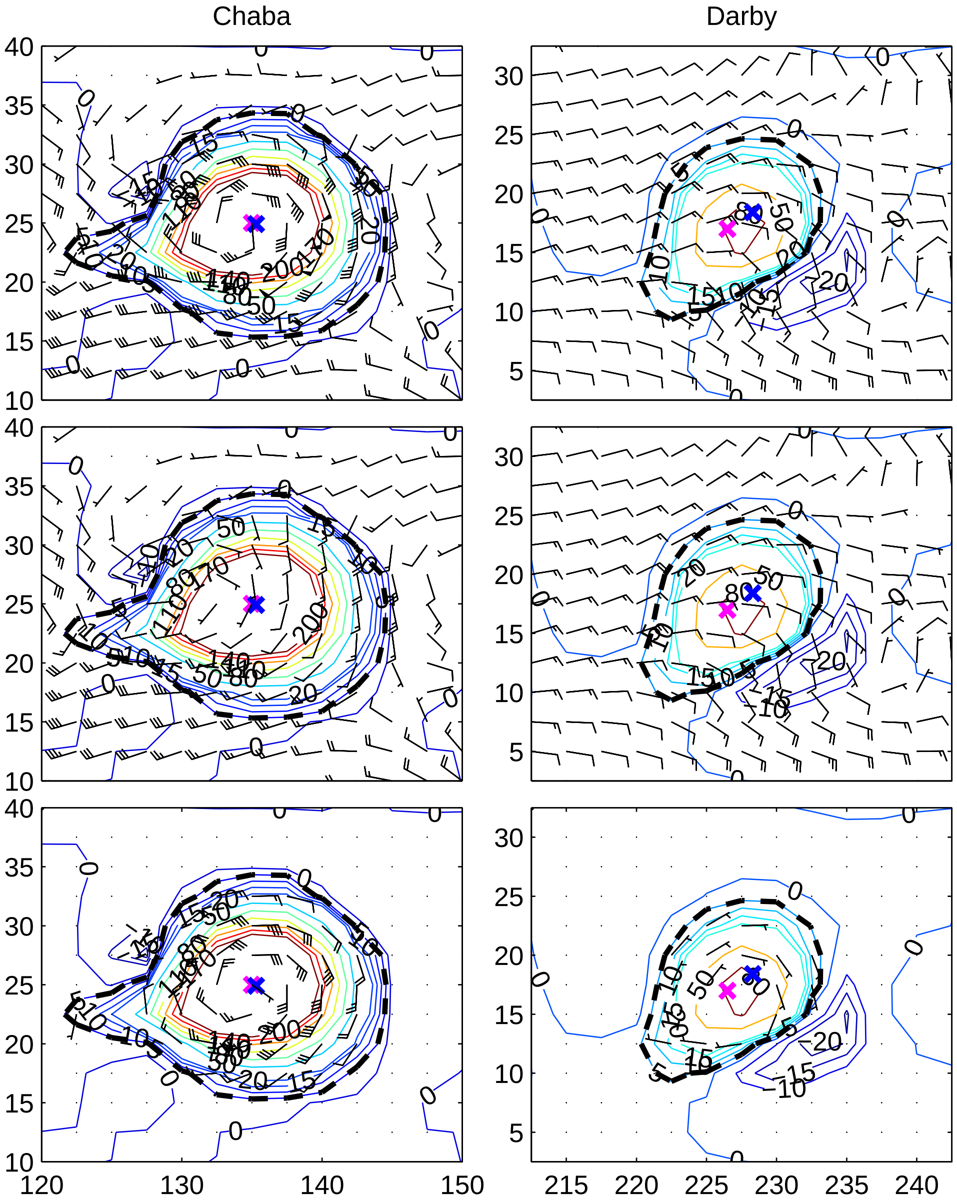

Figure A-1: The filtering algorithm applied at 850 mb for Super Typhoon Chaba (left column) and Hurricane Darby (right column). Color contours are the filtering function ($\times 10^7$ s^{-1}) and the dashed line is the threshold for the outer radius. The the top row is the unfiltered winds (knots), the middle row is the filtered winds, and the bottom row is the difference between the two. The magenta 'x' is the reanalysis TC center, as given by the maximum in the relative vorticity at the particular level, and the blue 'x' is the best-track TC center.

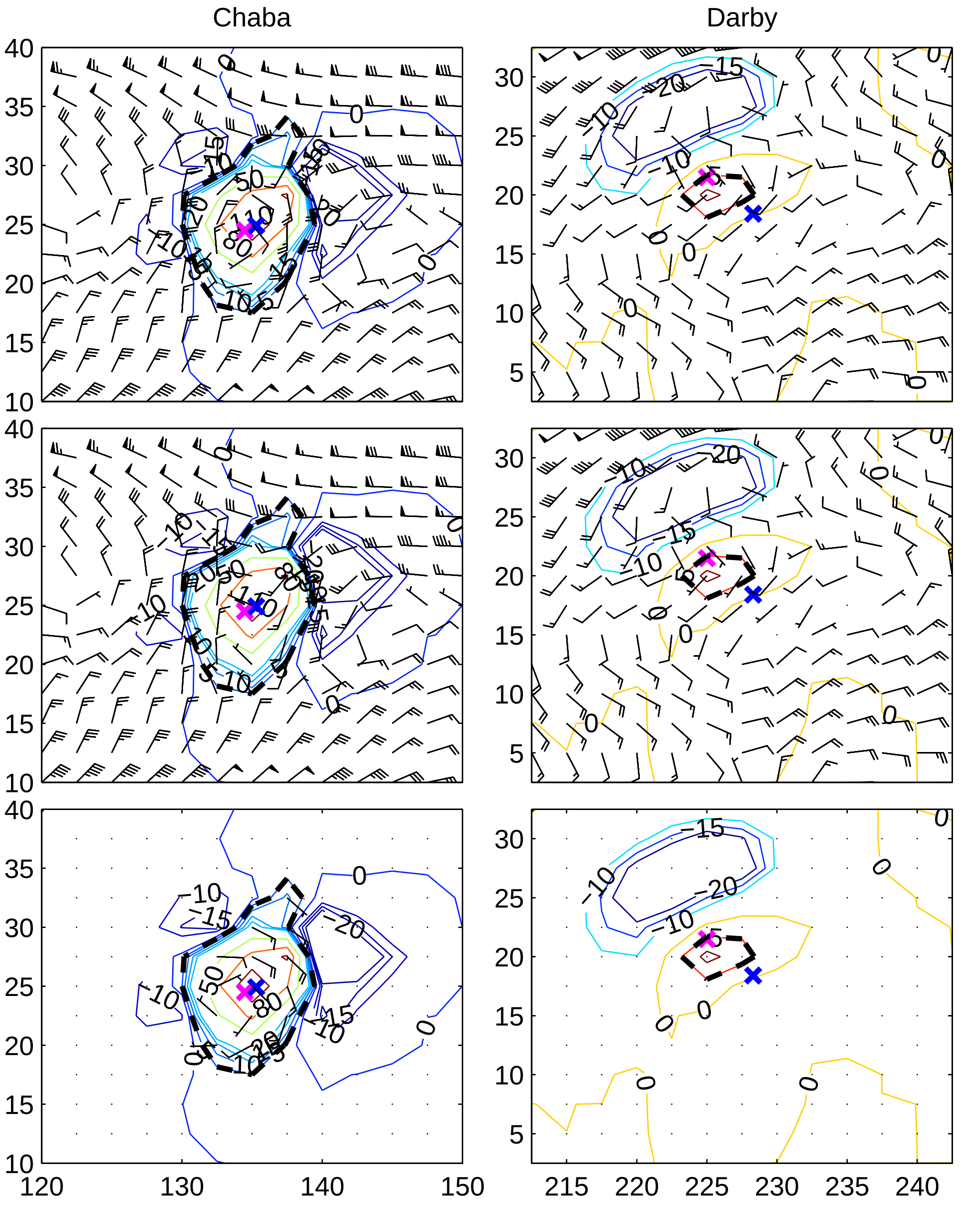

Figure A-2: Similar to Fig. A-1 except the filter is applied at 200 mb.

Appendix B

Outflow Temperature

Emanuel (1986) proposed a method for estimating the outflow temperature from a sounding by taking s_{min} to be the ambient boundary layer entropy and s_{max} to be the saturation entropy at the sea surface temperature. By lifting parcels with different entropies from s_{min} to s_{max} and calculating the temperature at their levels of neutral buoyancy, the outflow temperature $\overline{T_o}$, defined in (2.34), can be calculated.

In the ventilation framework, downdrafts can depress the sub-cloud layer entropy below the ambient value, reducing s_{min} while the entropy difference across the inner and outer regions can be used to determine s_{max}.

The change in entropy across both regions, given by (2.12), requires an expression for $\overline{\psi}$:

$$\psi = -\rho h r < u >, \tag{B.1}$$

and after using (2.18) in place of $< u >$ and averaging over the inner and outer regions,

$$\overline{\psi} \approx \rho C_D \left|\mathbf{u}_m\right| r_m^2 \left(\frac{1+\alpha^2\gamma}{2}\right). \tag{B.2}$$

Using (B.2) and the identity $\delta r / r_m = \alpha - 1$, (2.12) becomes

$$\delta s = -\frac{2(\alpha - 1)}{C_D \left|\mathbf{u}_m\right| (1 + \alpha^2 \gamma)} \Big\{ C_k \left|\mathbf{u}_m\right| \left[(1 + \alpha\gamma)(s^*_{SST} - s_a) - \Delta s\right] + \frac{C_D}{T_s}(1 + \alpha\gamma^3) \left|\mathbf{u}_m\right|^3 - \alpha\overline{w's'} \Big\}. \tag{B.3}$$

Given a sounding and sea surface temperature, equation (B.3) must be applied in an iterative manner as follows. As a first guess, s_{min} is set to the average entropy of the lowest 100 hPa of the sounding and s_{max} is set to s^*_{SST}. Then, an estimate of the outflow temperature can be calculated using (2.34) where T_o is the temperature at the level of neutral buoyancy. With the outflow temperature estimate, the steady state intensity is evaluated using (2.29), which can then be used to assess the entropy change across the outer region using (2.19) and the entire region using (B.3). If (2.19) is negative, then s_{min} is adjusted down to reflect the fact that downdrafts have lowered the entropy below s_a. Otherwise, s_{min} is unchanged. Likewise, (B.3) is used to adjust s_{max}, which should be greater than s_a. A new outflow temperature is calculated and the entire procedure is repeated until convergence occurs, usually in a few iterations.

A drawback of this method is that as α approaches 1, the entropy jump vanishes as the radial region over which fluxes act approaches a delta function. This precludes the ability of the algorithm to estimate the outflow temperature correctly and leads to an underestimate of the thermodynamic efficiency. It is recommended that $\alpha \geq 1.5$ when calculating the outflow temperature in order to avoid this deficiency.

Appendix C

Mass Sink in RE87 Model

The RE87 model is based off the Klemp and Wilhelmson (1978) 3D nonhydrostatic cloud model. In lieu of using the compressible continuity equation directly, a pressure equation is derived by taking the total derivative of the Exner function, defined by (4.9).

Subsequently, a truncation of the full pressure equation is taken that is consistent with the anelastic continuity equation (see (2.7) in Klemp and Wilhelmson (1978)). Justification for this approximation was given by comparing convective storm simulations using both the truncated and untruncated forms of the pressure equation in the Klemp and Wilhelmson (1978) model. The primary effect of the truncated pressure equation only appeared to be a constant offset in surface pressure, with little effect on convective storm characteristics.

The same approximation is carried forward in the RE87 model, but a key feature of TCs makes using the truncated pressure equation a poor choice. The key term in the truncated portion of the pressure equation is the total derivative of virtual potential temperature, θ_v, which includes diabatic heating. When this truncated term is large, it is equivalent to having large residuals in the continuity equation (Klemp et al., 2007). In a TC, the eyewall is a region of continuous and strong diabatic heating. This leads to a very large, persistent mass sink in the eyewall region, as shown in Fig. C-1 where the minimum mass budget residual is less than -2 kg m^{-3} s^{-1}! Consequently, there is not only a large pressure drift in the model due

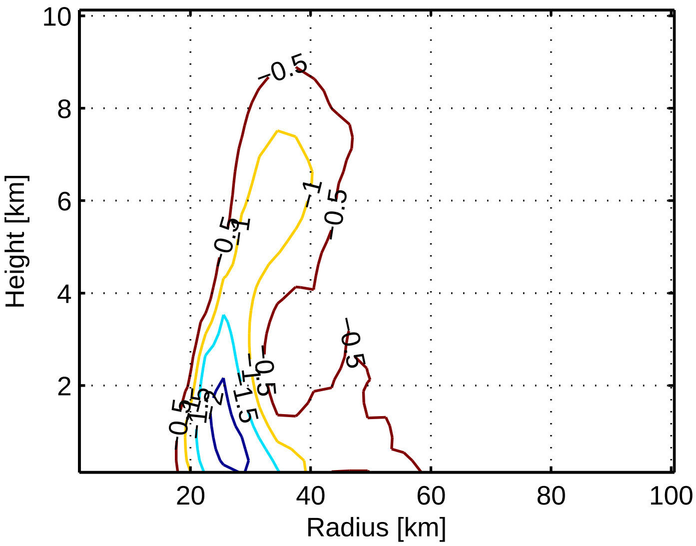

Figure C-1: The mass budget residual ($\mathrm{kg\,m^{-3}\,s^{-1}}$) averaged over 12 hours for a mature TC in the RE87 model.

to this persistent mass sink, but the budget of every extensive variable is affected. For example, the vertically integrated entropy flux at a radius outside the eyewall is negative due to enhanced inflow at lower levels and reduced outflow at upper levels. This is opposite of what is expected in steady, intense TCs, which should have a net export of entropy from the inner core.

A simple workaround is to add the advection of θ_v back in to the pressure equation. This reduces the mass sink in the eyewall by a substantial fraction and makes the TC entropy export the proper sign. However, there still remains a large enough residual such that accurate entropy or energy budgets are still difficult to achieve. In light of this, the compressible continuity equation is used directly in the current model.

Bibliography

Arakawa, A. and V. Lamb, 1977: Computational design of the basic dynamical process of the UCLA general circulation model. *Methods in Computational Physics*, Academic Press, Vol. 17, 173–265.

Bender, M., 1997: The effect of relative flow on the asymmetric structure in the interior of hurricanes. *J. Atmos. Sci.*, **54**, 703–724.

Bender, M., T. Knutson, R. Tuleya, J. Sirutis, G. Vecchi, S. Garner, and I. Held, 2010: Modeled impact of anthropogenic warming on the frequency of intense Atlantic hurricanes. *Science*, 454–458.

Bengtsson, L., M. Botzet, and M. Esch, 1996: Will greenhouse gas-induced warming over the next 50 years lead to higher frequency and greater intensity of hurricanes? *Tellus*, **48A**, 57–73.

Bengtsson, L., K. Hodges, M. Esch, N. Keenlyside, L. Kornblueh, J. Luo, and T. Yamagata, 2007: How may tropical cyclones change in a warmer climate? *Tellus*, **59A**, 539–561.

Bister, M. and K. Emanuel, 1997: The genesis of Hurricane Guillermo: TEXMEX analyses and a modeling study. *Mon. Wea. Rev.*, **125**, 2662–2682.

Bister, M. and K. Emanuel, 1998: Dissipative heating and hurricane intensity. *Meteor. Atmos. Phys.*, **65**, 233–240.

Black, M., J. Gamache, F. Marks, C. Samsury, and H. Willoughby, 2002: Eastern Pacific Hurricanes Jimena of 1991 and Olivia of 1994: The effect of vertical shear on structure and intensity. *Mon. Wea. Rev.*, **130**, 2291–2312.

Black, P., et al., 2007: Air-sea exchange in hurricanes: Synthesis of observations from the Coupled Boundary Layer Air-Sea Transfer experiment. *Bull. Amer. Meteor. Soc.*, **88**, 357–374.

Bolton, D., 1980: The computation of equivalent potential temperature. *Mon. Wea. Rev.*, **108**, 1046–1053.

Bracken, W. and L. Bosart, 2000: The role of synoptic-scale flow during tropical cyclogenesis over the North Atlantic Ocean. *Mon. Wea. Rev.*, **128**, 353–376.

Bryan, G., 2008: On the computation of pseudoadiabatic entropy and equivalent potential temperature. *Mon. Wea. Rev.*, **136**, 5239–5245.

Bryan, G. and J. Fritsch, 2004: A reevaluation of ice-liquid water potential temperature. *Mon. Wea. Rev.*, **132**, 2421–2431.

Bryan, G. and R. Rotunno, 2009a: Evaluation of an analytical model for the maximum intensity of tropical cyclones. *J. Atmos. Sci.*, **66**, 3042–3060.

Bryan, G. and R. Rotunno, 2009b: The maximum intensity of tropical cyclones in axisymmetric numerical model simulations. *Mon. Wea. Rev.*, **137**, 1770–1789.

Camargo, S., A. Sobel, A. Barnston, and K. Emanuel, 2007: Tropical cyclone genesis potential index in climate models. *Tellus*, **59A**, 428–443.

Caron, L. and C. Jones, 2008: Analysing present, past and future tropical cyclone activity as inferred from an ensemble of coupled global climate models. *Tellus*, **60A**, 80–96.

Chan, J., 2005: The physics of tropical cyclone motion. *Ann. Rev. Fluid Mech.*, **37**, 99–128.

Chen, Y., G. Brunet, and M. Yau, 2003: Spiral bands in a simulated hurricane. Part II: Wave activity diagnostics. *J. Atmos. Sci.*, **60**, 1239–1256.

Corbosiero, K. and J. Molinari, 2002: The effects of vertical wind shear on the distribution of convection in tropical cyclones. *Mon. Wea. Rev.*, **130**, 2110–2123.

Corbosiero, K., J. Molinari, A. Aiyyer, and M. Black, 2006: The structure and evolution of Hurricane Elena (1985). Part II: Convective asymmetries and evidence for vortex Rossby waves. *Mon. Wea. Rev.*, **134**, 3073–3091.

Cram, T., J. Persing, M. Montgomery, and S. Braun, 2007: A Lagrangian trajectory view on transport and mixing processes between the eye, eyewall, and environment using a high-resolution simulation of Hurricane Bonnie (1998). *J. Atmos. Sci.*, **64**, 1835–1856.

Davies-Jones, R., 2009: On formulas for equivalent potential temperature. *Mon. Wea. Rev.*, **137**, 3137–3148.

Davis, C. and L. Bosart, 2003: Baroclinically induced tropical cyclogenesis. *Mon. Wea. Rev.*, **131**, 2730–2747.

Delworth, T. and M. Mann, 2000: Observed and simulated multidecadal variability in the Northern Hemisphere. *Clim. Dyn.*, **16**, 661–676.

DeMaria, M., 1996: The effect of vertical shear on tropical cyclone intensity change. *J. Atmos. Sci.*, **53**, 2076–2087.

DeMaria, M., 2009: A simplified dynamical system for tropical cyclone intensity prediction. *Mon. Wea. Rev.*, **137**, 68–82.

DeMaria, M. and J. Kaplan, 1994a: Sea surface temperature and the maximum intensity of Atlantic tropical cyclones. *J. Climate*, **7**, 1324–1334.

DeMaria, M. and J. Kaplan, 1994b: A statistical hurricane intensity prediction scheme (SHIPS) for the Atlantic basin. *Wea. Forecasting*, **9**, 209–220.

DeMaria, M. and J. Kaplan, 1999: An updated Statistical Hurricane Intensity Prediction Scheme (SHIPS) for the Atlantic and eastern North Pacific basins. *Wea. Forecasting*, **14**, 326–337.

DeMaria, M., J. Knaff, and B. Connell, 2001: A tropical cyclone genesis parameter for the tropical Atlantic. *Wea. Forecasting*, **16**, 219–233.

DeMaria, M., M. Mainelli, L. Shay, J. Knaff, and J. Kaplan, 2005: Further improvements to the Statistical Hurricane Intensity Prediction Scheme (SHIPS). *Wea. Forecasting*, **20**, 531–543.

Dunion, J. and C. Velden, 2004: The impact of the Saharan air layer on Atlantic tropical cyclone activity. *Bull. Amer. Meteor. Soc.*, **85**, 353–365.

Dunkerton, T., M. Montgomery, and Z. Wang, 2009: Tropical cyclogenesis in a tropical wave critical layer: easterly waves. *Atmos. Chem. Phys.*, **9**, 5587–5646.

Durran, D., 1999: *Numerical methods for wave equations in geophysical fluid dynamics*. Springer, New York, 465 pp.

Edson, J., et al., 2007: The Coupled Boundary Layers and Air-Sea Transfer experiment in low winds. *Bull. Amer. Meteor. Soc.*, **88**, 341–356.

Elsberry, R. and R. Jeffries, 1996: Vertical wind shear influences on tropical cyclone formation and intensification during TCM-92 and TCM-93. *Mon. Wea. Rev.*, **124**, 1374–1387.

Emanuel, K., 1986: An air-sea interaction theory for tropical cyclones. Part I: Steady-state maintenance. *J. Atmos. Sci.*, **43**, 585–604.

Emanuel, K., 1989: The finite-amplitude nature of tropical cyclogenesis. *J. Atmos. Sci*, **46**, 3431–3456.

Emanuel, K., 1991: The theory of hurricanes. *Ann. Rev. Fluid Mech.*, **23**, 179–196.

Emanuel, K., 1994: *Atmospheric convection*. Oxford University Press, New York, 580 pp.

Emanuel, K., 1995: Sensitivity of tropical cyclones to surface exchange coefficients and a revised steady-state model incorporating eye dynamics. *J. Atmos. Sci.*, **52**, 3969–3976.

Emanuel, K., 1997: Some aspects of hurricane inner-core dynamics and energetics. *J. Atmos. Sci.*, **54**, 1014–1026.

Emanuel, K., 2000: A statistical analysis of tropical cyclone intensity. *Mon. Wea. Rev.*, **128**, 1139–1152.

Emanuel, K., 2003: Tropical cyclones. *Annu. Rev. Earth Planetary Sci.*, **31**, 75–104.

Emanuel, K., 2004: Tropical cyclone energetics and structure. *Atmospheric Turbulence and Mesoscale Meteorology*, E. Federovich, R. Rotunno, and B. Stevens, Eds., Cambridge University Press, 165–192.

Emanuel, K., 2007: Environmental factors affecting tropical cyclone power dissipation. *J. Clim.*, **20**, 5497–5509.

Emanuel, K., 2010: Tropical cyclone activity downscaled from NOAA-CIRES reanalysis, 1908-1958. *J. Adv. Model. Earth Syst.*, **2**, 12 pp.

Emanuel, K., C. DesAutels, C. Holloway, and R. Korty, 2004: Environmental control of tropical cyclone intensity. *J. Atmos. Sci.*, **61**, 843–858.

Emanuel, K. and D. Nolan, 2004: Tropical cyclone activity and the global climate system. *26th Conf. on Hurricanes and Tropical Meteorology*, Amer. Meteor. Soc., Miami, FL, 240–241.

Emanuel, K., S. Ravela, E. Vivant, and C. Risi, 2006: A statistical deterministic approach to hurricane risk assessment. *Bull. Amer. Meteor. Soc.*, **87**, 299–314.

Emanuel, K., R. Sundararajan, and J. Williams, 2008: Hurricanes and global warming - results from downscaling IPCC AR4 simulations. *Bull. Amer. Meteor. Soc.*, **89**, 347–367.

Fedorov, A., C. Brierley, and K. Emanuel, 2010: Tropical cyclones and permanent El Nino in the early Pliocene epoch. *Nature*, **463**, 1066–1070.

Frank, W. and E. Ritchie, 1999: Effects of environmental flow upon tropical cyclone structure. *Mon. Wea. Rev.*, **127**, 2044–2061.

Frank, W. and E. Ritchie, 2001: Effects of vertical wind shear on the intensity and structure of numerically simulated hurricanes. *Mon. Wea. Rev.*, **129**, 2249–2269.

Franklin, J., 2010: National Hurricane Center forecast verification. [http://www.nhc.noaa.gov/verification/].

Gallina, G. and C. Velden, 2002: Environmental vertical wind shear and tropical cyclone intensity change utilizing enhanced satellite derived wind information. *25th Conf. on Hurricanes and Tropical Meteorology*, Amer. Meteor. Soc., San Diego, CA, 172–173.

Garner, S., I. Held, T. Knutson, and J. Sirutis, 2009: The roles of wind shear and thermal stratification in past and projected changes of Atlantic tropical cyclone activity. *J. Clim.*, **22**, 4723–4734.

Goldenberg, S., C. Landsea, A. Mestas-Nunez, and W. Gray, 2001: The recent increase in Atlantic hurricane activity: Causes and implications. *Science*, **293**, 474–479.

Goody, R., 2003: On the mechanical efficiency of deep, tropical convection. *J. Atmos. Sci.*, **60**, 2827–2832.

Gray, W., 1968: Global view of the origin of tropical disturbances and storms. *Mon. Wea. Rev.*, **96**, 669–700.

Gray, W., 1979: Hurricanes: Their formation, structure and likely role in the tropical circulation. *Meteorology over the Tropical Oceans*, D. B. Shaw, Ed., Royal Meteorological Society, 155–218.

Gunn, R. and G. Kinzer, 1949: The terminal velocity of fall for water droplets in stagnant air. *J. Meteor.*, **6**, 243–248.

Hanley, D., J. Molinari, and D. Keyser, 2001: A composite study of the interactions between tropical cyclones and upper-tropospheric troughs. *Mon. Wea. Rev.*, **129**, 2570–2584.

Hartmann, D., J. Holton, and Q. Fu, 2001: The heat balance of the tropical tropopause, cirrus, and stratospheric dehydration. *Geophys. Res. Lett.*, **28**, 1969–1972.

Hendricks, E. and W. Schubert, 2009: Transport and mixing in idealized barotropic hurricane-like vortices. *Quart. J. Roy. Meteor. Soc.*, **135**, 1456–1470.

Heymsfield, G., J. Halverson, E. Ritchie, J. Simpson, J. Molinari, and L. Tian, 2006: Structure of highly sheared Tropical Storm Chantal during CAMEX-4. *J. Atmos. Sci.*, **63**, 268–287.

Holland, G., 1997: The maximum potential intensity of tropical cyclones. *J. Atmos. Sci.*, **54**, 2519–2541.

Holloway, C. and J. Neelin, 2007: The convective cold top and quasi equilibrium. *J. Atmos. Sci.*, **64**, 1467–1487.

Jin, Y., W. Thompson, S. Wang, and C. Liou, 2007: A numerical study of the effect of dissipative heating on tropical cyclone intensity. *Wea. Forecasting.*, **22**, 950–966.

Jones, S., 1995: The evolution of vortices in vertical shear. I: Initially barotropic vortices. *Quart. J. Roy. Meteor. Soc.*, **121**, 821–851.

Jones, S., 2000a: The evolution of vortices in vertical shear. II: Large-scale asymmetries. *Quart. J. Roy. Meteor. Soc.*, **126**, 3137–3159.

Jones, S., 2000b: The evolution of vortices in vertical shear. III: Baroclinic vortices. *Quart. J. Roy. Meteor. Soc.*, **126**, 3161–3185.

Jones, S., 2004: On the ability of dry tropical-cyclone-like vortices to withstand vertical shear. *J. Atmos. Sci.*, **61**, 114–119.

Jordan, C., 1958: Mean soundings for the West Indies area. *J. Meteor.*, **15**, 91–97.

Kalnay, E., et al., 1996: The NCEP/NCAR 40-year reanalysis project. *Bull. Amer. Meteor. Soc.*, **77**, 437–471.

Kinzer, G. and R. Gunn, 1951: The evaporation, temperature and relaxation-time of freely falling waterdrops. *J. Meteor.*, **8**, 71–83.

Klemp, J., J. Dudhia, and A. Hassiotis, 2008: An upper gravity-wave absorbing layer for NWP applications. *Mon. Wea. Rev.*, **136**, 3987–4004.

Klemp, J., W. Skamarock, and J. Dudhia, 2007: Conservative split-explicit time integration methods for the compressible nonhydrostatic equations. *Mon. Wea. Rev.*, **135**, 2897–2913.

Klemp, J. and R. Wilhelmson, 1978: The simulation of three-dimensional convective storm dynamics. *J. Atmos. Sci.*, **35**, 1070–1096.

Knaff, J., S. Seseske, M. DeMaria, and J. Demuth, 2004: On the influences of vertical wind shear on symmetric tropical cyclone structure derived from AMSU. *Mon. Wea. Rev.*, **132**, 2503–2510.

Knutson, T., J. Sirutis, S. Garner, G. Vecchi, and I. Held, 2008: Simulated reduction in Atlantic hurricane frequency under twenty-first-century warming conditions. *Nature Geosci.*, **1**, 359–364.

Knutson, T. and R. Tuleya, 2004: Impact of CO2-induced warming on simulated hurricane intensity and precipitation: Sensitivity to the choice of climate model and convective parameterization. *J. Clim.*, **17**, 3477–3495.

Knutson, T., et al., 2010: Tropical cyclones and climate change. *Nature Geosci.*, **3**, 157–163.

Kurihara, Y., M. Bender, and R. Ross, 1993: An initialization scheme of hurricane models by vortex specification. *Mon. Wea. Rev.*, **121**, 2030–2045.

Kwon, Y. and W. Frank, 2005: Dynamic instabilities of simulated hurricane-like vortices and their impacts on the core structure of hurricanes. Part I: Dry experiments. *J. Atmos. Sci.*, **62**, 3955–3973.

Kwon, Y. and W. Frank, 2008: Dynamic instabilities of simulated hurricane-like vortices and their impacts on the core structure of hurricanes. Part II: Moist experiments. *J. Atmos. Sci.*, **65**, 106–122.

Lackmann, G. and R. Yablonsky, 2004: The importance of the precipitation mass sink in tropical cyclones and other heavily precipitating systems. *J. Atmos. Sci.*, **61**, 1674–1692.

LeVeque, R., 2002: *Finite-volume methods for hyperbolic problems.* Cambridge University Press, Cambridge, 558 pp.

Lilly, D., 1962: On the numerical simulation of buoyant convection. *Tellus*, **14**, 148–172.

Lipps, F. and R. Hemler, 1980: Another look at the thermodynamic equation for deep convection. *Mon. Wea. Rev.*, **108**, 78–84.

Malkus, J. and H. Riehl, 1960: On the dynamics and energy transformations in steady-state hurricanes. *Tellus*, **12**, 1–20.

Marin, J., D. Raymond, and G. Raga, 2009: Intensification of tropical cyclones in the GFS model. *Atmos. Chem. Phys.*, **9**, 1407–1417.

Mason, P. and R. Sykes, 1982: A two-dimensional numerical study of horizontal roll vortices in an inversion capped planetary boundary-layer. *Quart. J. Roy. Meteor. Soc.*, **108**, 801–823.

McBride, J. and R. Zehr, 1981: Observational analysis of tropical cyclone formation. Part II: Comparison of non-developing versus developing systems. *J. Atmos. Sci.*, **38**, 1132–1151.

McDonald, R., D. Bleaken, D. Cresswell, V. Pope, and C. Senior, 2005: Tropical storms: representation and diagnosis in climate models and the impacts of climate change. *Clim. Dyn.*, **25**, 19–36.

McWilliams, J., L. Graves, and M. Montgomery, 2003: A formal theory for vortex Rossby waves and vortex evolution. *Geophys. Astrophys. Fluid Dynamics*, **97**, 275–309.

Mesinger, F., 1977: Forward-backward scheme, and its use in a limited area model. *Contrib. Atmos. Phys.*, **50**, 200–210.

Molinari, J., P. Dodge, D. Vollaro, K. Corbosiero, and F. Marks, 2006: Mesoscale aspects of the downshear reformation of a tropical cyclone. *J. Atmos. Sci.*, **63**, 341–354.

Molinari, J., D. Vollaro, and K. Corbosiero, 2004: Tropical cyclone formation in a sheared environment: A case study. *J. Atmos. Sci.*, **61**, 2493–2509.

Moller, J. and M. Montgomery, 1999: Vortex Rossby waves and hurricane intensification in a barotropic model. *J. Atmos. Sci.*, **56**, 1674–1687.

Moller, J. and M. Montgomery, 2000: Tropical cyclone evolution via potential vorticity anomalies in a three-dimensional balance model. *J. Atmos. Sci.*, **57**, 3366–3387.

Montgomery, M. and R. Kallenbach, 1997: A theory for vortex Rossby-waves and its application to spiral bands and intensity changes in hurricanes. *Quart. J. Roy. Meteor. Soc.*, **123**, 435–465.

Montgomery, M., R. Smith, and S. Nguyen, 2010: Sensitivity of tropical cyclone models to the surface exchange coefficients. *Quart. J. Roy. Meteor. Soc.*, in press.

Moskaitis, J., 2009: Toward improved tropical cyclone intensity forecasts : probabilistic prediction, predictability, and the role of verification. Ph.D. thesis, Massachusetts Institute of Technology.

Musgrave, K., C. Davis, and M. Montgomery, 2008: Numerical simulations of the formation of Hurricane Gabrielle (2001). *Mon. Wea. Rev.*, **136**, 3151–3167.

Nolan, D. and M. Montgomery, 2002: Nonhydrostatic, three-dimensional perturbations to balanced, hurricane-like vortices. Part I: Linearized formulation, stability, and evolution. *J. Atmos. Sci.*, **59**, 2989–3020.

Nolan, D. and E. Rappin, 2008: Increased sensitivity of tropical cyclogenesis to wind shear in higher SST environments. *Geophys. Res. Lett.*, **35**, L14 805.

Oouchi, K., J. Yoshimura, H. Yoshimura, R. Mizuta, S. Kusunoki, and A. Noda, 2006: Tropical cyclone climatology in a global-warming climate as simulated in a 20 km-mesh global atmospheric model: Frequency and wind intensity analyses. *J. Meteor. Soc. Japan*, **84**, 259–276.

Ooyama, K., 1990: A thermodynamic foundation for modeling the moist atmosphere. *J. Atmos. Sci.*, **47**, 2580–2593.

Ooyama, K., 2001: A dynamic and thermodynamic foundation for modeling the moist atmosphere with parameterized microphysics. *J. Atmos. Sci.*, **58**, 2073–2102.

Pauluis, O., 2007: Sources and sinks of available potential energy in a moist atmosphere. *J. Atmos. Sci.*, **64**, 2627–2641.

Pauluis, O. and I. Held, 2002: Entropy budget of an atmosphere in radiative-convective equilibrium. Part I: Maximum work and frictional dissipation. *J. Atmos. Sci.*, **59**, 125–139.

Peng, M., B. Jeng, and R. Williams, 1999: A numerical study on tropical cyclone intensification. Part I: Beta effect and mean flow effect. *J. Atmos. Sci.*, **56**, 1404–1423.

Persing, J. and M. Montgomery, 2003: Hurricane superintensity. *J. Atmos. Sci.*, **60**, 2349–2371.

Pielke Jr., R., J. Gratz, C. Landsea, D. Collins, M. Saunders, and R. Musulin, 2008: Normalized hurricane damages in the United States: 1900-2005. *Natural Hazards Rev.*, **9**, 29–42.

Powell, M., 1990: Boundary layer structure and dynamics in outer hurricane rainbands. Part II: Downdraft modification and mixed layer recovery. *Mon. Wea. Rev.*, **118**, 918–938.

Powell, M., P. Vickery, and T. Reinhold, 2003: Reduced drag coefficient for high wind speeds in tropical cyclones. *Nature*, **422**, 279–283.

Qiu, C., J. Bao, and Q. Xu, 1993: Is the mass sink due to precipitation negligible. *Mon. Wea. Rev.*, **121**, 853–857.

Raymond, D., 1995: Regulation of moist convection over the west Pacific warm pool. *J. Atmos. Sci.*, **52**, 3945–3959.

Raymond, D., S. Sessions, and Z. Fuchs, 2007: A theory for the spinup of tropical depressions. *Quart. J. Roy. Meteor. Soc.*, **133**, 1743–1754.

Raymond, D., S. Sessions, A. Sobel, and Z. Fuchs, 2009: The mechanics of gross moist stability. *J. Adv. Model. Earth Syst.*, **1**, 20 pp.

Reasor, P. and M. Montgomery, 2001: Three-dimensional alignment and corotation of weak, TC-like vortices via linear vortex Rossby waves. *J. Atmos. Sci.*, **58**, 2306–2330.

Reasor, P., M. Montgomery, and L. Grasso, 2004: A new look at the problem of tropical cyclones in vertical shear flow: Vortex resiliency. *J. Atmos. Sci.*, **61**, 3–22.

Reasor, P., M. Montgomery, F. Marks, and J. Gamache, 2000: Low-wavenumber structure and evolution of the hurricane inner core observed by airborne dual-Doppler radar. *Mon. Wea. Rev.*, **128**, 1653–1680.

Riemer, M., M. Montgomery, and M. Nicholls, 2010: A new paradigm for intensity modification of tropical cyclones: Thermodynamic impact of vertical wind shear on the inflow layer. *Atmos. Chem. Phys.*, **10**, 3163–3188.

Robe, F. and K. Emanuel, 2001: The effect of vertical wind shear on radiative-convective equilibrium states. *J. Atmos. Sci.*, **58**, 1427–1445.

Rogers, R., S. Chen, J. Tenerelli, and H. Willoughby, 2003: A numerical study of the impact of vertical shear on the distribution of rainfall in Hurricane Bonnie (1998). *Mon. Wea. Rev.*, **131**, 1577–1599.

Rotunno, R., Y. Chen, W. Wang, C. Davis, J. Dudhia, and G. Holland, 2009: Large-eddy simulation of an idealized tropical cyclone. *Bull. Amer. Meteor. Soc.*, **90**, 1783–1788.

Rotunno, R. and K. Emanuel, 1987: An air-sea interaction theory for tropical cyclones. Part II: Evolutionary study using a nonhydrostatic axisymmetric numerical model. *J. Atmos. Sci.*, **44**, 542–561.

Schecter, D., M. Montgomery, and P. Reasor, 2002: A theory for the vertical alignment of a quasigeostrophic vortex. *J. Atmos. Sci.*, **59**, 150–168.

Schubert, W., M. Montgomery, R. Taft, T. Guinn, S. Fulton, J. Kossin, and J. Edwards, 1999: Polygonal eyewalls, asymmetric eye contraction, and potential vorticity mixing in hurricanes. *J. Atmos. Sci.*, **56**, 1197–1223.

Shelton, K. and J. Molinari, 2009: Life of a six-hour hurricane. *Mon. Wea. Rev.*, **137**, 51–67.

Simpson, R. and R. Riehl, 1958: Mid-tropospheric ventilation as a constraint on hurricane development and maintenance. *Tech. Conf. on Hurricanes*, Amer. Meteor. Soc., Miami Beach, FL, D4–1–D4–10.

Skamarock, W. and J. Klemp, 1992: The stability of time-split numerical methods for the hydrostatic and the nonhydrostatic elastic equations. *Mon. Wea. Rev.*, **120**, 2109–2127.

Smith, R., 2006: Accurate determination of a balanced axisymmetric vortex in a compressible atmosphere. *Tellus*, **58A**, 98–103.

Smith, R., M. Montgomery, and H. Zhu, 2005: Buoyancy in tropical cyclones and other rapidly rotating atmospheric vortices. *Dyn. Atmos. Oceans*, **40**, 189–208.

Smith, R., W. Ulrich, and G. Sneddon, 2000: On the dynamics of hurricane-like vortices in vertical-shear flows. *Quart. J. Roy. Meteor. Soc.*, **126**, 2653–2670.

Soden, B. and I. Held, 2006: An assessment of climate feedbacks in coupled ocean-atmosphere models. *J. Clim.*, **19**, 3354–3360.

Srivastava, R., 1987: A model of intense downdrafts driven by the melting and evaporation of precipitation. *J. Atmos. Sci.*, **44**, 1752–1773.

Tripoli, G. and W. Cotton, 1981: The use of lce-liquid water potential temperature as a thermodynamic variable in deep atmospheric models. *Mon. Wea. Rev.*, **109**, 1094–1102.

Uppala, S., et al., 2005: The ERA-40 re-analysis. *Quart. J. Roy. Meteor. Soc.*, **131**, 2961–3012.

Van Sang, N., R. Smith, and M. Montgomery, 2008: Tropical cyclone intensification and predictability in three dimensions. *Quart. J. Roy. Meteor. Soc.*, **134**, 563–582.

Vecchi, G. and B. Soden, 2007a: Global warming and the weakening of the tropical circulation. *J. Clim.*, **20**, 4316–4340.

Vecchi, G. and B. Soden, 2007b: Increased tropical Atlantic wind shear in model projections of global warming. *Geophys. Res. Lett.*, **34**, L08 702.

Wang, Y., 2002a: Vortex Rossby waves in a numerically simulated tropical cyclone. Part I: Overall structure, potential vorticity, and kinetic energy budgets. *J. Atmos. Sci.*, **59**, 1213–1238.

Wang, Y., 2002b: Vortex Rossby waves in a numerically simulated tropical cyclone. Part II: The role in tropical cyclone structure and intensity changes. *J. Atmos. Sci.*, **59**, 1239–1262.

Wicker, L. and W. Skamarock, 2002: Time-splitting methods for elastic models using forward time schemes. *Mon. Wea. Rev.*, **130**, 2088–2097.

Willoughby, H., J. Clos, and M. Shoreibah, 1982: Concentric eye walls, secondary wind maxima, and the evolution of the hurricane vortex. *J. Atmos. Sci.*, **39**, 395–411.

Wong, M. and J. Chan, 2004: Tropical cyclone intensity in vertical wind shear. *J. Atmos. Sci.*, **61**, 1859–1876.

Wu, C. and K. Emanuel, 1995: Potential vorticity diagnostics of hurricane movement. Part 1: A case study of Hurricane Bob (1991). *Mon. Wea. Rev.*, **123**, 69–92.

Wu, L. and S. Braun, 2004: Effects of environmentally induced asymmetries on hurricane intensity: A numerical study. *J. Atmos. Sci.*, **61**, 3065–3081.

Yang, B., Y. Wang, and B. Wang, 2007: The effect of internally generated inner-core asymmetries on tropical cyclone potential intensity. *J. Atmos. Sci.*, **64**, 1165–1188.

Yoshimura, J., M. Sugi, and A. Noda, 2006: Influence of greenhouse warming on tropical cyclone frequency. *J. Meteor. Soc. Japan*, **84**, 405–428.

Yu, J., Y. Wang, and K. Hamilton, 2010: Response of tropical cyclone potential intensity to a global warming scenario in the IPCC AR4 CGCMs. *J. Clim.*, **23**, 1354–1373.

Zehr, R., 1992: Tropical cyclogenesis in the western north Pacific. Tech. rep., U.S. Department of Commerce, NOAA/NESDIS, 5200 Auth Rd., Washington, DC 20233.

Zeng, X., W. Tao, and J. Simpson, 2005: An equation for moist entropy in a precipitating and icy atmosphere. *J. Atmos. Sci.*, **62**, 4293–4309.

Zeng, Z., L. Chen, and Y. Wang, 2008: An observational study of environmental dynamical control of tropical cyclone intensity in the Atlantic. *Mon. Wea. Rev.*, **136**, 3307–3322.

Zeng, Z., Y. Wang, and C. Wu, 2007: Environmental dynamical control of tropical cyclone intensity - an observational study. *Mon. Wea. Rev.*, **135**, 38–59.

Zhao, M., I. Held, S. Lin, and G. Vecchi, 2009: Simulations of global hurricane climatology, interannual variability, and response to global warming using a 50-km resolution GCM. *J. Clim.*, **22**, 6653–6678.